

UNIVERSIDAD CARLOS III DE MADRID

ESCUELA POLITÉCNICA SUPERIOR



BACHELOR THESIS

IMPLEMENTATION OF A COMPLETE SCHEME OF BEAM HARDENING CORRECTION IN A SMALL ANIMAL CT SCANNER

Cristina Viña Berlanga

JUNE 2015

Implementation of a Complete Scheme of Beam Hardening Correction in a Small Animal CT Scanner

AUTHOR: Cristina Viña Berlanga
DIRECTOR: Mónica Abella García
CO-DIRECTOR: Claudia de Molina Gómez

Laboratorio de Imagen Médica (LIM)
Unidad de Medicina y Cirugía Experimental (UMCE)
Hospital General Universitario Gregorio Marañón

Departamento de Bioingeniería e Ingeniería Aeroespacial
Universidad Carlos III de Madrid

Título: Implementation of a Complete Scheme of Beam Hardening Correction in a Small Animal CT Scanner

Autor: Cristina Viña Berlanga

Director: Mónica Abella García

Co-director: Claudia de Molina Gómez

EL TRIBUNAL

Presidente: Manuel Urueña Pascual

Vocal: Gerson Rodríguez de los Santos López

Secretario: Alejandro García Lampérez

Realizado el acto de defensa y lectura del Trabajo Fin de Grado el día 13 de julio de 2015, en la Escuela Politécnica Superior de la Universidad Carlos III de Madrid, acuerda otorgarle la CALIFICACIÓN de:

VOCAL

SECRETARIO

PRESIDENTE

Abstract

In recent years, advances in the biomedical sciences have been accelerated by the uprising number of discoveries in genomics and molecular and cell biology which have led to the development of animal models of human diseases. The last improvements in instrumentation for medical imaging have enabled non-invasive investigations of biological processes in vivo, allowing longitudinal studies. Imaging systems are especially aimed to obtain high quality images of live animals. Small animal imaging techniques are essential to translational research in order to help in the early detection, diagnosis and treatment of diseases or pathological disorders.

X-ray computed tomography (CT) images suffer from several artifacts that impair the qualitative and quantitative analysis of the images. This project is focus in one of the most common artifacts encountered in micro-CT which is produced by the physical phenomenon of beam hardening. This effect causes cupping in homogeneous objects, and dark streaks between denser parts within heterogeneous volumes.

This project is part of a research line followed by the Biomedical Imaging and Instrumentation Group of the University Carlos III of Madrid and which takes place at the Instituto de Investigación Sanitaria Gregorio Marañón. The work is devoted to research into medical imaging techniques for applications in preclinical research, and to design, develop and evaluate new acquisition systems, as well as to carry out different processing and reconstruction methodologies for multimodal images. The result of this project will be incorporated into a high-resolution, small animal X-ray tomograph (micro-CT) which was developed by the group and it is currently being both manufactured and commercialized worldwide by the Spanish company SEDECAL S.A.

The general objective of this bachelor thesis is to incorporate and evaluate a complete scheme of beam hardening correction into the preclinical micro-CT scan developed by the laboratory research group. With the aim of fulfilling this objective, the beam hardening calibration method, as well as the linearization and post-processing

correction methods are implemented into the multimodality workstation (MMWKS) console by using the programming language IDL. Afterwards, a beam hardening calibration phantom and a test phantom are designed. The stability of the BH calibration parameters is studied and the parameters for the second order are optimized. Finally, the evaluation of the system in real studies takes place.

Keywords

X-rays, small animal, micro-CT, beam hardening correction

Agradecimientos

En primer lugar me gustaría que estas líneas sirvieran para expresar mi más profundo y sincero agradecimiento a todas aquellas personas que con su ayuda han colaborado en la consecución del presente proyecto.

Especial mención a Mónica, mi directora de proyecto, ya que sin ella esto no podría haberse llevado a cabo. Muchas gracias por confiar en mí desde el primer día y ofrecerme la posibilidad de realizar este proyecto. Gracias también a Claudia, co-directora y actual doctoranda. Ambas me habéis transmitido día a día vuestra pasión e interés por la imagen médica. Gracias de corazón por contagiarme la ilusión por la investigación y hacer que cada mañana me despertase de buen humor para ir al hospital. Agradecer también a todos los compañeros del Laboratorio de Imagen Médica del Hospital General Universitario Gregorio Marañón por acogerme entre vosotros como una más.

Por último me gustaría dedicar este proyecto con gran cariño a mi familia y amigos. Muchas gracias por la comprensión, paciencia y el ánimo recibidos en estos últimos años de carrera, en especial a mis padres. Gracias por darme alas para volar y brindarme la oportunidad de viajar a otros mundos.

A todos vosotros, muchas gracias.

Content Index

ABSTRACT	I
AGRADECIMIENTOS	III
CONTENT INDEX	IV
FIGURE INDEX	VI
TABLE INDEX	IX
1 INTRODUCTION	2
1.1 X-RAYS TISSUE DENSITIES	4
1.2 INTRODUCTION TO THE ELECTROMAGNETIC SPECTRUM: X-RAYS	4
1.2.1 <i>X-rays production</i>	5
1.2.2 <i>X-ray interaction with matter</i>	7
1.2.3 <i>X-rays detection</i>	8
1.3 EVOLUTION OF CT SYSTEMS	9
1.4 PROJECTION	12
1.5 IMAGE RECONSTRUCTION	13
1.5.1 <i>Analytical reconstruction methods</i>	13
1.5.2 <i>Iterative reconstruction methods</i>	17
1.6 BEAM HARDENING ARTIFACTS	19
1.6.1 <i>Beam hardening characterization</i>	20
2 MOTIVATION AND OBJECTIVES	24
2.1 MOTIVATION	24
2.2 OBJECTIVES	27
2.3 THESIS STRUCTURE	28
3 SYSTEM UNDER STUDY	31
3.1 GENERATION OF THE X-RAY IMAGE AT THE DETECTOR	32
3.2 IMAGE RECONSTRUCTION AND VISUALIZATION	34
4 FIRST ORDER METHOD	37
4.1 THEORETICAL EXPLANATION	37
4.2 CALIBRATION	39
4.2.1 <i>Design of the calibration phantom</i>	39
4.2.2 <i>Software development of the calibration procedure</i>	41
4.2.3 <i>Integration of the developed calibration software into the system</i>	47
4.2.4 <i>Definition of a calibration protocol</i>	49
4.3 CORRECTION	53
4.3.1 <i>Software development and integration of the first order correction procedure</i>	53
4.4 EVALUATION	54
4.4.1 <i>Evaluation of the stability of the BH calibration parameters</i>	57
5 SECOND ORDER METHOD	62
5.1 THEORETICAL EXPLANATION	62
5.2 CALIBRATION	65

5.2.1	<i>Design of the calibration phantom</i>	<i>68</i>
5.3	CORRECTION	69
5.3.1	<i>Software development and integration of the second order correction procedure</i>	<i>69</i>
5.4	EVALUATION	73
6	CONCLUSIONS AND FUTURE WORK.....	77
6.1	CONCLUSIONS	77
6.2	FUTURE WORK.....	79
	APPENDIX A: BIBLIOGRAPHIC REVIEW OF THE BEAM HARDENING CORRECTION METHODS.....	80
	APPENDIX B: ‘.ACT’ HEADER EXAMPLE.....	83
	APPENDIX C: ‘.HDR’ HEADER EXAMPLE	86
	BIBLIOGRAPHICAL REFERENCES	89
	GLOSSARY OF TERMS.....	92
	PROJECT MANAGEMENT.....	93
I.	GANTT CHART.....	93
II.	FINANCIAL PLAN.....	94

Figure Index

FIGURE 1-1: HUMAN RADIOLOGICAL STUDIES: (LEFT) THORAX, AND (RIGHT) CRANIAL.....	3
FIGURE 1-2: REPRESENTATION OF THE THREE PLANES FORMED BY TOMOGRAPHIC SLICES, AND (RIGHT) CORONAL, AXIAL AND SAGITTAL SLICES FROM A MAXILLOFACIAL CT	3
FIGURE 1-3: ELECTROMAGNETIC SPECTRUM.....	5
FIGURE 1-4: SCHEMATIC SKETCH OF AN X-RAY TUBE.....	5
FIGURE 1-5: GENERATION OF BRAKING RADIATION.	6
FIGURE 1-6: GENERATION OF CHARACTERISTIC RADIATION.	6
FIGURE 1-7: CHARACTERISTIC X-RAY EMISSION SPECTRUM DUE TO THE TYPICAL PHENOMENA PRODUCED INSIDE THE X-RAY TUNGSTEN TUBE.	7
FIGURE 1-8: MASS ATTENUATION COEFFICIENTS FOR SOFT TISSUE.	7
FIGURE 1-9: SCHEME OF A DIGITAL RADIOLOGY DETECTION SYSTEM (FLAT PANEL) WITH INDIRECT CONVERSION (KÖRNER ET AL 2007).	8
FIGURE 1-10: CT HOUNSFIELD SCALE ACCORDING TO THE BODY OR SOFT TISSUE WINDOW, WHICH IS CENTRED ON THE TISSUES OF INTEREST (AIR-BONE), WITH BLACK AND WHITE AT THE EXTREME ENDS OF THE SPECTRUM.	9
FIGURE 1-11: (LEFT) FIRST CLINICAL CT SCANNER (OCT 1971), AND (RIGHT) ITS FIRST IMAGE OBTAINED.	9
FIGURE 1-12: SCHEME OF THE WORKING MECHANISM OF THE DIFFERENT GENERATIONS OF CT SYSTEMS.	11
FIGURE 1-13: SCHEME OF THE WORKING MECHANISM OF HELICAL SCANNERS.....	11
FIGURE 1-14: SIMPLE EXAMPLE OF THE PROJECTION CONCEPT.	12
FIGURE 1-15: SCHEME OF THE PROJECTION FORMAL DEFINITION WITH PARALLEL X-RAY BEAM.	13
FIGURE 1-16: FOURIER SLICE THEOREM (ABELLA 2010).....	14
FIGURE 1-17: DIRECT FOURIER RECONSTRUCTION (ABELLA 2010).	14
FIGURE 1-18: (LEFT) SINGLE BACKPROJECTION, AND (RIGHT) FILTERED BACKPROJECTION.....	15
FIGURE 1-19: EXAMPLE SHOWING THE FILTERING EFFECT OVER A BACKPROJECTED IMAGE.	16
FIGURE 1-20: SCHEMATIC DIAGRAMS WITH DIFFERENT ACQUISITION MODES: (LEFT) FAN BEAM, AND (RIGHT) CONE BEAM. THE FAN BEAM CORRESPONDS ONLY TO THE CENTRAL PLANE OF THE CONE BEAM.	17
FIGURE 1-21: SCHEME OF THE WORKING MECHANISM OF ITERATIVE RECONSTRUCTION METHODS.....	18
FIGURE 1-22: (LEFT) AXIAL SLICE OF A CT IMAGE OF A HOMOGENEOUS CYLINDER WITH CUPPING (THE INNER AREA IS CLEARLY DARKER THAN THE OUTER PART), AND (RIGHT) BASE OF A SKULL WITH DARK STREAKS (BONES HAVE A HIGHER ATOMIC NUMBER THAN WATER).	19
FIGURE 1-23: FI, TOTAL ATTENUATION OF WATER WHEN THE X-RAY SOURCE IS MONOENERGETIC AT A VOLTAGE OF 45KeV.	20
FIGURE 1-24: FBH, TOTAL ATTENUATION OF WATER AT 45KeV WHEN THE X-RAY SOURCE IS POLYENERGETIC.	21
FIGURE 1-25: ENERGY DEPENDENCE OF ATTENUATION COEFFICIENTS OF TISSUES M(E).	22
FIGURE 1-26: ENERGY SPECTRUM OF THE PHOTON NUMBER EMITTED BY THE SOURCE $N_{IN}(E)$ (BLACK LINE), AND THE SAME SPECTRUM AFTER TRAVERSING 4CM OF WATER (BLUE LINE).....	22
FIGURE 2-1: PET IMAGING OF RAT BRAIN.	24
FIGURE 2-2: CT IMAGING OF RAT BRAIN.	25
FIGURE 2-3: PET/CT IMAGING OF RAT BRAIN	25
FIGURE 2-4: (LEFT) PMMA PHANTOM SUFFERING FROM CUPPING (DARKER AREA IN THE CENTRE), AND (RIGHT) HEAD SCAN OF A RAT WHICH SHOWS DARK STREAKS BETWEEN ITS BONES (RED LINES POINTING).....	26
FIGURE 3-1: MULTIMODAL ARGUS PET/CT BY SEDECAL.....	31
FIGURE 3-2: SCHEMA OF THE GEOMETRY OF THE MICRO-CT SYSTEM.	32

FIGURE 3-3: (A) <i>Nout</i> : RAW DATA OBTAINED AT THE DETECTOR, (B) <i>Nfill</i> : FLOOD IMAGE (WITHOUT THE OBJECT), (C) <i>Idark</i> : DARK CURRENT IMAGE (X-RAY SOURCE OFF), (D) <i>MXDX</i> :: RAW DATA OBTAINED AT THE DETECTOR AFTER CORRECTION (3.3), (E) ATTENUATION IMAGE AFTER APPLYING THE LOGARITHM TO (D).	33
FIGURE 3-4: VISUALIZATION OF THE SAGITTAL, CORONAL AND AXIAL SLICES FROM A SMALL ANIMAL CT STUDY WITH THE MMWKS CONSOLE.	34
FIGURE 3-5: SCHEMATIC OF THE COMMUNICATION BETWEEN THE USER PC AND THE CONTROL PC (PLACED INSIDE THE SCANNER).	35
FIGURE 4-1: REPRESENTATION OF THE BEAM HARDENING FUNCTION <i>FBH_T</i> AND ITS CORRESPONDING IDEAL FUNCTION <i>FI_T</i>	38
FIGURE 4-2: LINEARIZATION FUNCTION.	38
FIGURE 4-3: (A) SIMULATION OF A TRIANGULAR PHANTOM, (B) RECONSTRUCTED IMAGE OF (A) SHOWING ARTIFACTS DUE TO THE ANGULAR SHAPE OF THE PHANTOM.	40
FIGURE 4-4: (LEFT) SKETCH OF THE CALIBRATION PHANTOM DONE IN MATLAB AND SENT TO THE MANUFACTURERS, AND (RIGHT) BRAND-NEW CYLINDRICAL PPMA CALIBRATION PHANTOM.	41
FIGURE 4-5: BLOCK DIAGRAM OF THE CALIBRATION PROCESS.	42
FIGURE 4-6: EMPIRICAL BH FUNCTION <i>FBH_T</i> OBTAINED AT DIFFERENT VOLTAGES.	44
FIGURE 4-7: FIT BH FUNCTION <i>FBH_{fit}(T)</i> COMPUTED FOR DIFFERENT VOLTAGES.	45
FIGURE 4-8: IDEAL BH FUNCTION <i>FI(T)</i> COMPUTED FOR DIFFERENT VOLTAGES.	45
FIGURE 4-9: TRANSFORMED BH FUNCTION <i>T(x)</i> COMPUTED FOR DIFFERENT VOLTAGES.	46
FIGURE 4-10: TEXT FILE CONTAINING THE CALIBRATION DATA AND INFORMATION FROM AN ACQUISITION MADE ON THE 17 TH OF MARCH 2015 AT A VOLTAGE OF 35 kVp.	47
FIGURE 4-11: FIRST ORDER CALIBRATION FLOW CHART.	48
FIGURE 4-12: PPMA SEMI-CYLINDRICAL BH CALIBRATION PHANTOM WITH A RADIUS OF 3 cm.	49
FIGURE 4-13: (LEFT) BH CALIBRATION PHANTOM LYING IN THE ARGUS PET/CT BED WHILE THE RED ARROW POINTS TO ITS END, AND (RIGHT) GUIDING BED ELEVATION AT 3 cm.	50
FIGURE 4-14: (LEFT) MAIN MENU OF THE MMWKS CONSOLE, AND (RIGHT) DIFFERENT ACQUISITION OPTIONS INCLUDING THE NEW BH CALIBRATION BUTTON.	50
FIGURE 4-15: SEQUENTIAL PROCESS FOR OBTAINING THE SCANOGRAM: ACQUISITIONS AT 0=0° AND 0=90°.	51
FIGURE 4-16: (LEFT) FIRST ORDER SEGMENTATION INTERFACE SHOWING THE CENTRAL SLICE OF THE RECONSTRUCTED VOLUME, AND (RIGHT) MASK RESULTING FROM THE SEGMENTATION OF THE SAME SLICE.	52
FIGURE 4-17: POP-UP WINDOW INFORMING THE USER ABOUT THE SUCCESSFUL COMPLETION OF THE BH CALIBRATION.	52
FIGURE 4-18: RECONSTRUCTION INTERFACE SHOWING THE NEW INTEGRATED BH CORRECTION OPTIONS.	53
FIGURE 4-19: CYLINDRICAL, HOMOGENEOUS PMMA TEST PHANTOM FOR THE BH FIRST ORDER CORRECTION.	54
FIGURE 4-20: (LEFT) RECONSTRUCTED PROJECTIONS WITHOUT CORRECTION, AND (RIGHT) SAME PROJECTIONS WITH FIRST ORDER CORRECTION.	55
FIGURE 4-21: PROFILE REPRESENTATION OF THE CUPPING ARTIFACT AND ITS CORRECTION.	55
FIGURE 4-22: SKETCH OF CUPPING PROFILES.	56
FIGURE 4-23: SKETCH OF CUPPING PROFILES WITH POINTS FOR THE ANALYTICAL COMPUTATION OF THE CUPPING EFFECT.	56
FIGURE 4-24: PROFILES OF THE RECONSTRUCTION OF A HOMOGENEOUS CYLINDRICAL PHANTOM BEFORE AND AFTER THE FIRST ORDER CORRECTION, AS WELL AS THE IDEAL CORRECTION PROFILE. THE ACQUISITION PARAMETERS WERE 35 kVp, 240 μA, 360 PROJECTIONS, BINNING 4, AND 8 SHOTS.	57
FIGURE 4-25: LINEARIZATION FUNCTIONS AT A VOLTAGE OF 35, 40, 45, AND 50 kVp TAKEN IN DIFFERENT DAYS.	60
FIGURE 5-1: MASS ATTENUATION COEFFICIENTS FOR HUMAN TISSUES NORMALIZED AT A VOLTAGE OF 40 KEV (ELBAKRI <i>ET AL</i> 2002).	62

FIGURE 5-2: RESPRESENTATION OF $\lambda(\epsilon)$ EXPRESSING THE DEPENDENCY BETWEEN THE MASS ATTENUATION OF THE BONE AND THE SOFT TISSUE WITHIN THE SAME ENERGY RANGE	63
FIGURE 5-3: DIAGRAM SHOWING THE SECOND ORDER CORRECTION PROCEDURE.	65
FIGURE 5-4: SECOND ORDER CALIBRATION PHANTOM SIMULATED IN MATLAB.	66
FIGURE 5-5: MATLAB SIMULATION FOR OBTAINING THE MSE OF THE SECOND ORDER CALIBRATION PARAMETERS.	66
FIGURE 5-6: DIFFERENT RECONSTRUCTION PROFILES FROM A SIMULATION (WITH AND WITHOUT CORRECTION).	67
FIGURE 5-7: AXIAL SLICE OF FOUR EPPENDORF FILLED WITH DIFFERENT CONCENTRATIONS OF A MIXED IODINE AND SALINE SOLUTION.	68
FIGURE 5-8: MATERIALS USED FOR THE FABRICATION OF THE BH SECOND ORDER CALIBRATION/TEST PHANTOM.	69
FIGURE 5-9: BH CORRECTION FLOW CHART.	70
FIGURE 5-10: SEQUENCE DIAGRAM OF THE SECOND ORDER BH CORRECTION.	72
FIGURE 5-11: SECOND ORDER SEGMENTATION INTERFACE, (LEFT) WITHOUT MASK, AND (RIGHT) WITH IT.	73
FIGURE 5-12: (LEFT) RECONSTRUCTED PROJECTIONS WITHOUT CORRECTION, AND (RIGHT) SAME PROJECTIONS WITH SECOND ORDER CORRECTION.	74
FIGURE 5-13: PROFILE REPRESENTATION OF THE DARK STREAKS EFFECT AND ITS CORRECTION.	74
FIGURE 5-14: RECONSTRUCTED IMAGE FROM THE SECOND ORDER PHANTOM AND THE DATA OBTAINED TO WHEN ANALYSING DIFFERENT REGIONS TO CALCULATE ITS ANR.	75
FIGURE 5-15: PROFILE REPRESENTATION OF THE DARK STREAKS EFFECT AND ITS CORRECTION.	75

Table Index

TABLE 3-1: POSSIBLE CONFIGURATIONS OF THE PROJECTION DATA FILES WITH EXTENSION ‘.CTF’	34
TABLE 4-1: ACQUISITION PARAMETERS OF THE CALIBRATION PHANTOM WHERE THE NUMBER OF <i>SHOTS</i> CORRESPONDS TO THE NUMBER OF SHOTS FROM THE SOURCE IN EACH ANGULAR POSITION WHICH WILL BE AVERAGED OUT IN ORDER TO REDUCE NOISE, AND <i>BINNING</i> CORRESPONDS TO THE RESOLUTION.	51
TABLE 4-2: 17TH MARCH 2015: BH CALIBRATION PARAMETERS.....	58
TABLE 4-3: 31ST MARCH 2015: BH CALIBRATION PARAMETERS.	58
TABLE 4-4: 14TH APRIL 2015: BH CALIBRATION PARAMETERS.	58
TABLE 4-5: BEHAVIOUR OF THE FIRST ORDER CALIBRATION PARAMETERS AS THE VOLTAGES INCREASES.	59
TABLE 4-6: MEAN (μ) AND STANDARD DEVIATION (σ) OF THE FIRST ORDER CALIBRATION PARAMETERS.	60
TABLE 5-1: RESULTING VALUES OF THE SECOND ORDER CORRECTION PARAMETERS AFTER COMPUTING THE MSE ITERATIVELY IN A MATLAB SIMULATION.....	67

INTRODUCTION

1 Introduction

Diagnostic imaging is a widely spread discipline in the medical world. It represents the spatial distribution of one or more physical or chemical properties inside the human body, which facilitates the detection of any anomalies in the clinical picture of a patient.

Techniques used in diagnostic imaging, also known as image modalities, are characterized by radiating the patient with some kind of energy. Depending on the symptoms presented, as well as the body part to be treated, doctors may apply one modality or another. Among them stand out the radiology (*X-rays*), nuclear medicine (*γ -rays*), magnetic resonance imaging (*radio waves*), echography (*ultrasound*) and endoscopy (*light*).

Radiology is the most used medical imaging modality worldwide. It has numerous advantages such as low cost and speed. This modality employs X-ray energy, which was discovered in 1895 by the German physician Wilhelm Conrad Röntgen who would receive the Physics Nobel Prize a few years after.

The main imaging techniques which apply to this modality are the *conventional radiology*, the *digital radiology*, and the *computerized tomography (CT)*. All these techniques are ionizing as they use X-rays energy. The X-rays induce chemical reactions over the patient due to the high energy that is being irradiated and which leads to the ionization of diverse molecules. Likewise, spatial high-resolution images are obtained, and detailed information about the anatomy of the subject is extracted according to the density of the tissue traversed by the rays.

Conventional radiology is the technique by which a projective image is obtained when exposing a photographic film to radiation with high energy levels. The film captures the photons radiated by the X-ray source which were neither absorbed nor scattered by the patient, who is placed between the source and the photographic film. These images are said to be projective as each pixel represents the integral of the physical properties of an object along a ray being projected onto a screen.

Digital radiology is very similar to the conventional one. Its working mechanism differs only in the utilization of a digital detector instead of the film screen, which it is more sensitive and allows the reduction of the ionizing radiation dose to the patient. On the other hand, and thanks to the image digitalization, it is possible to recover certain valid information by applying image processing even when the performing conditions of the scan were not the optimal ones. Scan repetitions may be avoided when applying this technique.

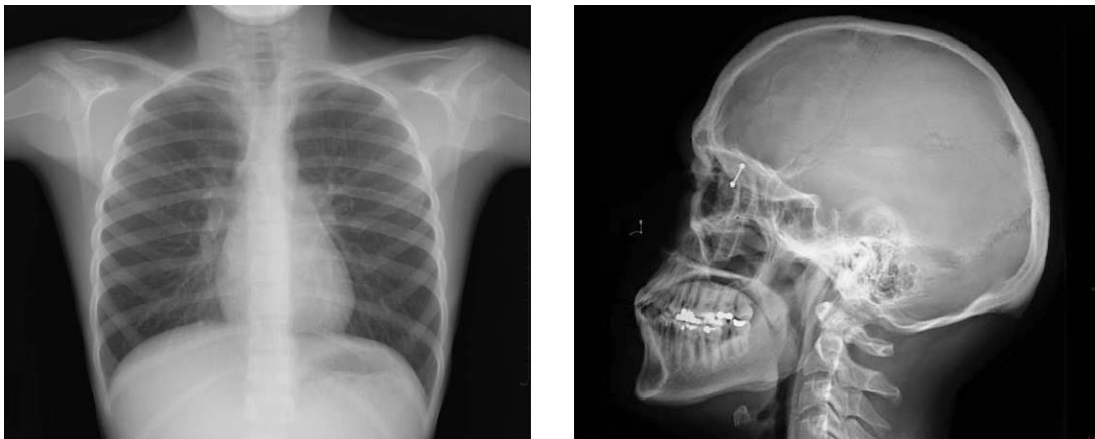


Figure 1-1: Human radiological studies: (left) thorax, and (right) cranial.

Computed tomography (CT), unlike its two predecessors, is able to separate each of the different planes of the sample (Figure 1-2), and to represent them into a two-dimensional image. Tomographic slices facilitate the visualization of a body section and its interpretation without interferences from other regions.

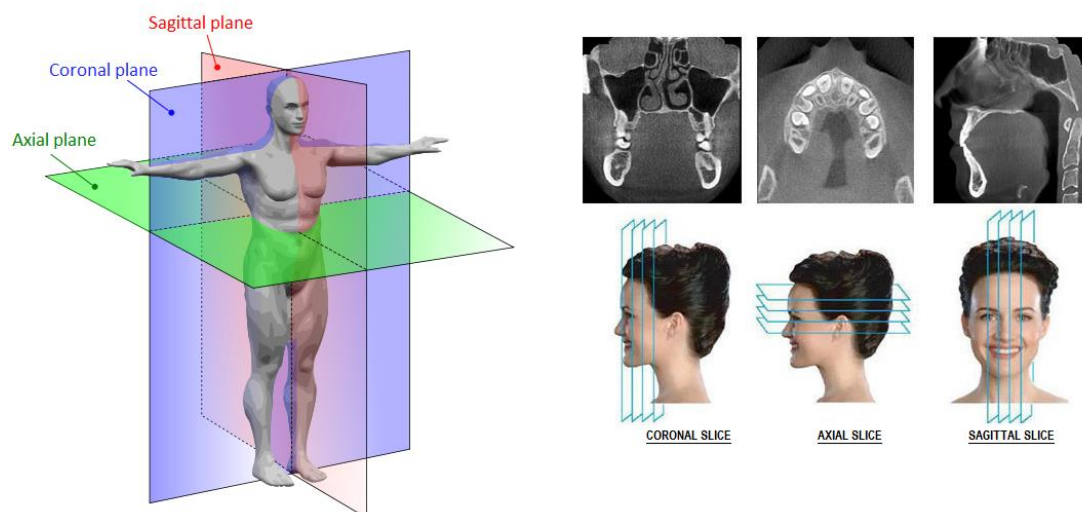


Figure 1-2: Representation of the three planes formed by tomographic slices, and (right) coronal, axial and sagittal slices from a maxillofacial CT

1.1 X-rays tissue densities

X-rays can pass through matter more or less easily depending on its density. The term density is closely related with how close the particles are held together. The denser the matter, the fewer photons arrive to the detector. Soft tissues and fluids scarcely attenuate the rays, while hard tissue such as bone is more likely to block them, mostly the softer ones.

Hard X-rays are X-rays with high frequencies and extremely penetrating into the matter. Soft X-rays are X-rays with lower frequencies and they are usually filtered in order to remove these non-image forming X-rays from the beam as well as scatter before it reaches the scanned object (Brooks et al 1976). This filter reduces the number of photons that reach the detector by absorbing the ones with a low energy and therefore, the Signal-to-Noise Ratio (SNR) is also reduced. By filtering these rays, the patient avoids receiving an unnecessary radiation dose and thus, the risk of radiation damage is reduced.

1.2 Introduction to the electromagnetic spectrum: X-rays

X-rays are a form of electromagnetic radiation with high frequency and short wavelength, i.e., they have an extremely high energy as shown in (1.1). In the electromagnetic spectrum (Figure 1-3), it can be observed that the X-ray energy ranges from about 5×10^4 to 10^6 eV, considerably higher than those of light, but less than the gamma (Γ -) rays which have a mean energy of 10^{10} eV. This large amount of energy allows the X-ray photons to interact and modify the molecular structure of the patient. Therefore, an overexposure to X-ray radiation could be considered dangerous and harmful as it can give rise to muscular problems.

X-rays are commonly produced by accelerating or decelerating charged particles. For simplicity, the energy of X-rays can be defined as the energy of a photon which follows:

$$E = \frac{h \cdot c}{\lambda} = h \cdot \nu \quad (1.1)$$

where $h = 4,135 \times 10^{-15}$ eV · s is the Planck's constant, $c = 2.997 \times 10^8$ m/s the speed of light, λ the wavelength, and ν the frequency.

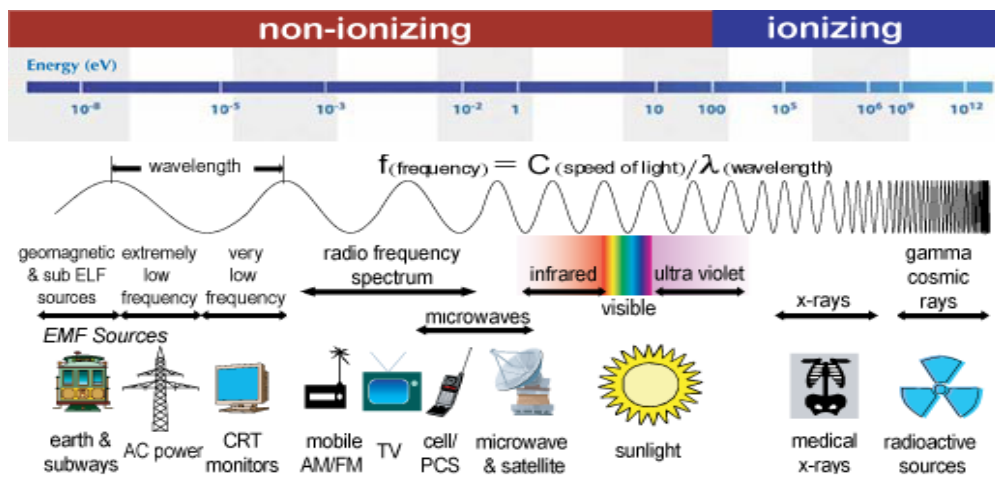


Figure 1-3: Electromagnetic spectrum.

1.2.1 X-rays production

X-rays are produced when electrons lose most or all of their kinetic energy by interacting with the atoms of a metal target. An X-ray tube contains a heated cathode filament through which the electrons are accelerated and emitted towards the matter of the anode (generally made of tungsten). After the electrons meet the target, about 98 % of their kinetic energy is given up in heat. The 2 % left is divided among the breaking radiation (commonly known as bremsstrahlung), and the characteristic radiation. The generation of X-rays by deceleration of electrons is thus very inefficient (Bissonnette 1991).

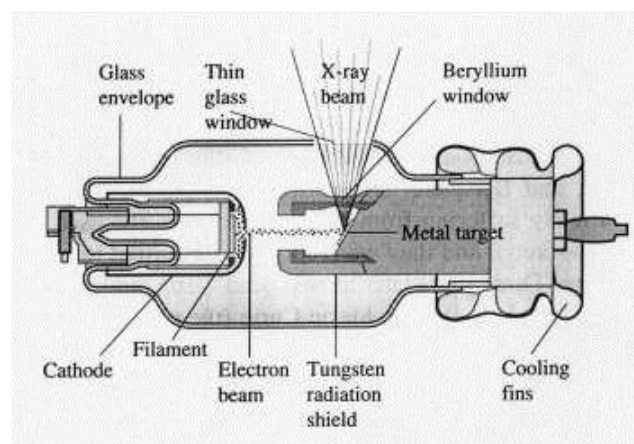


Figure 1-4: Schematic sketch of an X-ray tube.

- **Braking radiation (Bremsstrahlung)** is the process responsible for most of the X-rays produced inside an X-ray tube. An incident electron loses part of its kinetic energy when it collides with the nucleus of the target atom. The nuclear Coulomb field deflects the original course of the electron and makes it to release part of its energy as a photon.

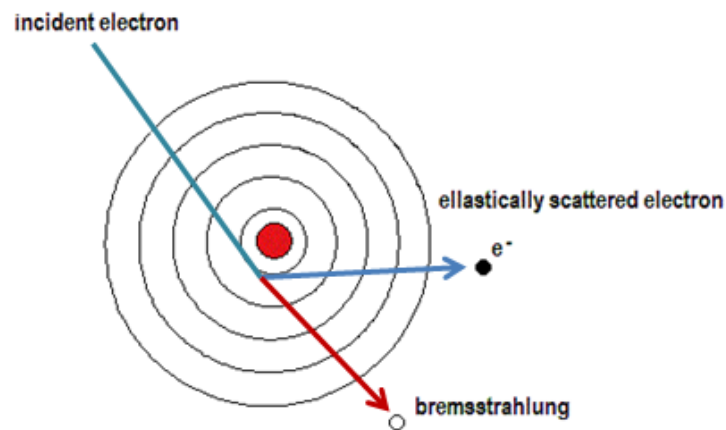


Figure 1-5: Generation of braking radiation.

- **Characteristic radiation** results from the collision of the incident electron with the target atom which triggers the ejection of an electron from its inner shells. The resulting ionized atom is in an excited state and electrons belonging to higher energy levels from outer shells cover successively the gap in order to come back to its ground state. These transitions produce X-ray photons.

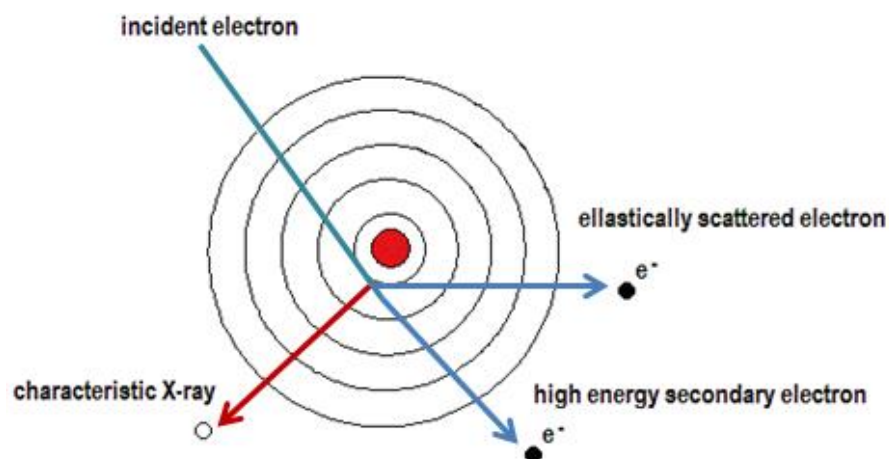


Figure 1-6: Generation of characteristic radiation.

Most of the low-energy photons are absorbed by the X-rays tube, which affects to the spatial distribution at low energies as shown in the following energy spectrum.

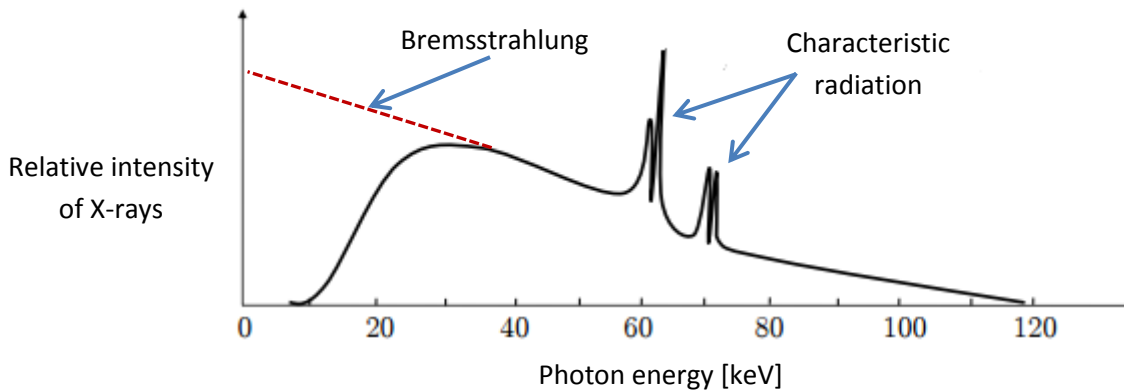


Figure 1-7: Characteristic X-ray emission spectrum due to the typical phenomena produced inside the X-ray tungsten tube.

1.2.2 X-ray interaction with matter

X-ray intensity decays when traversing matter. During the X-ray interaction within the range of energies commonly used in radiology (100 – 150 keV), other effects such as Rayleigh and the Compton scattering, and the photoelectric effect take place at the same time.

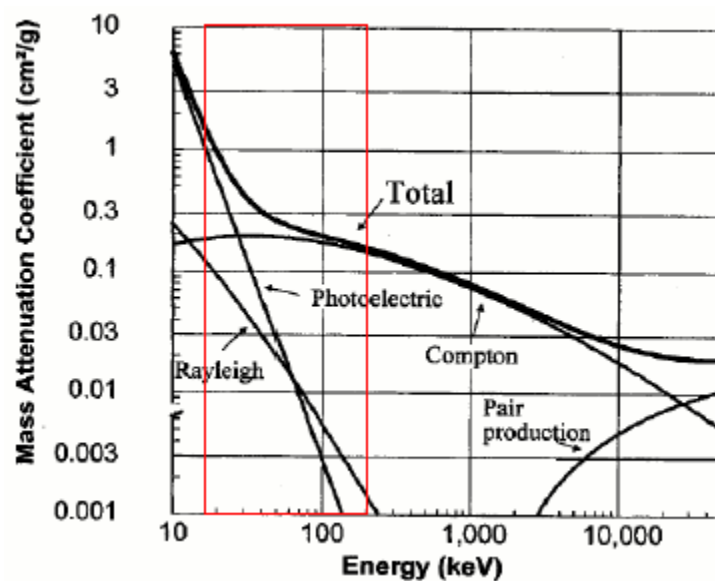


Figure 1-8: Mass attenuation coefficients for soft tissue.

1.2.3 X-rays detection

The first X-rays detectors used for obtaining medical images were compounded of a photographic film made out of a silver halide emulsion. This film is more sensitive to visible light rather than to X-rays, making necessary high X-rays doses to obtain images with a reasonable quality.

In the nineties, it appeared the direct radiography systems which convert X-rays into electric signals. These systems can be grouped into direct or indirect depending on the conversion type. Direct conversion systems convert the X-ray photons into electric signals in a single step by using a photoconductor material. Indirect conversion systems are considered as two step processes because they first convert X-rays into light, and then the light into photoelectrons. One of the most common digital radiology detection system with indirect conversion is called flat panel. Flat panel detectors present a small size, are lighter, and far more durable than other digital detectors. They have a good image quality with a low radiation dose, and are more sensitive and faster than film.

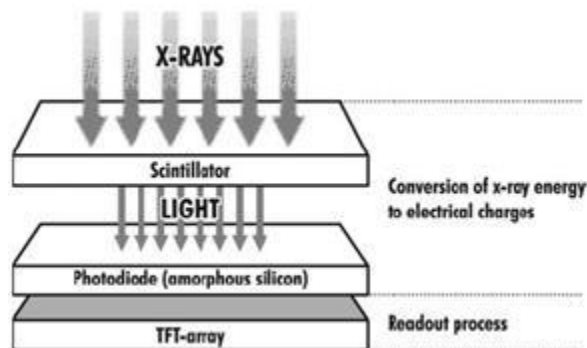


Figure 1-9: Scheme of a digital radiology detection system (flat panel) with indirect conversion (Körner et al 2007).

CT Hounsfield scale

The Hounsfield scale is the result of a quantitative transformation of the original linear attenuation coefficient μ of an object at a given energy. As shown in Figure 1-10, the CT Hounsfield scale displays radiodensity in a linear greyscale expressed in Hounsfield Units (HU), (Hounsfield, 1979). These units are computed by applying the formula stated in (1.2):

$$HU = 1000 \times \frac{\mu - \mu_{water}}{\mu_{water} - \mu_{air}} \quad (1.2)$$

where μ , μ_{water} and μ_{air} are the attenuation coefficients of the object under study, the water, and the air respectively.

The Hounsfield Units represent the relative density of each tissue element from a scanned object. Each pixel of a CT image acquires a value which oscillates between -1000 HU (black; low density) and +3000 HU (white, high density).

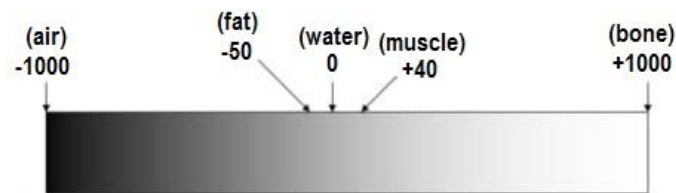


Figure 1-10: CT Hounsfield scale according to the body or soft tissue window, which is centred on the tissues of interest (air-bone), with black and white at the extreme ends of the spectrum.

1.3 Evolution of CT systems

Tomographic systems have undergone a major evolution since its inception and subsequent implementation in 1971. A brief description of the different generations of these systems is next.



Figure 1-11: (Left) first clinical CT scanner (Oct 1971), and (right) its first image obtained.

- First generation

First CT systems are based on the geometry of the parallel X-ray beam. A single source is responsible for the emission of a highly collimated narrow beam towards a single detector which performs translational and rotational movements. The X-ray source is translated across the patient in order to obtain a set of parallel

projection measurements at each angle. Then the source is rotated and the procedure is repeated up to 180°. This mechanism generates very high scanning times of 4-5 minutes per scan and therefore, this process results in a harmful emission of high X-ray doses to the patient.

- **Second generation**

Tomographic systems belonging to the second generation differ from their predecessor in the X-ray beam geometry. Multiple narrow beams are used in order to reduce the acquisition time. The trajectory described by the rays is called fan beam, i.e., the rays diverge from the same point in a fan shape. Furthermore, the number of detectors is significantly increased (between 5 and 30). Thus, the number of rotations is reduced from 180 to 6. As shown in the Figure 1-4, the X-ray tube generates multiple beams, each of which is incident on one single detector.

- **Third generation**

This generation of tomographic systems removes the translational movement characteristic of the previous generations by arranging the detectors (around 700 units) in an arc. The X-ray source fan beam is wider enough to cover the entire area to be scanned. Thus, only a synchronous rotation of both the source and the arc is needed. The scan time is considerably improved up to few seconds.

- **Fourth generation**

Tomographic systems belonging to the fourth generation are also rotational scanners in which the detector array is a stationary ring containing up to 4,800 fixed detectors. The X-ray tube rotates around that ring. This generation is more sensitive to scattered radiation and avoids the ring artifacts characteristic of previous generation scanners.

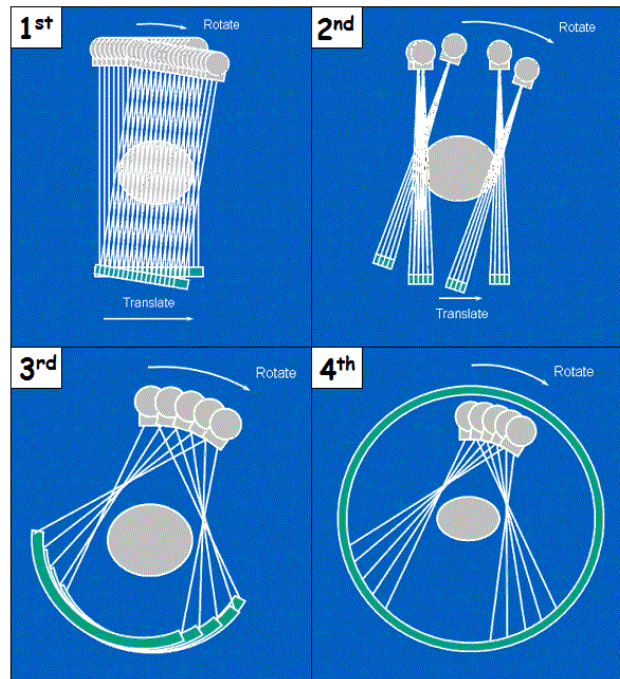


Figure 1-12: Scheme of the working mechanism of the different generations of CT systems.

- Spiral/helical scanners

These 3D scanners belong to the latest generation of CT. The X-ray source describes a helical trajectory around the patient, who lies in a motorized bed that moves axially at a uniform rate. Both the source and a two-dimensional array of detectors are placed on a rotating gantry. Although this method allows to take multiple slices at a time as well as to image more tissue volume in less time, the complexity of the reconstruction of the image is highly increased.

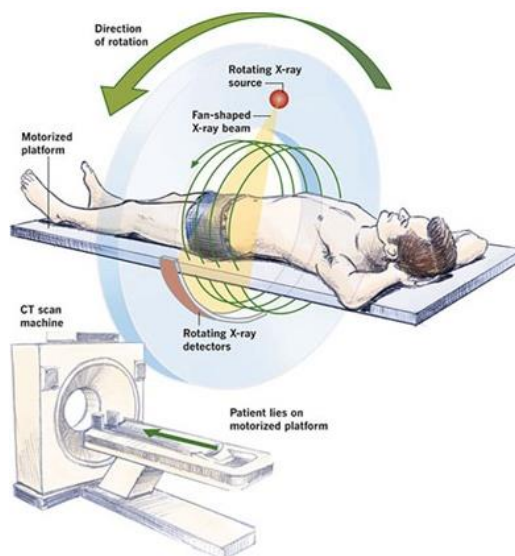


Figure 1-13: Scheme of the working mechanism of helical scanners.

1.4 Projection

Data gathered by the tomographic systems generate the so-called projections. In order to explain the concept in an intuitive and easy way, a 2D image with different attenuation coefficients (μ) and parallel beam geometry is used (Figure 1-14). The projection acquired at a scan angle of $\theta=0^\circ$ is the sum of the attenuation coefficients along the horizontal trajectories which follow the X-rays. At this point, the data is still insufficient to reconstruct the image. In order to know the disposition and the value of the four attenuation coefficients, it is necessary to scan one more time but at an angle of $\theta=90^\circ$, so that the total attenuation in the vertical axis is also obtained. These two projections are enough to find out the attenuation coefficients by solving the system with four unknowns and four linear equations. In a real system, the number of unknowns is greater, and consequently more projections are needed in order to reconstruct the scanned object. Note that the noise is not being taken into account in this example.

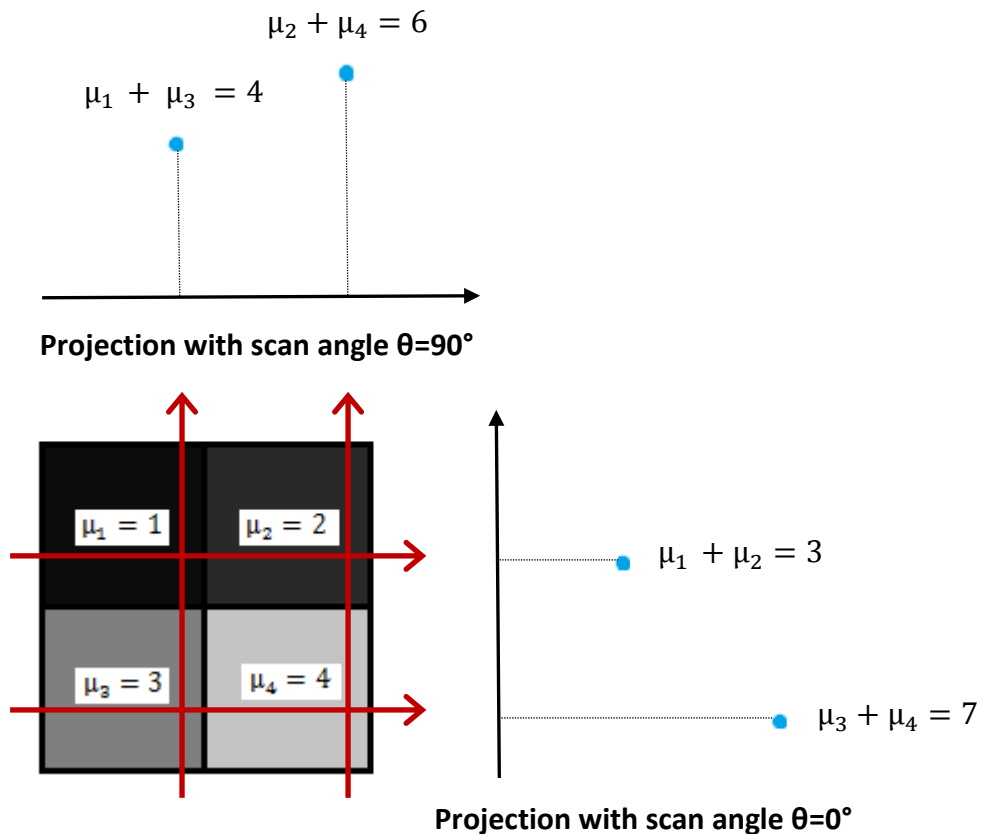


Figure 1-14: Simple example of the projection concept.

There is also a formal way to define a projection in the continuous domain as the set of line integrals across the object at a given angle (Figure 1-15).

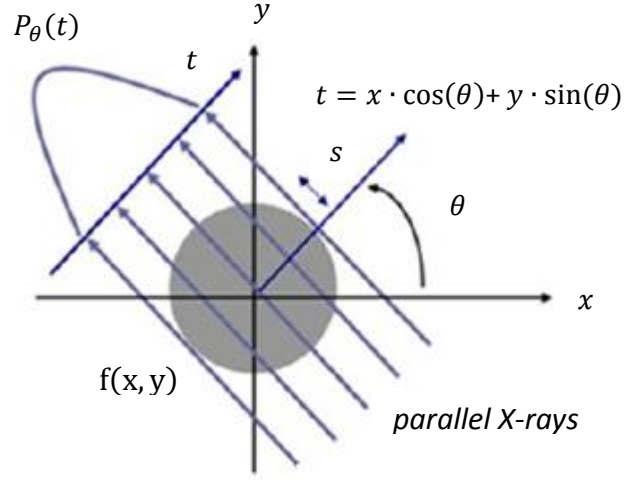


Figure 1-15: Scheme of the projection formal definition with parallel X-ray beam.

$$P_{\theta}(t) = \int_{(\theta,t)} f(x, y) \cdot ds = \int_{-\infty}^{+\infty} f(x, y) \cdot \delta(x \cdot \cos(\theta) + y \cdot \sin(\theta) - t) \cdot dx \cdot dy \quad (1.3)$$

$$t = x \cdot \cos(\theta) + y \cdot \sin(\theta) \quad (1.4)$$

1.5 Image reconstruction

The main objective of tomography is to achieve the reconstruction of an object by generating its volume from just a set of projections. Nowadays, there is a number of reconstruction methods which fall into two categories depending on the mathematical basis used when turning the angular projections into the original dataset. These reconstruction methods can be either analytical or iterative.

1.5.1 Analytical reconstruction methods

The analytical methods attempt to reconstruct the image by finding an analytical expression that allows obtaining the inverse of $P_{\theta}(t)$, commonly known as the Radon transform of $f(x, y)$.

These methods are based on the Fourier Slice Theorem which relates the Fourier transform of a projection to the 2D Fourier transform of the object along a radial line (Kak 1988).

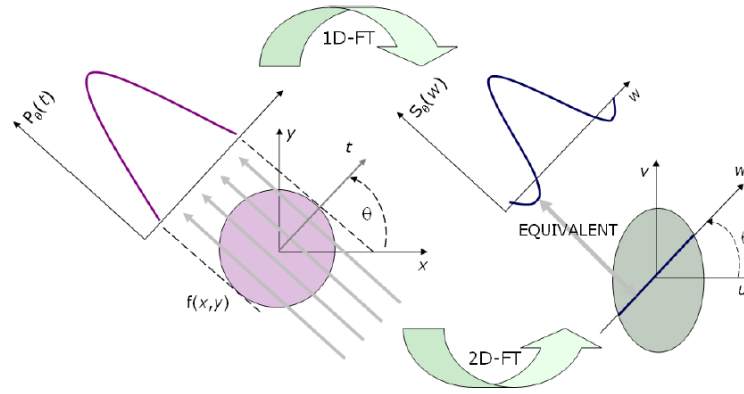


Figure 1-16: Fourier Slice Theorem (Abella 2010).

1.5.1.1 Direct Fourier reconstruction

The direct Fourier reconstruction method is directly based on the Fourier Slice Theorem (Figure 1-17). According to this theorem, once obtained the 1D-FT of the projections of an object $f(x,y)$ at different angles, it is possible to determine the values of the 2D-FT of the object, $F(u,v)$. If infinite projections were taken, all points of $F(u,v)$ would be known and thus, the object $f(x,y)$ could be recovered by applying the inverse Fourier transform.

In practice, only a finite number of projections is available from the measurements. Radon transform samples radially the frequency space of the 2D object. Afterwards, the data points are resampled to a rectangular grid by interpolation. This step can lead to the introduction of high-frequency artifacts. The interpolation turns out to be less accurate as it goes further from the coordinates centre due to a coarse sampling. Finally, a 2D inverse Fourier transform of $F(u,v)$ is performed to recover the object function $f(x,y)$.

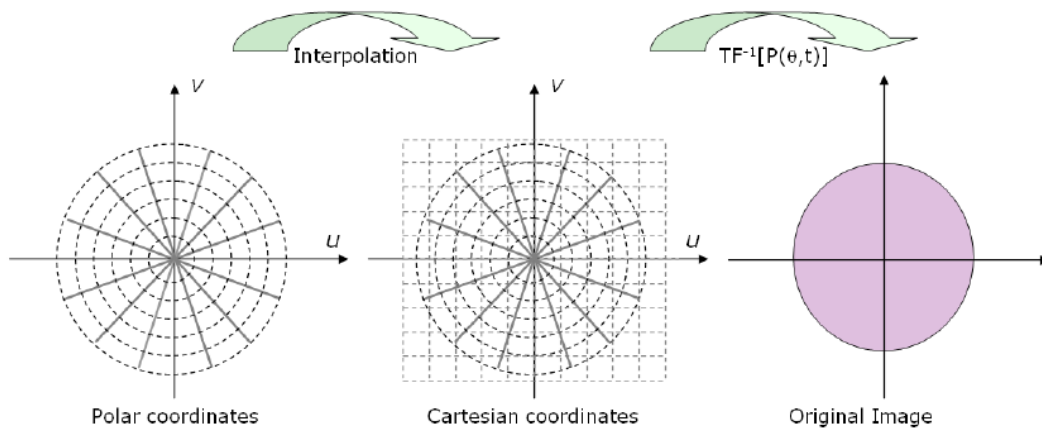


Figure 1-17: Direct Fourier reconstruction (Abella 2010).

1.5.1.2 Filtered Back Projection (FBP reconstruction)

FBP is a reconstruction algorithm based on the Central Slice Theorem. It has two parts: filtering and backprojection. The filtering part can be simply understood as a weighting of each of the acquired projections in the frequency domain. The second part is in charge of setting all the image pixels along the ray pointing to the sample to the same value. This algorithm was developed for correcting the blurriness of the images reconstructed by simple backprojection (Figure 1-18).

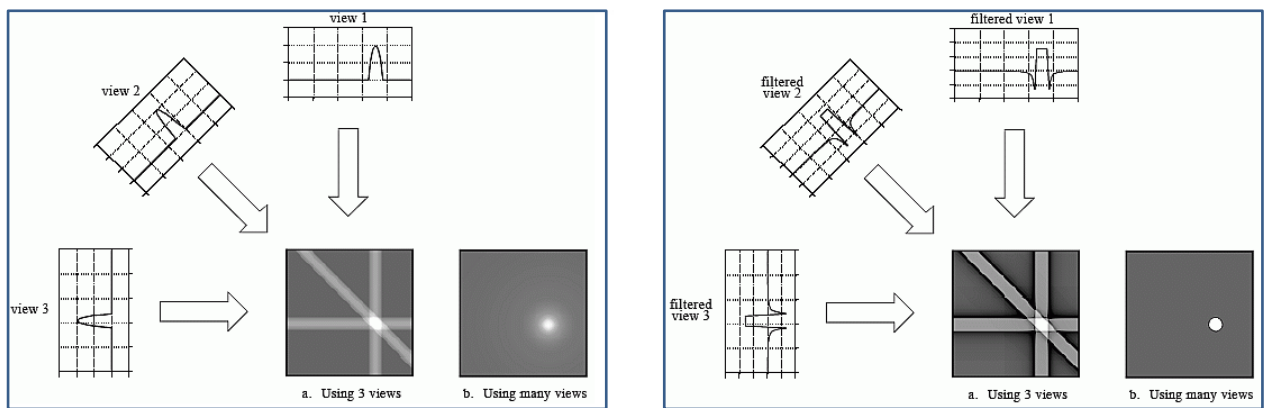


Figure 1-18: (Left) Single backprojection, and (right) filtered backprojection.

The resulting backprojected image represents a blurred version of the original one as it has large low-frequency components. In order to recover the original image the filtering part is needed. The various frequency components of the image are multiplied by a filter function in the frequency domain.

To give a more intuitive insight, an example is shown in Figure 1-19. The image (a) was obtained after backprojection. Figure 1-19 a' corresponds to its 2D Fourier transform which explains the blurriness of the backprojected image as its greater values correspond to low frequencies. With the purpose of improving that image and enhancing its edges, a 2D ramp filter with cone shape is used. This filter has the effect of reducing the image low-frequency components and increasing the weight of the high ones. The filter (Figure 1-19 b) is applied in the frequency space. Figure 1-19 b' shows an intensification of the high-frequency components which lead to a more defined image (c) when applying the inverse Fourier transform.

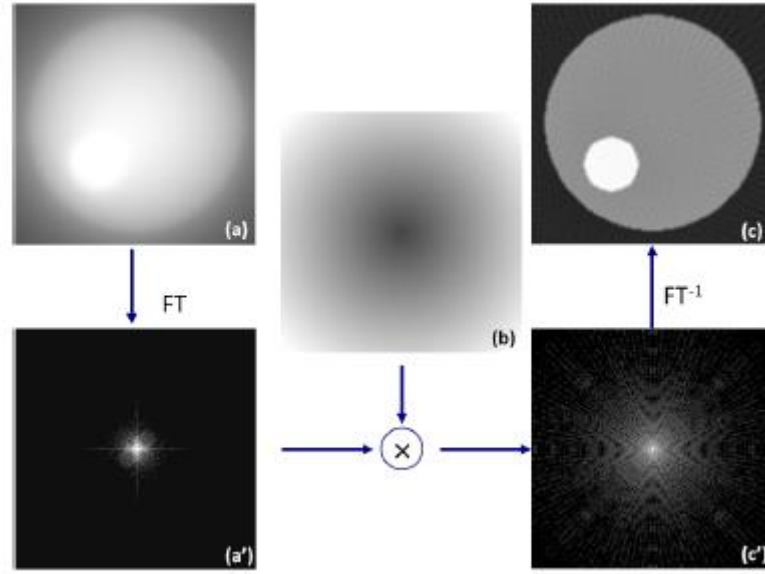


Figure 1-19: Example showing the filtering effect over a backprojected image.

This method can be easily extended to different 2D X-rays geometries like fan beam as well as to 3D reconstructions following a cone beam geometry.

1.5.1.3 Feldkamp-Davis-Kress (FDK reconstruction)

FDK is a reconstruction algorithm designed for cone beam projections which have been acquired from a circular source trajectory (Feldkamp *et al* 1984).

This method deals with three-dimensional image reconstruction by proposing an approximation of the FBP to a 3D model. Therefore, it is also based on the Fourier Slice Theorem. A third axial coordinate is introduced, so that all rays obtained from transformations of the coordinate system can be taken into account.

The mathematical concept is explained in depth in (Kak 1988), and it is based on the following formula:

$$f(u, v, z) = \frac{1}{2} \int_0^{2\pi} \frac{D_{SO}^2}{(D_{SO}-v)^z} \int_{-\infty}^{\infty} R_{\beta}(p, z) h\left(\frac{D_{SO}u}{D_{SO}-v} - p\right) \frac{D_{SO}}{\sqrt{D_{SO}^2 + u^2 + z^2}} dp d\beta \quad (1.5)$$

where D_{SO} indicates the distance between the source and the object, R_{β} is the projection data, and h represents the 3D version of the ramp filter.

The quality of the FDK reconstruction varies with the elevation of the plane. For example, if taking the central slice of the object with rotation plane $z=0$, the cone

beam algorithm would be identical to an equispacial fan beam algorithm (Figure 1-20), yielding to a good reconstruction. However, in the case of any other slice, each point of the object was irradiated from all directions at an oblique angle. This fact causes cone beam artifacts in the reconstruction, which leads to a noticeable degradation in the image. Indeed, just the central slice has the correct data in order to apply FBP accurately. Hence, the central slice is the only one that can be reconstructed without errors. These errors keep increasing as we get further from the central plane.

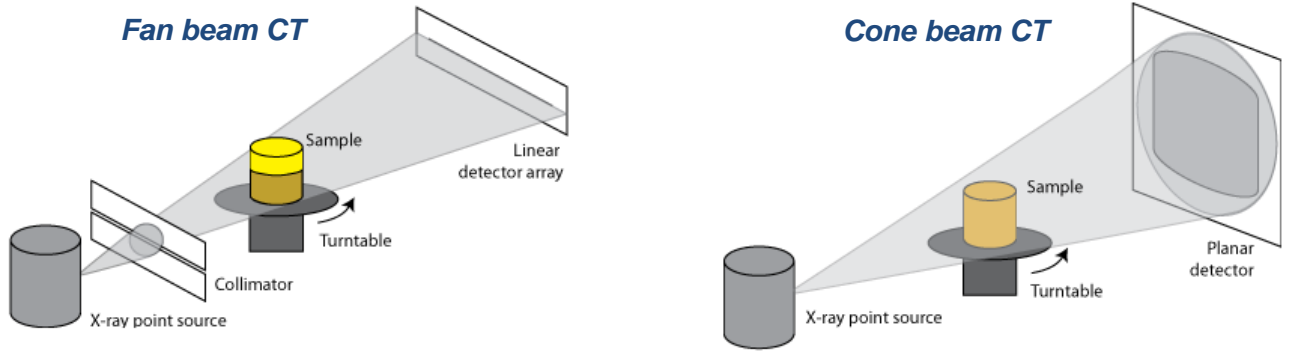


Figure 1-20: Schematic diagrams with different acquisition modes: (left) fan beam, and (right) cone beam. The fan beam corresponds only to the central plane of the cone beam.

Analytical reconstruction methods are computationally efficient and therefore, they are widely used on clinical CT scanners. However, they are not able of handling some complex factors such as scatter.

1.5.2 Iterative reconstruction methods

The iterative methods attempt to reconstruct the image by generating a system of equations in which its unknowns are substituted by the projection data (1.6).

$$\begin{aligned}
 w_{11}f_1 + w_{12}f_2 + w_{13}f_3 + \cdots + w_{1n}f_n &= p_1 \\
 w_{21}f_1 + w_{22}f_2 + w_{23}f_3 + \cdots + w_{2n}f_n &= p_2 \\
 &\dots \\
 w_{m1}f_1 + w_{m2}f_2 + w_{m3}f_3 + \cdots + w_{mn}f_n &= p_m
 \end{aligned}
 \tag{1.6}$$

where f_j is the grey value of the voxel j of the volume that is being reconstructed, p_i is

the value measured at the detector for the ray i , and w_{ij} are the weights that defined the influence of the voxel j over the ray i . Expressing it as a matrix:

$$W \cdot f = P \quad (1.7)$$

Matrix W has a really high value about 100000 TB, so the computation of its inverse can be almost immediately discarded. Iterative methods use instead successive approximations until reaching to a reasonable estimation of the distribution, which originally generated the data acquired. This idea is graphically shown in Figure 1-21.

The method starts with a simplified estimation of the image, i.e., a mask in which the object values turn into ones and the rest is set to zero. The simulated projections are compared with the real image projections each iteration. The error obtained is subtracted in order to correct the estimated projection. The procedure is repeated once and another until obtaining the most similar image to the original one.

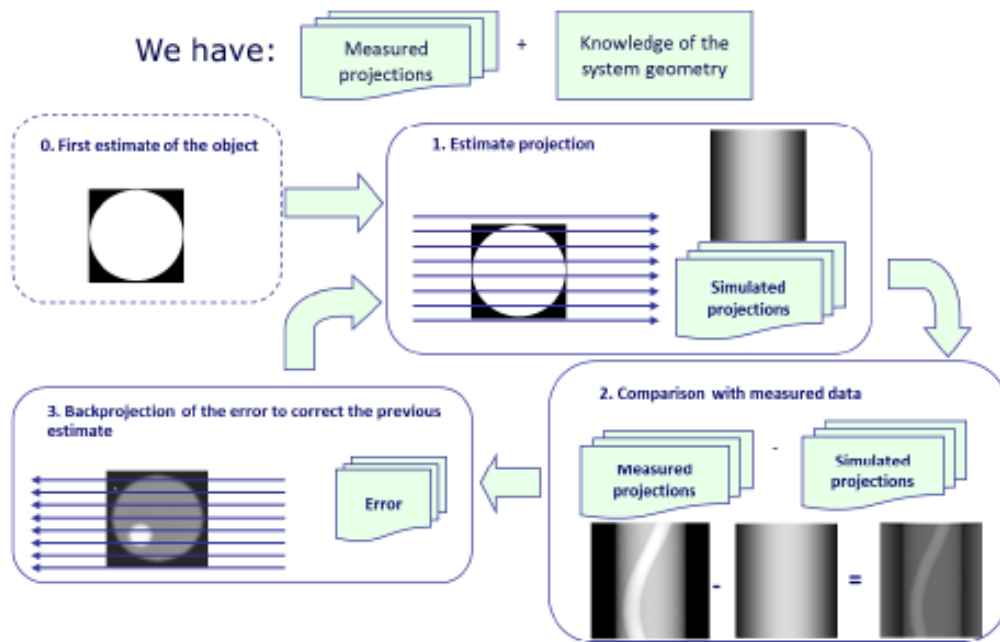


Figure 1-21: Scheme of the working mechanism of iterative reconstruction methods.

Although these methods are computationally expensive, their results are sometimes better than the analytical ones. If the number of projections acquired is scarce, or they have a lot of noise, the use of iterative methods is advisable. They provide a more complete view of the acquisition model not only based on geometry. It also allows the noise characterization when applying statistical methods (De Man *et al* 2001).

1.6 Beam hardening artifacts

Clinical CT images contain not only information of interest, which faithfully represent the objects we are interested in, but spurious or erroneous data that distort them. Depending on the randomness of the data, this superimposed and unwanted information may be called noise or artifact. Noise has a completely random nature while artifacts arise from systematic errors generated by problems in the imaging technique.

Artifacts are commonly encountered in CT images, and may obscure or simulate diverse pathologies. Beam hardening is a physics-based artifact.

There are two factors involving the origin of beam hardening artifacts: the polyenergy of the X-ray source, and the energy dependence of attenuation coefficients of tissues. The beam hardening effect is produced due to the increase of the mean energy of the X-ray beam as it passes through an object, i.e., the beam becomes “harder”. The concept lies in that lower energy photons are preferably absorbed. Therefore, the filtered beam has a greater distribution of high-energy photons which increase the mean energy of the beam resulting in low-attenuation artifacts (Brooks et al 1976).

Typical artifacts in beam hardening are *cupping* in homogeneous objects, and dark streaks between denser parts in heterogeneous objects (Figure 1-22). They become apparent in the reconstructed CT images, and may significantly impair the diagnostic quality of the image.

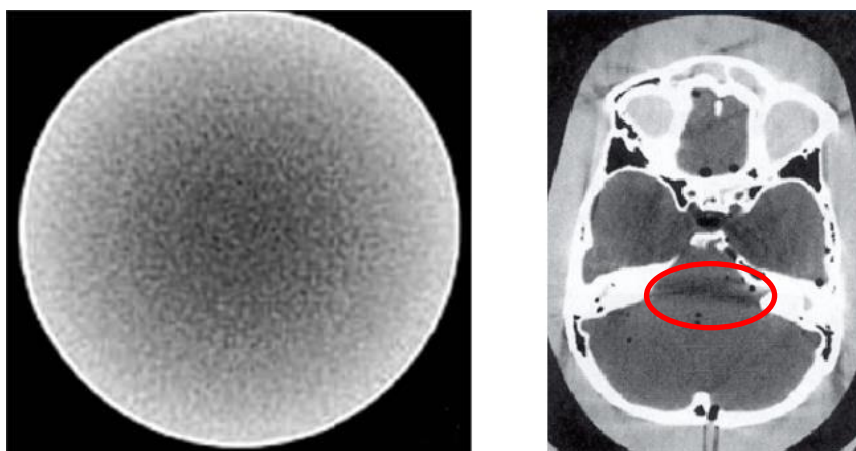


Figure 1-22: (Left) axial slice of a CT image of a homogeneous cylinder with cupping (the inner area is clearly darker than the outer part), and (right) base of a skull with dark streaks (bones have a higher atomic number than water).

1.6.1 Beam hardening characterization

Matter absorbs part of the energy of an X-ray beam as it passes through it. The attenuation suffered by the X-rays can be modelled according to Lambert-Beer law (1.9).

$$N_{out}(\varepsilon) = N_{in}(\varepsilon) \cdot e^{-\int_T \sum_i \mu_i(\varepsilon) dt} d\varepsilon \quad (1.9)$$

where $N_{in}(\varepsilon)$ is the photon number emitted by the source at a given voltage, $N_{out}(\varepsilon)$ the number of the remaining photons after passing through a material i with thickness t , and μ_i the attenuation coefficient of that material.

In the ideal case of a monochromatic source (1.10),

$$\mu_{total} = \int_T \sum_i \mu_i dt = \ln\left(\frac{N_{in}}{N_{out}}\right) = F_I(t) \quad (1.10)$$

where the ideal function F_I is the total attenuation suffered by the X-rays when passing through a given material with thickness t .

The ideal function is directly proportional to the material length traversed, as shown in Figure 1-23.

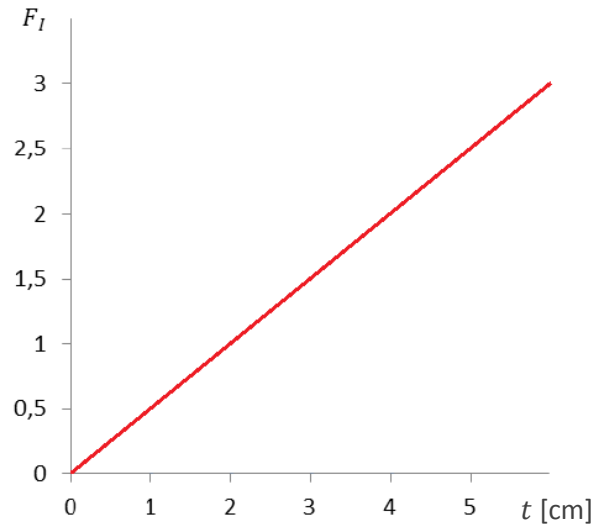


Figure 1-23: F_I , total attenuation of water when the X-ray source is monoenergetic at a voltage of 45KeV.

In the real case of a polychromatic source:

$$\int_T \sum_i \mu_i(\varepsilon) dt = \ln \left(\frac{N_{in}(\varepsilon)}{N_{out}(\varepsilon)} \right) = \ln \left[\frac{N_{in}(\varepsilon)}{N_{in}(\varepsilon) \cdot e^{-\int_T \sum_i \mu_i(\varepsilon) dt}} \right] = F_{BH} \quad (1.11)$$

where the real function or beam hardening function F_{BH} is the total attenuation suffered by the X-rays in the polyenergetic case, in which the measured attenuation does not depend linearly on the traversed material (Figure 1-24).

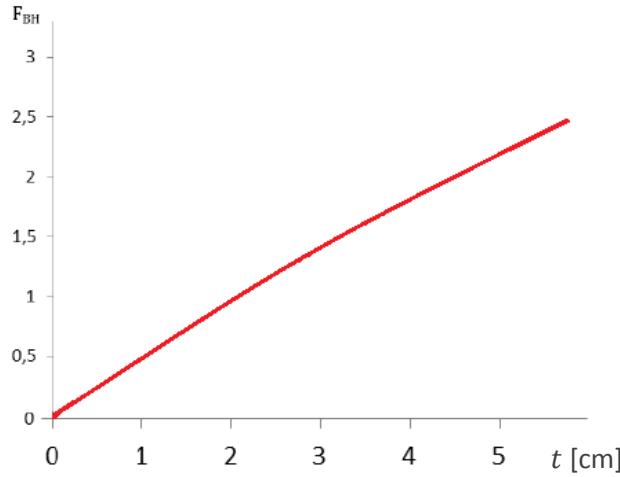


Figure 1-24: F_{BH} , total attenuation of water at 45KeV when the X-ray source is polyenergetic.

The attenuation coefficient of each material depends on the energy. Figure 1-25 shows a decrease in the attenuation as the photon energy increases. This means that the high-energy photons (the hard ones) are able to pass through the material more easily as they are barely absorbed.

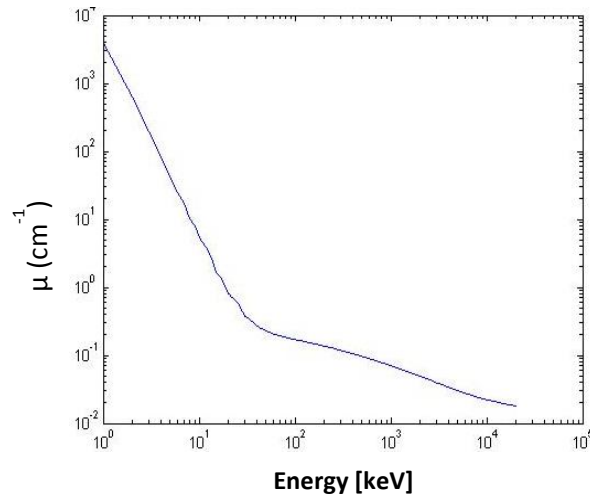


Figure 1-25: Energy dependence of attenuation coefficients of tissues $\mu(\epsilon)$.

As the beam passes through a given material, the energy spectrum distribution changes (Figure 1-26) because the low-energy photons are preferably absorbed. The mean energy of the beam increases, i.e., the beam is mainly composed of high-energy photons as it reaches the detector and thus, it is said that it got harder. The detector does not distinguish energies, it just detects the number of photons that reaches it, and considers them as if they all had the same energy.

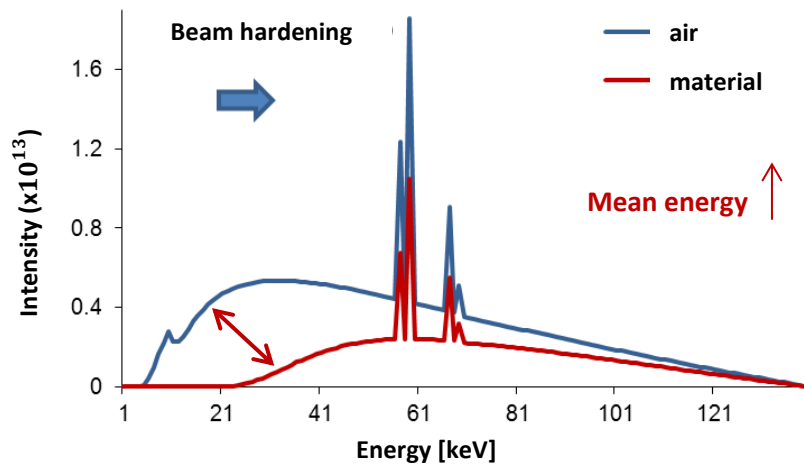


Figure 1-26: Energy spectrum of the photon number emitted by the source $N_{in}(\epsilon)$ (black line), and the same spectrum after traversing 4cm of water (blue line).

The detector does not distinguish energies, it just detects the number of photons that reaches it, and considers them as if they all had the same energy.

MOTIVATION AND OBJECTIVES

2 Motivation and objectives

2.1 Motivation

Visualization and quantification of the physiological function of identified small animal organs using molecular imaging techniques is proving to be a tool of valuable importance. The biomedical research community benefits from characterizing the behavioural phenotype of transgenic and knockout animals, the study of models of human diseases, and the discovery and development of new medicines and biochemical probes.

The largest number of human diseases models has been developed on rodents due to its genetic similarity to humans, as well as good knowledge of these models and low cost (Lewis *et al* 2002).

All these facts have driven the development and advancement of molecular imaging systems especially dedicated to small animal imaging. Nuclear imaging lies in the detection of the emission of gamma rays by a radiotracer. Low doses of radioactive substances are generally applied to glucose and injected into the study subject. These substances can be detected using special detection equipment such as PET (Positron Emission Tomography) and SPECT (Single Positron Emission Tomography). Images obtained with these techniques provide functional information, but are sometimes difficult to interpret due to an ambiguous location of the uptake of the radiotracer.

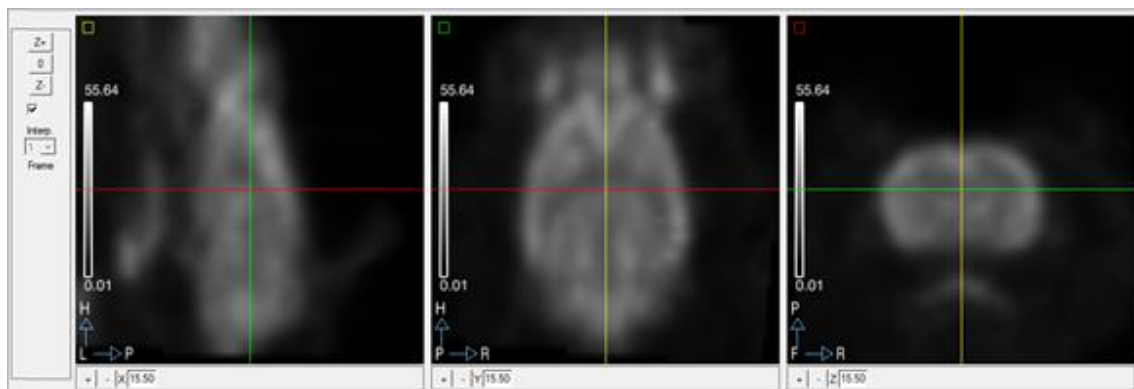


Figure 2-1: PET imaging of rat brain.

On the other side, micro-CT systems are the preferred technique to obtain high-resolution, three-dimensional, anatomical images of small laboratory animals such as rats and mice. These systems have proved to be effective in both soft-tissue tumour imaging and disease phenotyping in transgenic models. Micro-CT systems have been mostly used for bone imaging applications because of the high contrast obtained between soft tissue and bone. By using iodinated contrast agents, the image contrast can be significantly improved as well.

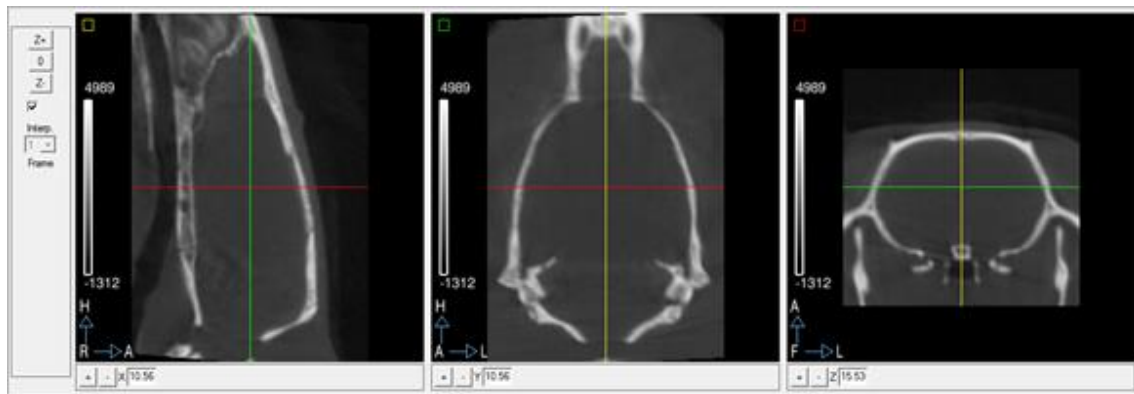


Figure 2-2: CT imaging of rat brain.

Multimodality imaging combines the functional information revealed from PET with the anatomical structures from the CT into one single image. It is remarkable the integration ease of these systems. This is the reason why the development of multimodal imaging systems has suffered from an exponential growth in recent years.

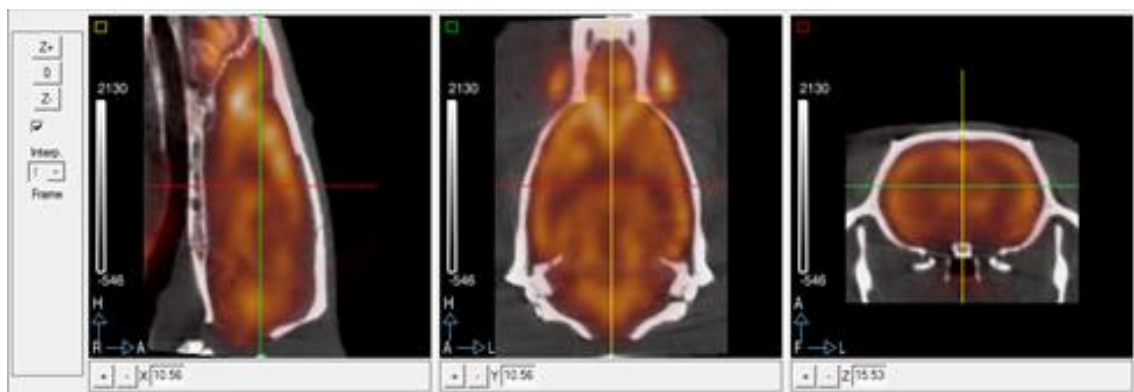


Figure 2-3: PET/CT imaging of rat brain.

Figure 2-3 shows the sagittal, coronal, and axial slices of a PET/CT of a rat brain study. The functional imaging (PET) takes advantage of the good location of the anatomical image (CT).

The work of this project falls within a research line that is being carried out by the Biomedical Imaging and Instrumentation Group of the University Carlos III de Madrid and the Instituto de Investigacion Sanitaria Gregorio Marañón.

Its aim is to design, develop and evaluate new systems of data acquisition, processing and reconstruction of multimodal images for applications in biomedical research. Within this research line, a high-resolution small animal CT has been developed which it is currently being commercialized worldwide by the Sociedad Española de Electromedicina y Calidad S.A. (SEDECAL: www.sedecal.com).

As explained in Chapter 1, a common type of CT artifacts is produced by the beam hardening phenomenon. These artifacts are not exclusive from clinical X-ray scanners, but also from small animal equipment like the system under study. In Figure 2-4 are exposed two images taken with the Argus micro-CT and which both present different artifacts produced by beam hardening. They seriously impair the qualitative and quantitative analysis of the images, making necessary the development of correction algorithms.

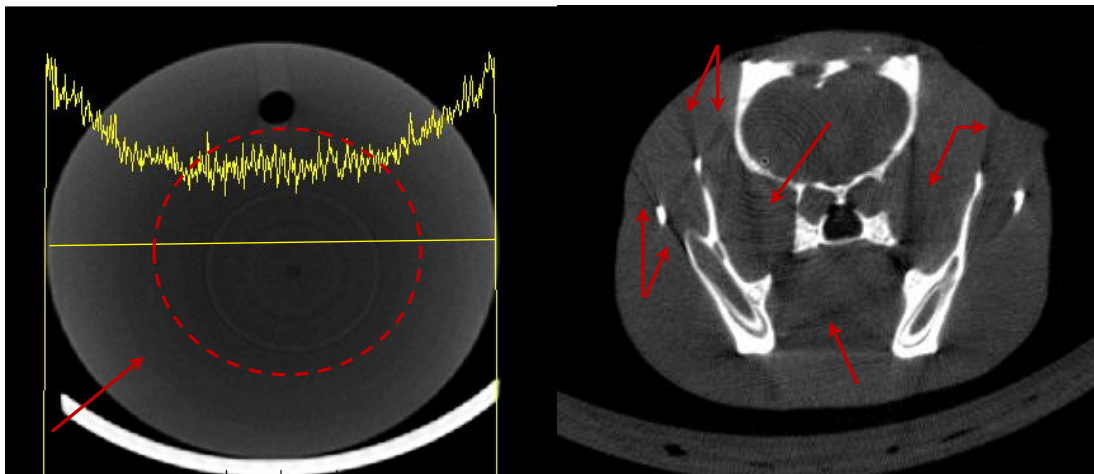


Figure 2-4: (Left) PMMA phantom suffering from cupping (darker area in the centre), and (right) head scan of a rat which shows dark streaks between its bones (red lines pointing).

There has been done some previous work about the topic in the laboratory (De Molina 2012), and the beam hardening correction methods proposed in the literature were revised [see bibliographic review in Appendix A]. Two methods were selected and developed: linearization and post-processing. Nowadays, they are in a preliminary version and they need to be integrated into the scanner.

2.2 Objectives

The main objective of this project lies in the incorporation of the correction of beam hardening artifacts into the Argus PET/CT by integrating the first and second order methods into the MMWKS.

This general objective is based on the following specific objectives:

1. Analysis of the system under study. The first phase is based on the in-depth examination of the micro-CT scanner for gaining a better understanding of the basic principles of operation, procurement processes, and data reconstruction.
2. Study of the user interface (MMWKS). The second phase comprises the understanding of the working mechanism of the console, as well as the communication protocols between the user PC (Windows operating system) and the control PC (Linux operating system).
3. Software implementation of the BH first order method which includes both the calibration and the correction.
4. Software implementation of the BH second order method which includes the correction.
5. Integration of the developed software into the system and evaluation.

2.3 Thesis structure

The thesis is organized in chapters as follows:

- **Chapter 1: Introduction.** This first chapter introduces the physical fundamentals of X-rays, and explains how they interact with matter, as well as its generation and detection. Next, the working mechanisms of computed tomography systems are presented followed by both the data acquisition and reconstruction processes. A brief classification of the most characteristic artifacts in reconstructed CT images is also shown. Last of all, a theoretical explanation of the origin of the beam hardening effect is exposed.
- **Chapter 2: Motivation and objectives.** In this chapter, the importance of computed tomography in preclinical research is highlighted, and the contextual framework of this project is presented. Finally, the objectives are defined.
- **Chapter 3: System under study:** This chapter offers the reader a general insight into the working environment of the project, and a better understanding of the tomographic system used.
- **Chapter 4: First order method:** This chapter faces the correction of cupping artifacts in homogeneous objects by implementing the first order correction method. The theoretical fundamentals of the linearization are exposed. The steps followed in order to reduce cupping artifacts from CT images, such as the design of the calibration phantom, and the calibration software for the multimodal console are explained. Then it is resumed with the analysis of the stability of the BH calibration parameters along the time, and the definition of a calibration protocol. The effectiveness of the implemented methods is evaluated.
- **Chapter 5: Second order method:** This chapter faces the correction of dark streaks in heterogeneous objects by implementing the second order correction method. The theoretical fundamentals of the post-processing correction are presented. The steps followed in order to reduce dark streaks between denser areas in CT images, such as the design of a calibration/test phantom, the

optimization of the second order correction parameters, and the design of the second order correction software are explained. To conclude, the effectiveness of the implemented methods is evaluated.

- **Chapter 6: Conclusions and future work.** This chapter emphasises the most significant results obtained throughout the project including some limitations which were encountered. It also outlines some future lines of work and makes suggestions for further research.
- **Appendix A:** Bibliographic review of the beam hardening correction methods
- **Appendix B:** '.ACT' header example
- **Appendix C:** '.HDR' header example
- **Bibliographic references**
- **Glossary of terms**
- **Project management**

In order to assess the correction methods in real systems, it has been used the available infrastructure at the UMCE from the Hospital General Universitario Gregorio Marañón, as well as some of the previously designed phantoms for the purpose. The animals used were maintained in the animal facility of the UMCE. All handling of animals was done according to the rules on protection of animals used for experimental purposes (Directive 86/609 / EEC and RD. 223/1998).

The software developed in this project will be integrated into preclinical, high-resolution equipment manufactured by the Spanish company SEDECAL S.A.

SYSTEM UNDER STUDY

3 System under study

Tomography system Argus PET/CT

The Argus PET/CT is a third generation, multimodal micro-CT designed to be integrated with nuclear imaging systems, PET and SPECT, and optical imaging (Figure 3-1).

The hardware is basically comprised of a microfocus X-ray source and a flat panel with CMOS technology and a microcolumnar CsI scintillator plate. The platform where the subject is placed is located in between them, and it is commonly known as bed. Thanks to the movement of the rotating ring, both the source and the detector rotate counter-clockwise around the bed acquiring projections at different angles.

The movement of the ring is managed by a control PC (general purpose machine AMD Opteron 242 1.6 GHz, 1 MB of RAM, Linux OS 2.4.21).

The X-ray tube (Apogee 5000 series, Oxford Instruments) comprises a tungsten anode, a beryllium window of $126\ \mu\text{m}$, and a focal size of $46.5\ \mu\text{m} \times 49.1\ \mu\text{m}$. It works from 0 to 50 keV with a maximum power of 50 W according to manufacturer's specifications.



Figure 3-1: Multimodal Argus PET/CT by SEDECAL.

The cone beam geometry that follows the X-ray source and the detector is represented in Figure 3-2.

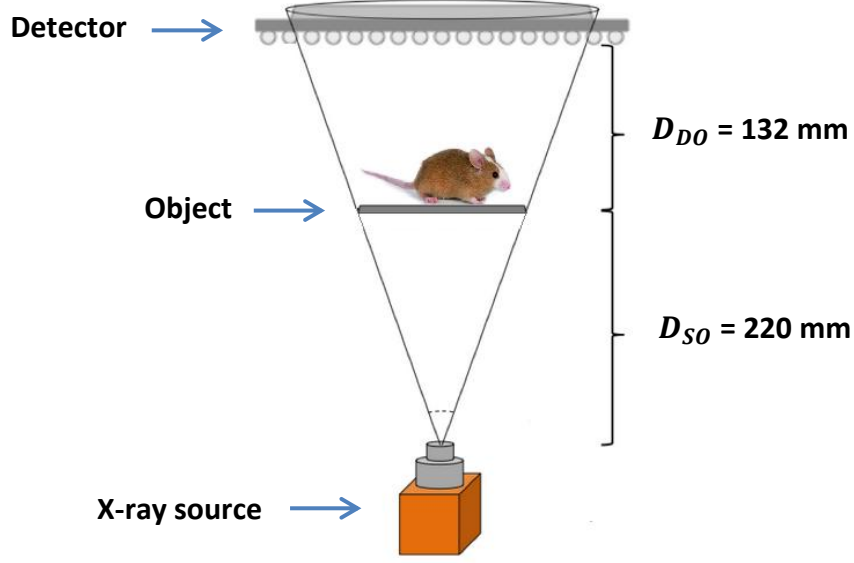


Figure 3-2: Schema of the geometry of the micro-CT system.

3.1 Generation of the X-ray image at the detector

In order to generate an X-ray image, a photon beam has to pass through an object. The detector counts the number of photons it receives (N_{out}) after crossing the given object, and relates them with the emitted number of photons (N_{in}) by the following expression:

$$N_{out} = N_{in} \cdot e^{-\int \mu(x) dx} + I_{dark} \quad (3.1)$$

where $\mu(x)$ is the linear attenuation coefficient of the object, and I_{dark} is the dark current received at the detector when the source is off. This small electric current, also referred to as reverse bias leakage current, flows even when no photons are entering the device.

The number of emitted photons (N_{in}) can be found by acquiring in the absence of the object, but with the same parameters, and with the X-ray source on. The obtained image is known as “flood image” (N_{fill}).

$$N_{fill} = N_{in} \cdot e^{-\int 0 \cdot dx} + I_{dark} = N_{in} + I_{dark} \quad (3.2)$$

The linear attenuation coefficient can be expressed as:

$$\int \mu(x)dx = \ln\left(\frac{N_{in}}{N_{out}-I_{dark}}\right) = \ln\left(\frac{N_{fill}-I_{dark}}{N_{out}-I_{dark}}\right) \quad (3.3)$$

During the calibration process, the system registers in a file the precise positions of both dead and defective pixels in the detector which contain no information. Those faulty pixels can be corrected by interpolation when reconstructing the image.

Different stages of the generation of X-ray images at the detector are shown in the following figure.

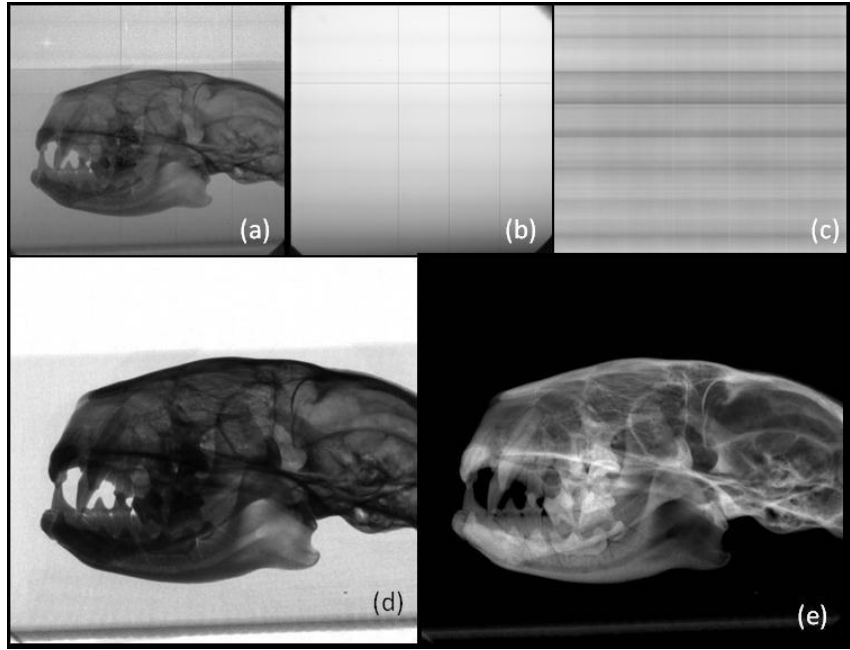


Figure 3-3: (a) N_{out} : raw data obtained at the detector, (b) N_{fill} : flood image (without the object), (c) I_{dark} : dark current image (X-ray source off), (d) $\int \mu(x)dx$: raw data obtained at the detector after correction (3.3), (e) attenuation image after applying the logarithm to (d).

A header file with extension '.ACT' is generated in every study [see example in Appendix B]. It contains the necessary information of the acquisition such as the voltage and current applied, the number of projections and their size, the scan angle, etc. Files with extension '.CTF' contain the projection data (unsigned int). The number of these files depends on the binning and the number of projections. For example, if binning=4 and number_of_projections=360, then a total of 2 '.CTF' files would be created. In the Table 3-1 are shown different possible configurations of the projection data files.

Binning	Pixel size	Projection size	Number of projections per '.CTF'
1	50 μm	2400x2400 pixels = 11 MB	30
2	100 μm	1200x1200 pixels = 2.74 MB	90
4	200 μm	600x600 pixels = 704 kB	180

Table 3-1: Possible configurations of the projection data files with extension '.CTF'.

3.2 Image reconstruction and visualization

The system is also equipped with a user PC which contains the multimodality workstation MMWKS (Pascau *et al* 2006), and the multi-bed reconstruction software Mongoose® (Abella *et al* 2011) based on the FDK analytical method (Feldkamp *et al* 1984). The software was completely designed in the Medical Imaging Laboratory.

The result of the reconstruction is a header file with extension '.HDR' [see example in Appendix C], and the reconstructed data is a file with extension '.IMG'. The header file contains relevant information from the reconstructed data such as information about the subject and some of the acquisition parameters (voltage and amperage of the source, number of projections, etc.).

The console facilitates the interaction between the user and the scanner when launching the acquisition. It also helps with the reconstruction, as well as with the visualization, management, segmentation, registration and analysis of the images once reconstructed.



Figure 3-4: Visualization of the sagittal, coronal and axial slices from a small animal CT study with the MMWKS console.

In order to acquire and reconstruct CT studies, a communication protocol between the user PC (Windows operating system) and the control PC (Linux operating system) is established.

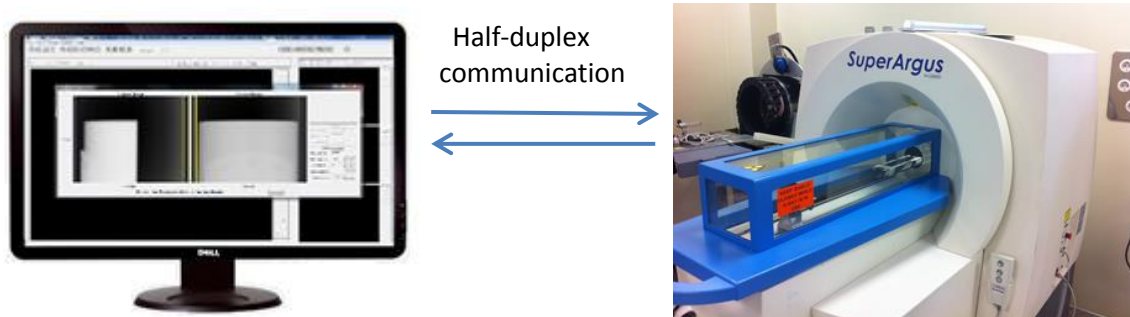


Figure 3-5: Schematic of the communication between the user PC and the control PC (placed inside the scanner).

FTP is the main communication protocol between them and it is used in order to interchange files from the control PC to the user PC.

By confidentiality issues, the exact communication protocols between the MMWKS and the scanner, as well as the state diagrams cannot be described in detail in this paper.

FIRST ORDER METHOD

4 First order method

First order correction can be achieved by linearization (Brooks et al 1976, Herman 1979, McDavid et al 1997). This method is one of the most used in order to reduce considerably the cupping artifact characteristic of homogeneous objects. It is assumed that all materials which form the object present similar attenuation properties to water (i.e., soft tissues). The algorithm is based on the conversion from the acquired projection with a polychromatic source into the projection that would have been acquired with an equivalent monochromatic one (also known as ideal source) in order to avoid nonlinearities. The linearization correction is available in the majority of the commercial scanners thanks to its simplicity.

4.1 Theoretical explanation

Human beings, as well as rodents, are essentially composed of soft tissue, which has attenuation characteristics similar to the water. Thus, for simplicity reasons, the object under study will be assumed to be composed only of water.

The linearization correction lies in the transformation of the beam hardening function F_{BH} into its corresponding ideal function F_I (Figure 4-1). F_I is lineal and directly proportional to the quantity of traversed water. Its slope corresponds to the effective mass attenuation coefficient of F_{BH} . This transform is known as the linearization function $T(x)$.

$$T(x) \equiv F_I(F_{BH}(t)) \quad (4.1)$$

where t corresponds to the quantity of traversed water (thickness), and x to the pixel value. Both $F_{BH}(t)$ and $F_I(t)$ can be obtained in an analytical way following (4.2) and (4.3) respectively:

$$F_{BH}(t) = \ln \left(\frac{\sum_{\varepsilon} N_0(\varepsilon)}{N_0(\varepsilon) \cdot \sum_{\varepsilon} e^{-\sum_{\varepsilon} m(\varepsilon) \cdot \rho \cdot t}} \right) \quad (4.2)$$

$$F_I(t) = m_{eff}(\varepsilon_{eff}) \cdot t \quad (4.3)$$

where $N_0(\varepsilon)$ is the intensity of the emitted X-rays, and $m(\varepsilon)$ the mass attenuation coefficients of the object under study.

In real scanners $N_0(\varepsilon)$ is not usually known. Therefore, $F_{BH}(t)$, $F_I(t)$, and $T(x)$ must be found out in an experimental manner.

Figure 4-1 shows the typical shape of the BH and the ideal functions.

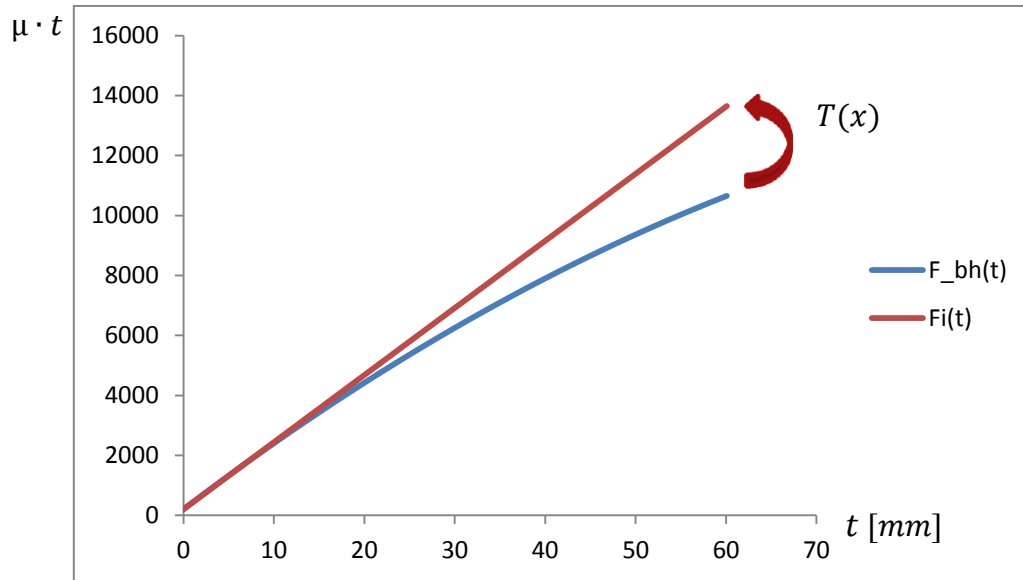


Figure 4-1: Representation of the beam hardening function $F_{BH}(t)$ and its corresponding ideal function $F_I(t)$.

The graphic indicates that for small quantities of water, both F_{BH} and F_I match together. For greater values, it is necessary to calibrate the measured attenuation values, as they are smaller than the real ones. Figure 4-2 represents the linearization function $T(x)$ needed in order to correct those values at different thicknesses

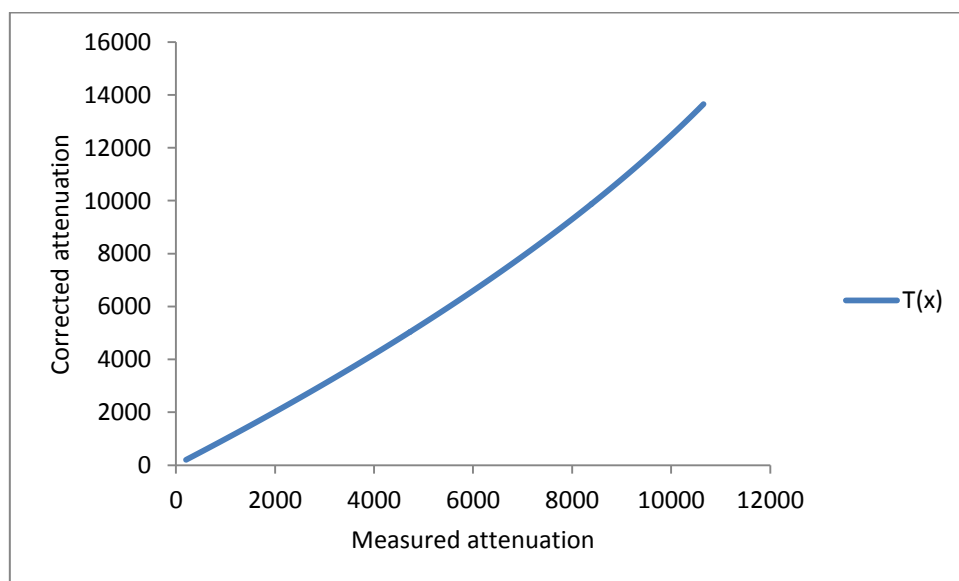


Figure 4-2: Linearization function.

This linearization function basically works as a look-up table which helps with the correction. Nonetheless, in order to speed up the correction, the function can be adjusted into a second order polynomial following the expression:

$$T(x) = \mathbf{a} \cdot x^2 + \mathbf{b} \cdot x + \mathbf{c} \quad (4.4)$$

The correction is done in the projection space as:

$$proj_{line} = \mathbf{a} \cdot proj_{or}^2 + \mathbf{b} \cdot proj_{or} + \mathbf{c} \quad (4.5)$$

So as to obtain \mathbf{a} , \mathbf{b} , and \mathbf{c} unknowns, a calibration procedure has been implemented.

4.2 Calibration

4.2.1 Design of the calibration phantom

In order to accurately reconstruct CT images correcting the first order beam hardening effect, it is needed to design and manufacture a calibration phantom. For this purpose, many considerations have to be taken into account: the optimal material and shape of the phantom, the cost, the range of penetration lengths, etc.

As explained before, the first order correction method takes already into account the homogeneity of the object under study, and it is based on the linearization of the beam hardening function F_{BH} into its ideal function F_I for different thicknesses.

4.2.1.1 Material

When talking about human beings, as well as animals, most of their composition is made out of soft tissue such as skin, fat, and blood. Soft tissues share similar spectral attenuation characteristics to water, and differ considerably from bone.

Thus, the homogeneous calibration phantom that simulates the human tissue and organs must have a mass attenuation coefficient similar to soft tissue, and therefore similar to water. In order to design it, we need to find a tissue equivalent material which has an approximate mass density $m_i(\varepsilon)$ of 1 g/cm^3 .

Poly methyl methacrylate (PPMA) is a strong, lightweight, transparent thermoplastic which belongs to the family of polymers, also known as acrylates. It is relatively

economical to be produced, and it has a mass density between $1.17 - 1.20 \text{ g/cm}^3$. Hence, it has multiple uses in the biomedical field such as intraocular lenses, dentures, and cosmetic surgery.

4.2.1.2 Shape

Another important consideration for the calibration phantom design is the shape. The aim is to get the maximum amount of penetration lengths when projecting the image's mask.

Intuitively, a triangular shape phantom will provide the most extensive range of measurements; small thicknesses when projecting the edges, and big thicknesses when projecting the centre. However, this geometry was discarded as its angular shape introduces many artifacts in the edges of the reconstructed image.

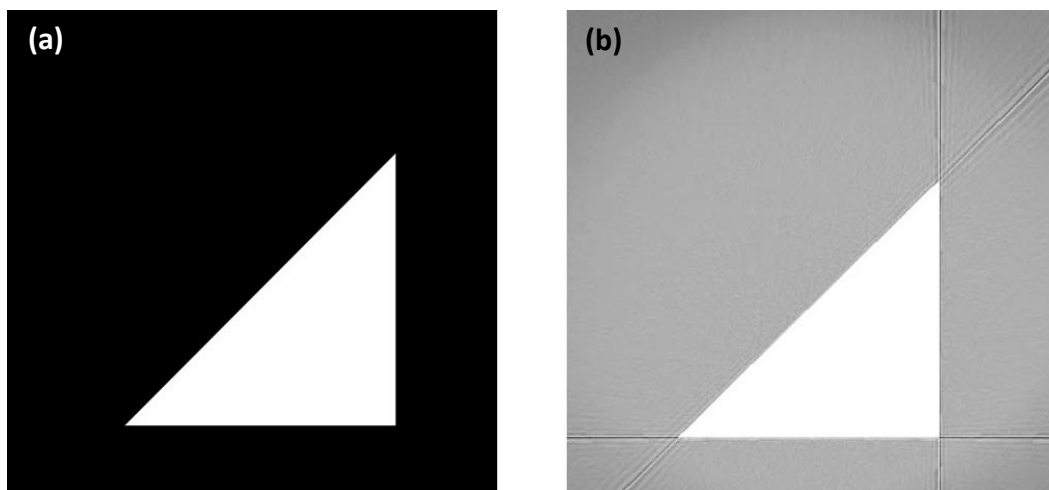


Figure 4-3: (a) Simulation of a triangular phantom, (b) reconstructed image of (a) showing artifacts due to the angular shape of the phantom.

In order to avoid these artifacts, the three edges are lightly smoothed turning into rounded corners. The outcome is a half cylinder which also offers small thicknesses but without producing the just mentioned reconstruction artifacts.

Following the more detailed analysis made in (De Molina 2012), it has been chosen a calibration phantom with a semi cylindrical shape.

4.2.1.3 Size

The size of the phantom must fulfil two requirements. On the one hand, it must be able to provide a fair amount of measurements for preclinical research, i.e., be able to cover any thickness range of tissue a rat may have. On the other hand, the phantom must be able to correctly fit inside the Argus PET/CT, and in the field of view (FOV).

After taking measurements of the micro-CT bed, it was decided that the half cylinder would have a height of 20 cm. The radius was chosen to be 3 cm as the maximum FOV corresponds to 6 cm.

4.2.1.4 Manufacture

Once decided the material, shape and size of the calibration phantom, a sketch was done in Matlab and it was sent to the manufacturers.

Two weeks later, the brand-new phantom designed at our Medical Imaging Laboratory and manufactured by Resopal (Madrid, Spain) is done and ready to start operating at the hospital.

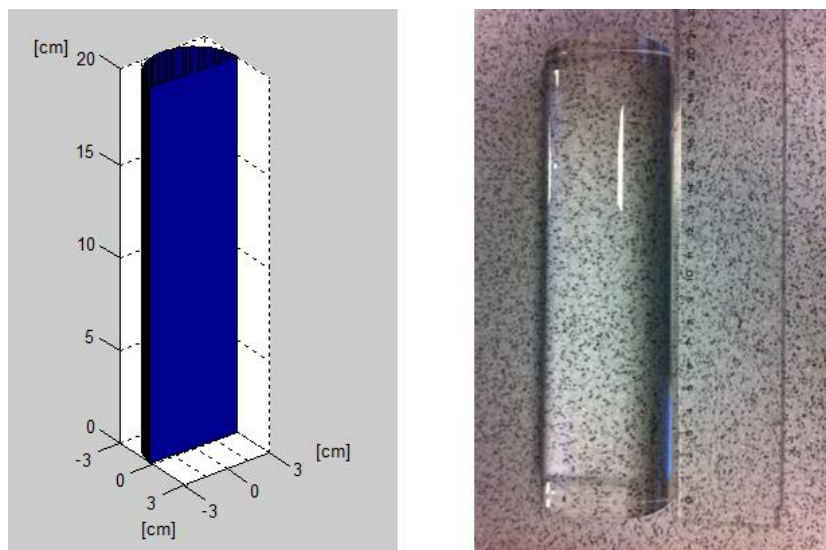


Figure 4-4: (Left) sketch of the calibration phantom done in Matlab and sent to the manufacturers, and (right) brand-new cylindrical PPMA calibration phantom.

4.2.2 Software development of the calibration procedure

The entire beam hardening calibration code was developed in Interactive Data Language (IDL) version 8.4. IDL is a programming language widely used for data analysis and medical imaging.

The calibration procedure has been divided into two steps: first acquisition, and then calibration.

On the one side, the acquisition is in charge of obtaining the projections of the calibration phantom at 360 angles. On the other side, the calibration is responsible of obtaining the parameters of the linearization function (equation 4.4) with which the projections will be corrected.

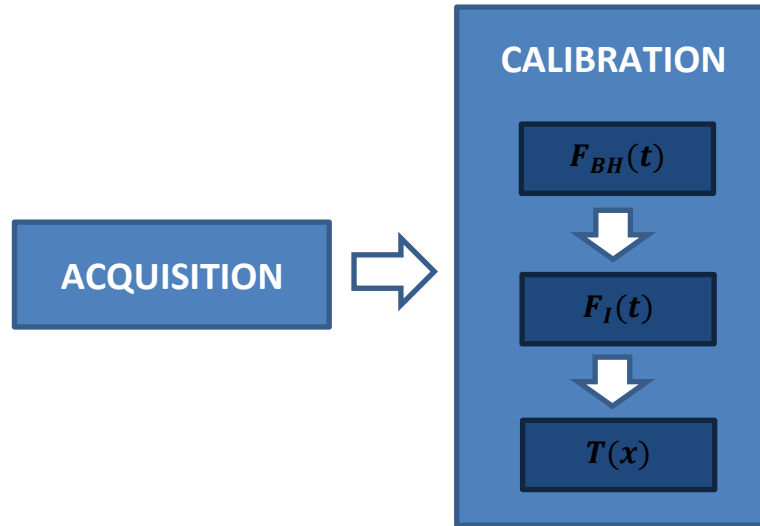


Figure 4-5: Block diagram of the calibration process.

- Acquisition module

Before obtaining the projections of the calibration phantom, it is necessary to make a scanogram. A scan, also known as scout, shows the sagittal and coronal views of the object under study, and helps the user to check if it is correctly placed in the bed and also to decide the acquisition ROI before the whole acquisition is made at 360 angles (instead of just 2). After checking the correct connection establishment between the user PC and the Argus scanner and that there are no security problems, the scan acquisition generates two different calls to the scanner. One for acquiring at $\theta = 0^\circ$ (which is responsible for the generation of the sagittal view), and another at $\theta = 90^\circ$ (coronal view).

Once the scanogram is obtained, we can set the acquisition parameters (voltage, current, etc.) and proceed with the complete acquisition (360°).

- **Calibration module**

$$F_{BH}(t)$$

- **CreaMascaraBH** is a prototype in charge of thresholding the reconstructed image of the calibration phantom by creating a mask (composed of ones and zeroes), and to project it. Every pixel from the mask projection is equivalent to another pixel from the calibration phantom projection at the same position. The value from each pixel corresponds to the thickness of the phantom (or amount of water) traversed by the X-rays.

It employs the following parameters:

- **maniqui_BH**: reconstructed image from the calibration phantom projections.
- **umbral**: value that separates the soft tissue from the air (in HU).

When the user is satisfied with the mask, the simulator will project it.

- **CreaCurvaBH** is a function that obtains the empirical beam hardening function $F_{BH}(t)$, without knowing the emission spectrum. We need to know the different amount of water traversed by the X-rays (Figure 4-6, x-axis → thickness t), and the corresponding total attenuation values (Figure 4-6, y-axis → attenuation per distance $\mu \cdot t$), i.e., the x-axis and y-axis from Figure 4-6 respectively.

It employs the following parameters:

- **proy_BH**: original projection data.
- **proy_mask**: projection data from the projected mask.
- **nbins**: number of samples from the generated function.
- **max_len**: diameter of the calibration phantom (in mm).

It returns **BHcurve**, which contains the empirical values of $F_{BH}(t)$.

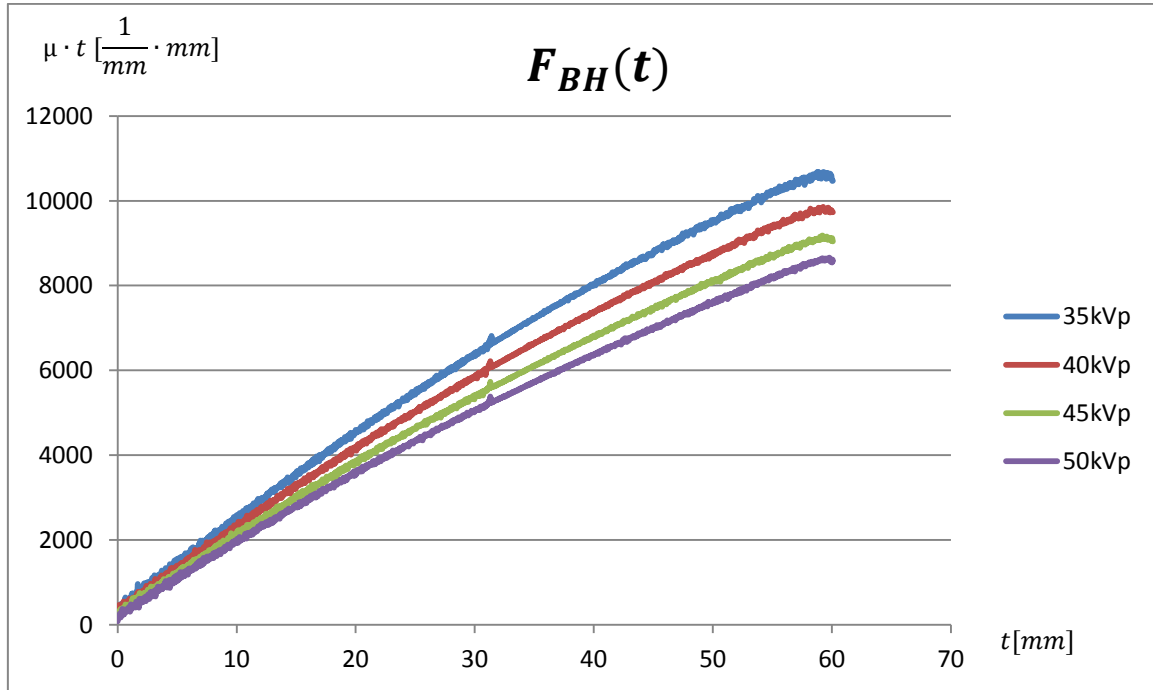


Figure 4-6: Empirical BH function $F_{BH}(t)$ obtained at different voltages.

$$F_I(t)$$

- **CalculaMacEfectivaSinEspectro** is a function that obtains the ideal function $F_I(t)$. First of all, the BH curve is fit into a polynomial function for reducing the noise. Afterwards, the first derivative is computed at $t = 0$, which corresponds to the slope of $F_I(t)$. However, it was found out that a more accurate tangent is obtained if using the mean of the first 7 points from the BH curve as the slope of the line. The independent term corresponds to the mean value from the projection air (the phantom's background).

It employs the parameters **proy_BH**, **proy_mask**, and **BHcurve**.

It returns **dev**, which contains the slope and the independent term of $F_I(t)$ (m, n), and the fit beam hardening function $F_{BH_{fit}}(t)$.

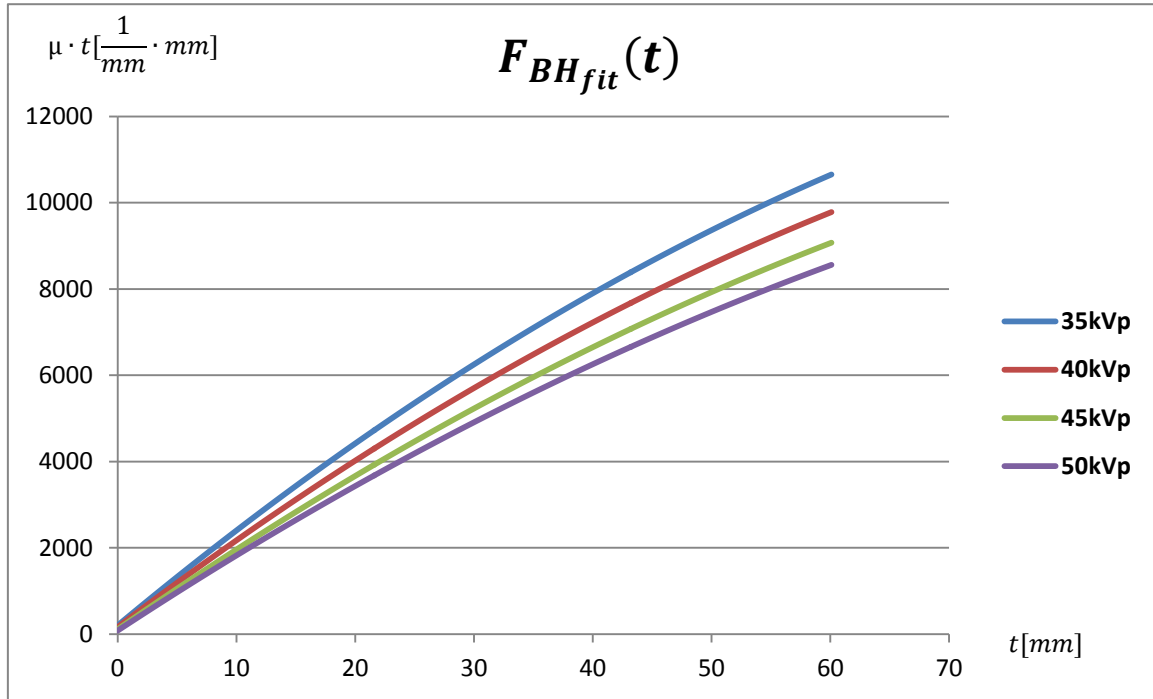


Figure 4-7: Fit BH function $F_{BH_{fit}}(t)$ computed for different voltages.

These BH functions show a similar pattern. Nevertheless, it can be checked out that the higher the voltage, the less beam hardening effect over the reconstructed images.

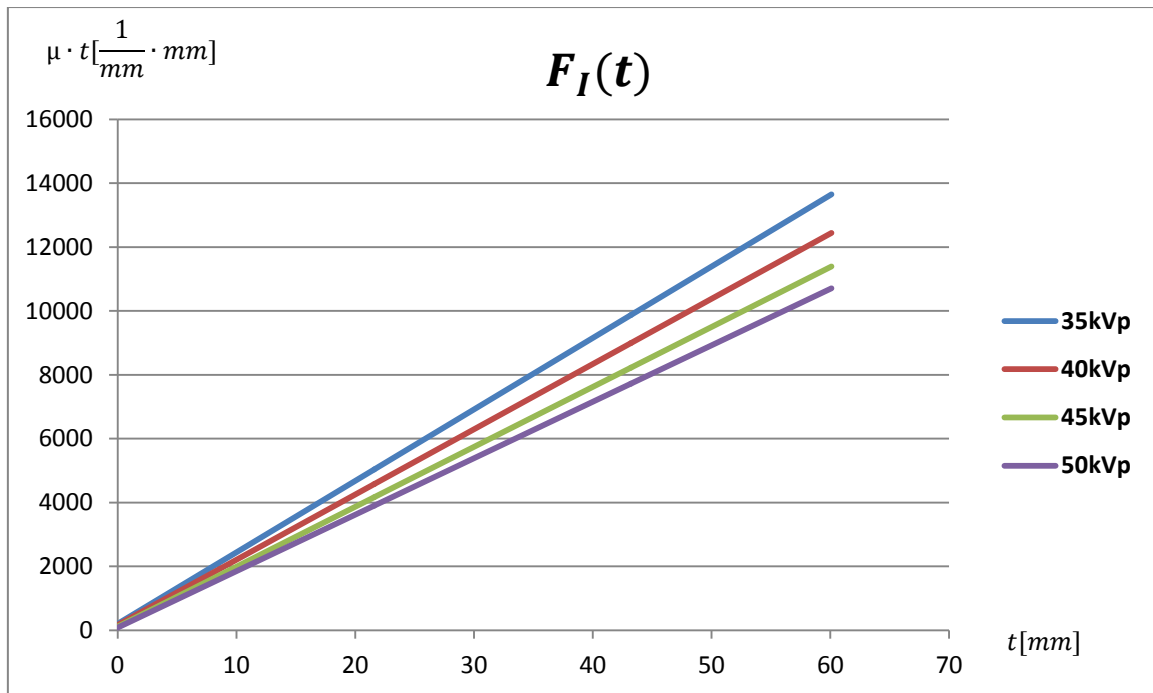


Figure 4-8: Ideal BH function $F_I(t)$ computed for different voltages.

$$T(x)$$

- **CreaCurvaLinealizacion** is a function that transforms $F_{BH_{fit}}(t)$ into $F_I(t)$ by transposing the curve.

It employs the parameters **BHcurve**, and **dev**.

It returns **result_pol**, which contains the three coefficients that define the linearization function, i.e., the ones which correct the first order BH artifacts. These coefficients are saved in a text file named 'coefs_cal_BH_voltage_X', where X corresponds to the voltage of the source in *kVp*. Apart from the calibration coefficients, this file contains the calibration date, and the acquisition file used (Figure 4-10).

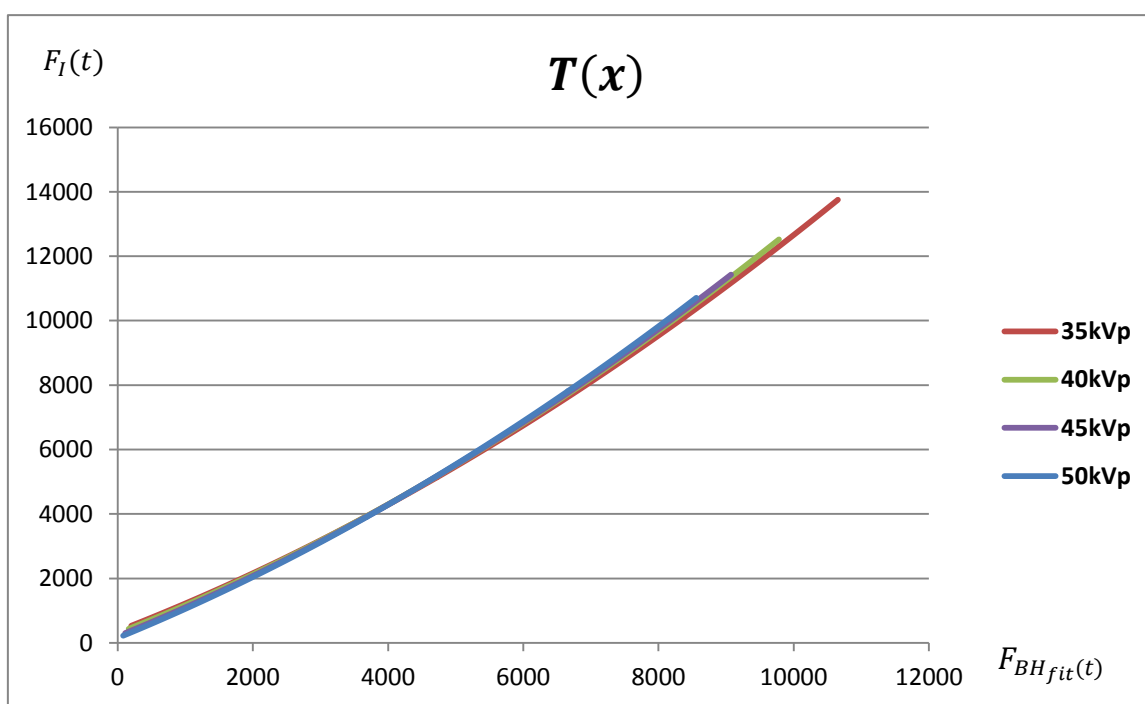
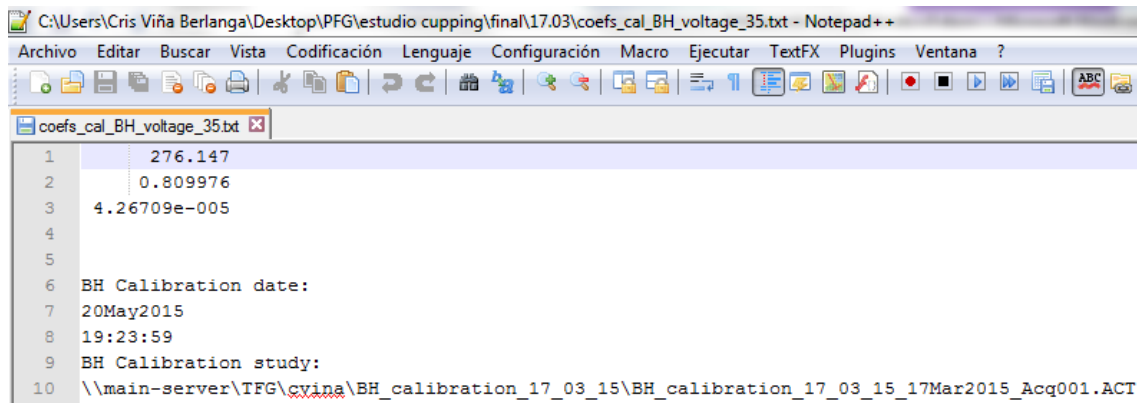


Figure 4-9: Transformed BH function $T(x)$ computed for different voltages.



```
C:\Users\Cris Viña Berlanga\Desktop\PFG\estudio cupping\final\17.03\coefs_cal_BH_voltage_35.txt - Notepad++
Archivo  Editar  Buscar  Vista  Codificación  Lenguaje  Configuración  Macro  Ejecutar  TextFX  Plugins  Ventana  ?
coefs_cal_BH_voltage_35.txt
1      276.147
2      0.809976
3      4.26709e-005
4
5
6  BH Calibration date:
7  20May2015
8  19:23:59
9  BH Calibration study:
10 \\main-server\TFG\cvina\BH_calibration_17_03_15\BH_calibration_17_03_15_17Mar2015_Acq001.ACT
```

Figure 4-10: Text file containing the calibration data and information from an acquisition made on the 17th of March 2015 at a voltage of 35 kVp.

4.2.3 Integration of the developed calibration software into the system

The functions described in the section above have been integrated into the user PC (MMWS console).

The following flow chart (Figure 4-11) represents the calibration process including the different interactions between the user PC and the control PC.

If the BH calibration interface is opened and the 'New plan button' pressed, the user PC will call the control PC in order to acquire two projections; one at 0 degrees and the other one at 90. The user PC keeps updated of the progress by reading a log and a progress files from the control PC (by FTP). Once the acquisition is finished, the '.out' files containing the projections are retrieved by using the same protocol, and the user PC changes the format to '.ctf'. Then the user set the acquisition parameters and press 'Proceed'. The user PC calls again the control PC but this time the scanner acquires at 360°. Once finished, the user PC retrieves the resulting file and converts it into a '.ctf' file and it also creates a header file with extension '.act' containing the acquisition parameters. Finally, the functions described in 4.2.2 are applied to the raw data so that the calibration parameters are obtained thanks to the linearization function. These parameters are saved in a '.txt' file. In case the file already existed, it would be overwritten.

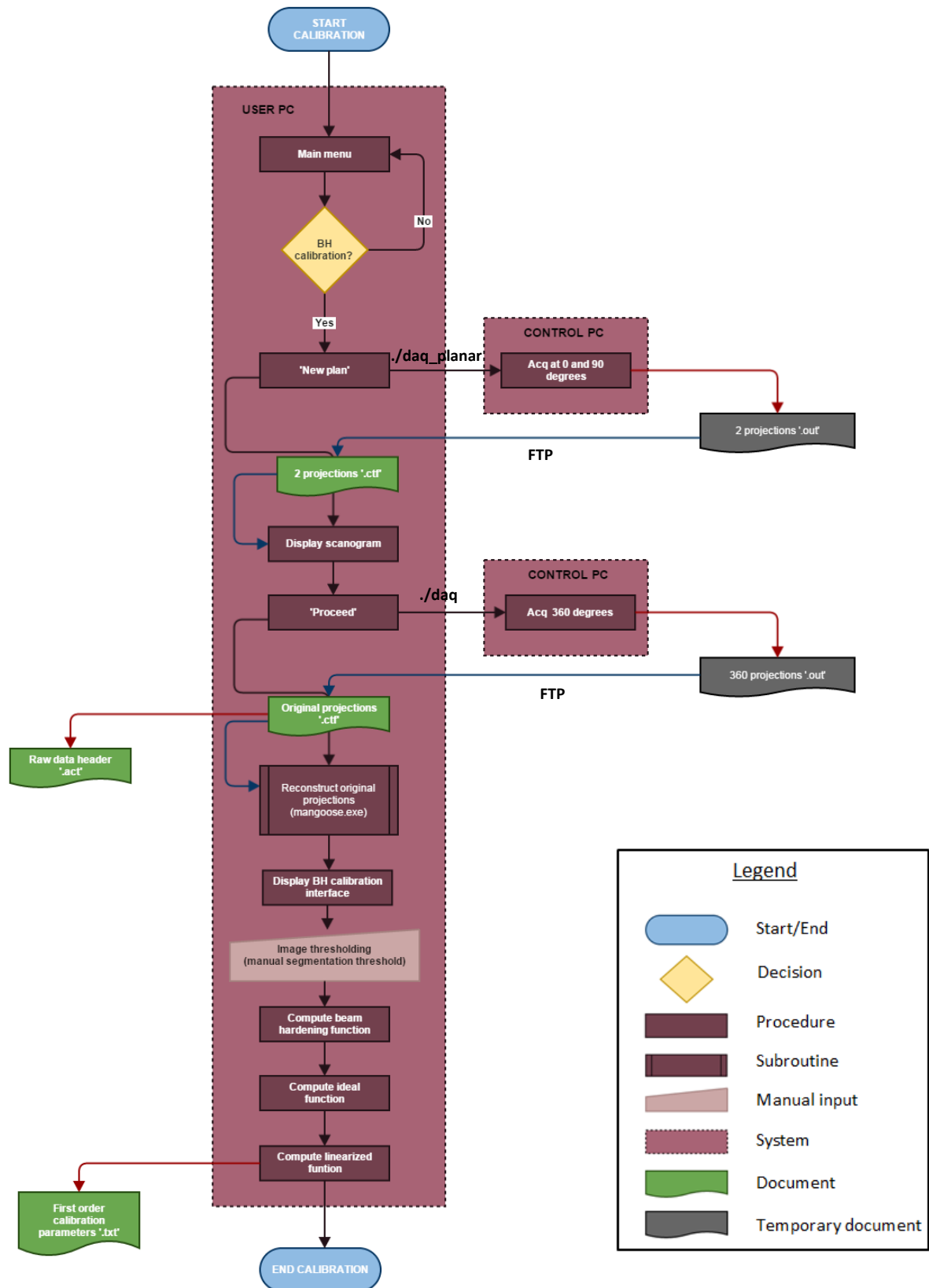


Figure 4-11: First order calibration flow chart.

4.2.4 Definition of a calibration protocol

In order to help the technical staff with the beam hardening calibration, the following protocol has been established.

4.2.4.1 Calibration phantom positioning

The phantom used for the BH calibration is a PPMA half cylinder with a radius of 3 cm, whose mass attenuation density is similar to the one of the water, and thus to soft tissue in general. The height of the phantom must range between 15 and 20 cm for stability reasons.

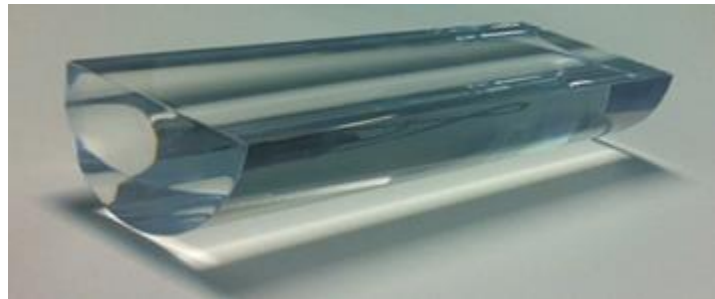


Figure 4-12: PPMA semi-cylindrical BH calibration phantom with a radius of 3 cm.

The technical staff must place the phantom in the scanner in such a way that a part of it sticks out of the bed as shown in Figure 4-13. The bed is not made out of the same material, and it has a different mass density. This fact would cause erroneous measurements of the quantity of traversed water by the X-rays (as they pass through the phantom and the bed). Moreover, it has to be centred in order to fit in the FOV.

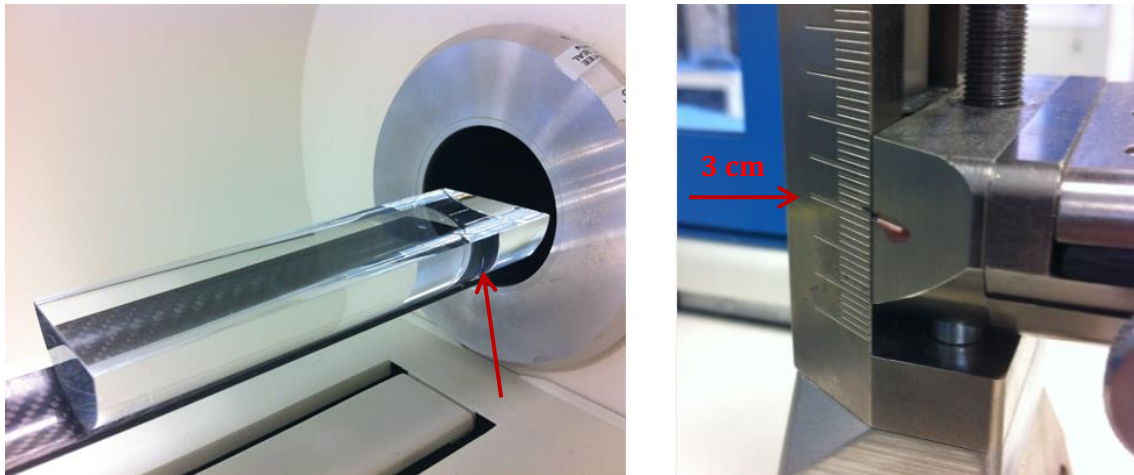


Figure 4-13: (Left) BH calibration phantom lying in the Argus PET/CT bed while the red arrow points to its end, and (right) guiding bed elevation at 3 cm.

4.2.4.2 Acquisitions

After placing the phantom in the scanner, the technical staff may launch the MMWKS console from the user PC (Figure 4-14). Once launched, the user may click in the ACQ button, and select the BH CALIBRATION option.

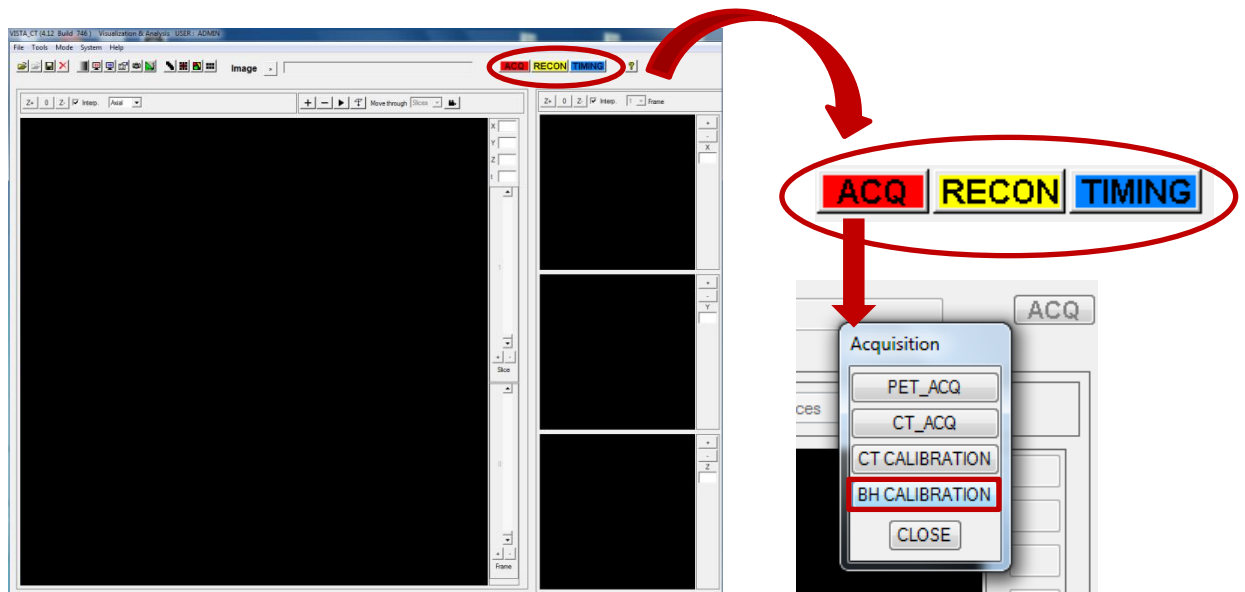


Figure 4-14: (Left) main menu of the MMWKS console, and (right) different acquisition options including the new BH CALIBRATION button.

The BH calibration interface (Figure 4-15) will open. The user must fill the empty fields related to the study information and where it is going to be saved. The initial bed position field is related with the depth in which the bed is introduced into the CT ring

for acquisition. By default, the value is set to 255 but the user can adjust it so that the central slice contains only the phantom (no bed). This can be checked with the scanogram by clicking 'New plan'.

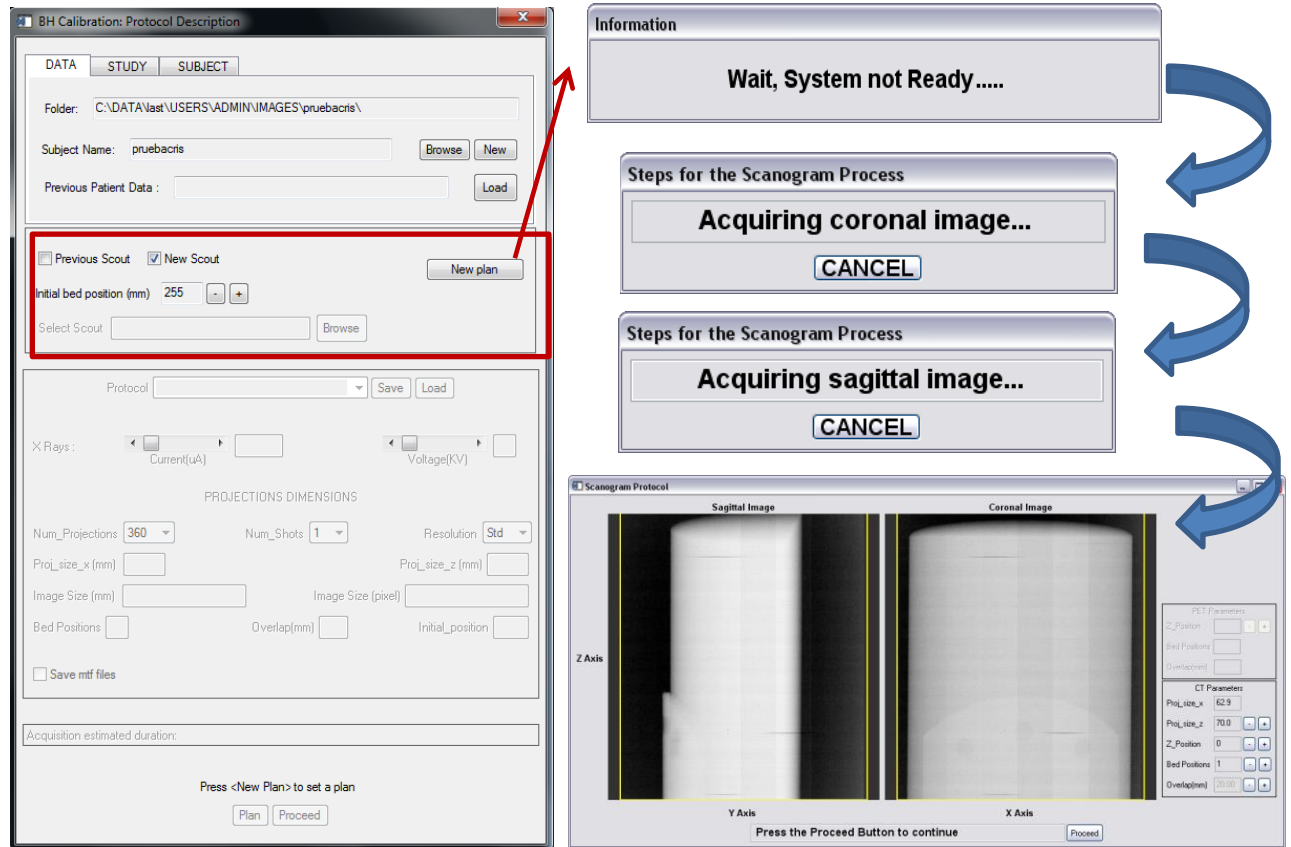


Figure 4-15: Sequential process for obtaining the scanogram: acquisitions at $0=0^\circ$ and $0=90^\circ$.

Once the scanogram is obtained, the user should proceed to set the acquisition parameters (Table 4-1), and to go on with the acquisition by clicking 'Proceed'. In the case the technician is displeased with the outcome, the scout could be repeated after rearranging the position of the calibration phantom.

Voltage (kVp)	Current (μ A)	Shots	Binning
35	240	8	4 (Standard)
40	240	8	4 (Standard)
45	240	8	4 (Standard)
50	200	8	4 (Standard)

Table 4-1: Acquisition parameters of the calibration phantom where the number of *shots* corresponds to the number of shots from the source in each angular position which will be averaged out in order to reduce noise, and *binning* corresponds to the resolution.

Right after the acquisition is finished, the mask segmentation interface will pop up. The user has to select now the segmentation mask that better adjust to the axial view of the semi cylinder. There is a sliding scroll bar at the bottom of the image that indicates the threshold for this purpose.

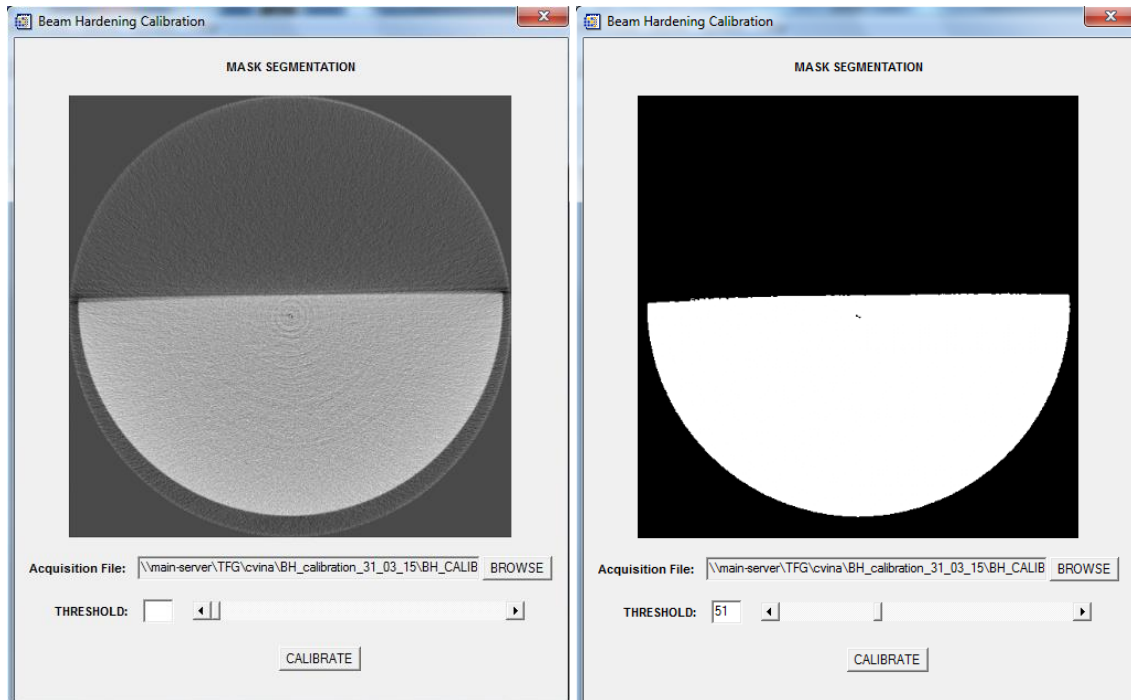


Figure 4-16: (Left) first order segmentation interface showing the central slice of the reconstructed volume, and (right) mask resulting from the segmentation of the same slice.

Once the calibration is finished, an informative pop-up window is displayed informing the user of the completion of the procedure (Figure 4-17). The calibration phase takes less than a minute. The micro-CT scanner is then ready to be used, and the first order correction can be applied to new reconstructions. For this, it is just necessary to click in the RECON button of the main panel, and access the reconstruction interface.

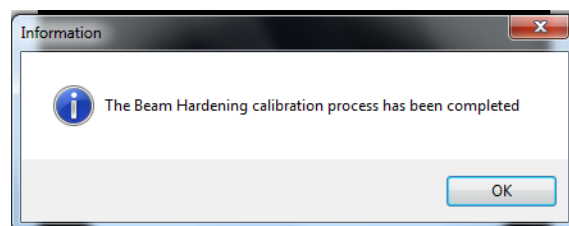


Figure 4-17: Pop-up window informing the user about the successful completion of the BH calibration.

4.3 Correction

The correction is based on applying the linearization function to each projection pixel by pixel.

4.3.1 Software development and integration of the first order correction procedure

For the implementation of the first order BH correction into the MMWKS, it has been made use of the already integrated reconstruction interface. A new drop-down list has been added. This list will keep insensitive until a first BH calibration has been made. The voltage at which the image we want to reconstruct was acquired should match the text file named 'coefs_cal_BH_voltage_X'. In that case, the list becomes available to the user and the options 'None', 'First order correction', and 'Second order correction' are displayed. Once the reconstruction starts, if 'First order correction' is set, the reconstruction will take a different path rather than the normal workflow [see flow chart in Figure 5-9].

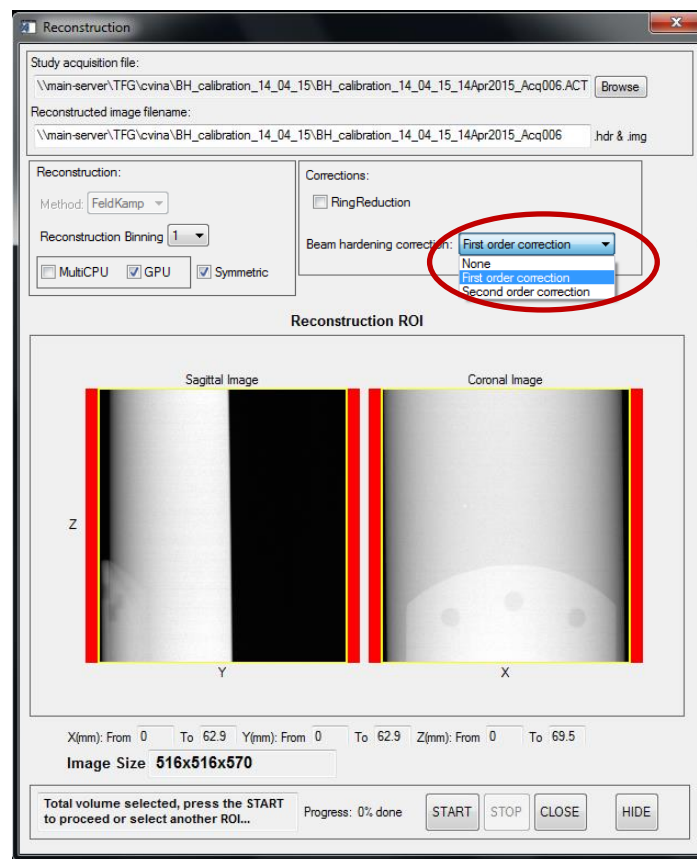


Figure 4-18: Reconstruction interface showing the new integrated BH correction options.

- **First order correction module**

- **BH_Correction_projection** is the only prototype in charge of correcting the cupping effect from the reconstructed images. Therefore, it reads the original projection data taken with the CT ($proj_{or}$) and corrects it by applying the BH calibration parameters as follows:

$$proj_{line} = coef3_{BH} \cdot (proj_{or})^2 + coef2_{BH} \cdot proj_{or} + coef1_{BH} \quad (4.6)$$

where $proj_{line}$ are the resulting linearized projection data.

It employs the following parameters:

- **path_act**: string with the directory path in which are the header file with extension '.act' and the data files with extension '.ctf' from the acquisition of the calibration phantom.
- **path_ct**: string with the directory path in which are the text files generated in the calibration.
- **coef1_BH, coef2_BH, and coef3_BH**: calibration parameters (coefficients a , b , and c from the linearization function (4.4)).

4.4 Evaluation

A pre-existing cylindrical PPMA phantom of 3 cm of radius with an inner perforation of 3.5 mm (radius) has been used for the testing of the first order correction method.

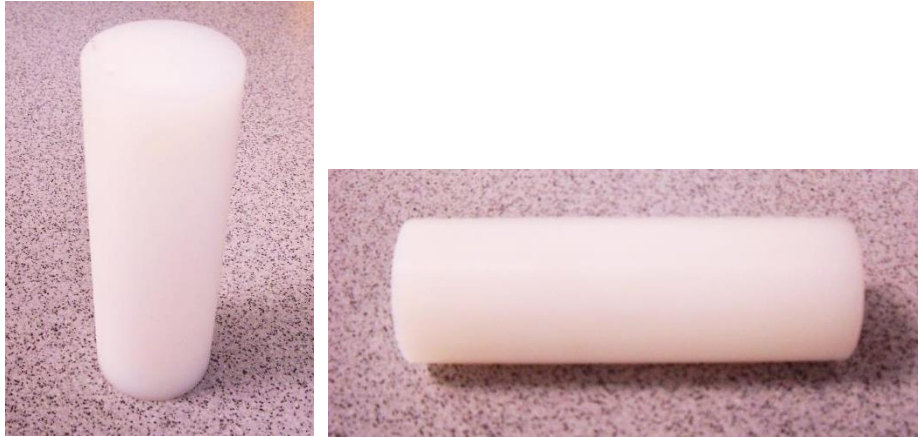


Figure 4-19: Cylindrical, homogeneous PMMA test phantom for the BH first order correction.

On the first place, four acquisitions are made at 35 *kVp*, 40 *kVp*, 45 *kVp*, and 50 *kVp* each. Afterwards, the projections at each voltage are corrected by applying their corresponding linearization curve obtained during the BH calibration. This process consists in correcting a set of 360 516x570 projections of the cylindrical phantom and took about a minute (GPU used). The result is shown in Figure 4-20.

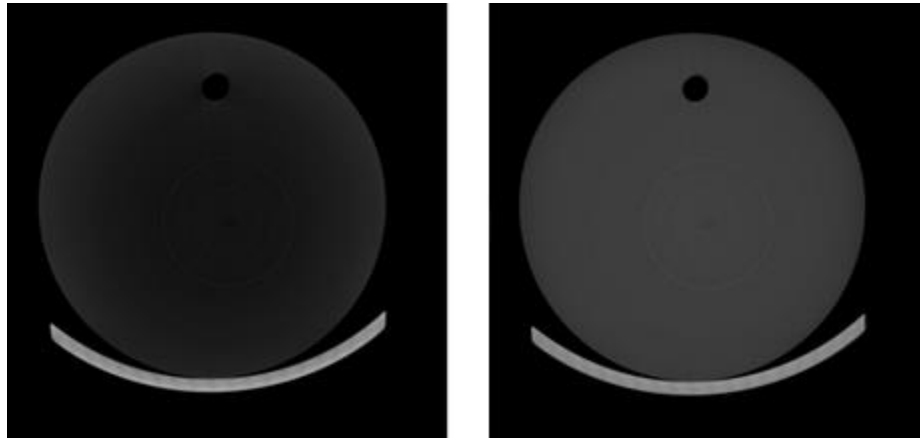


Figure 4-20: (Left) reconstructed projections without correction, and (right) same projections with first order correction.

Even if differences among them are just barely visible to the naked eye, the following schema shows what is really happening when tracing a profile.

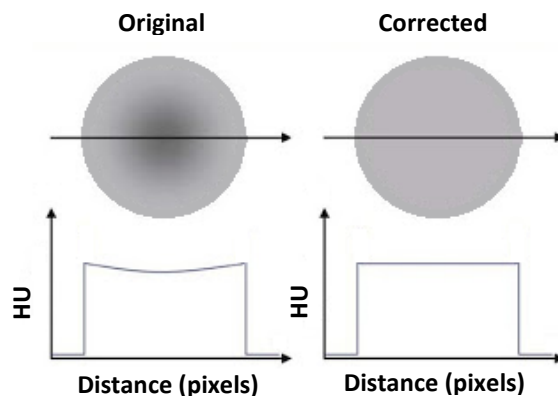


Figure 4-21: Profile representation of the cupping artifact and its correction.

Therefore, in order to assess the cupping reduction, we need to evaluate the cupping effect in both the original and the corrected profiles. Two techniques

have been followed. The most intuitive one consists in calculating the area in between the original and the ideal curves (A_{or}), and the area in between the corrected and the ideal curves (A_{corr}).

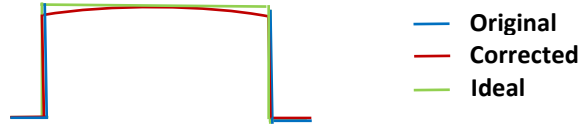


Figure 4-22: Sketch of cupping profiles.

The following formula expresses the cupping reduction which was achieved by applying the linearization method.

$$CR = \left(\frac{|A_{or}| - |A_{corr}|}{|A_{or}|} \right) \cdot 100\% \quad (4.7)$$

Nevertheless this formula cannot take into account over correction. The other way consists in determining the cupping effect of both the original and the corrected image with respect to the ideal profile.

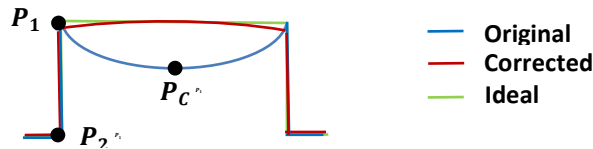


Figure 4-23: Sketch of cupping profiles with points for the analytical computation of the cupping effect.

where P_1 is the point with minimum beam hardening effect (uppermost edge of the profile), P_c is the point with maximum artifact (central part of the cylinder), and P_2 is the background value (bottom edge).

The following formula expresses the cupping effect over a profile.

$$CE = \frac{P_1 - P_c}{P_1 - P_2} \cdot 100 \% \quad (4.8)$$

Figure 4-24 shows a comparison of profiles obtained from both the original image and the corrected image.

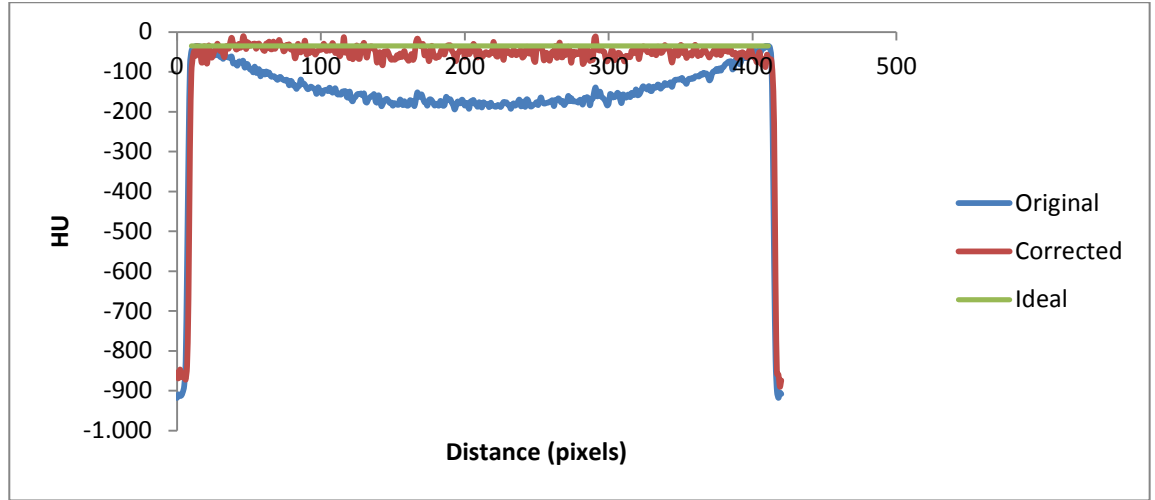


Figure 4-24: Profiles of the reconstruction of a homogeneous cylindrical phantom before and after the first order correction, as well as the ideal correction profile. The acquisition parameters were 35 kVp, 240 μ A, 360 projections, binning 4, and 8 shots.

Applying equation 4.7, it has been measured that the cupping effect was reduced an 83.78 %. Applying equation 4.8, it was determined that the original image was suffering a maximum cupping effect of 16.48 %, as opposed to the 2.64 % cupping on the corrected image. Therefore, by using a simple rule of three (4.9), the cupping correction was an 83.98 %. These percentages have been experimentally computed and may vary slightly due to the noisy nature of the images.

$$CR = \frac{CE_{or} - CE_{corr}}{CE_{or}} \cdot 100 \% \quad (4.9)$$

4.4.1 Evaluation of the stability of the BH calibration parameters

For studying the stability of the BH calibration parameters, we have calibrated with the brand-new phantom and the implemented software. These calibrations have taken place along three different sessions every two weeks each.

The following tables contain the BH calibration parameters **a**, **b**, and **c** from the linearization function (4.4) corresponding to each of the calibrations made.

4.4.1.1 17th March 2015

Voltage (kVp)	a	b	c
35	4.27E-05	0.809976	276.147
40	4.46E-05	0.820322	247.016
45	4.49E-05	0.836918	228.721
50	4.54E-05	0.849504	173.428

Table 4-2: 17th March 2015: BH calibration parameters.**4.4.1.2** 31st March 2015

Voltage (kVp)	a	b	c
35	4.15E-05	0.814662	364.135
40	4.31E-05	0.827913	297.777
45	4.26E-05	0.850395	207.189
50	4.39E-05	0.857980	151.304

Table 4-3: 31st March 2015: BH calibration parameters.**4.4.1.3** 14th April 2015

Voltage (kVp)	a	b	c
35	4.32E-05	0.805665	311.999
40	4.53E-05	0.817739	269.301
45	4.52E-05	0.835777	219.927
50	4.56E-05	0.850953	143.368

Table 4-4: 14th April 2015: BH calibration parameters.

The following table shows the behaviour of the parameters as the voltage increases.

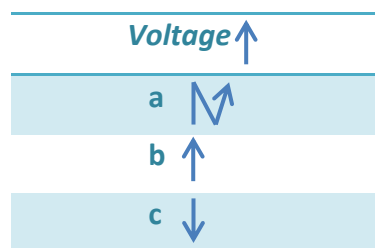
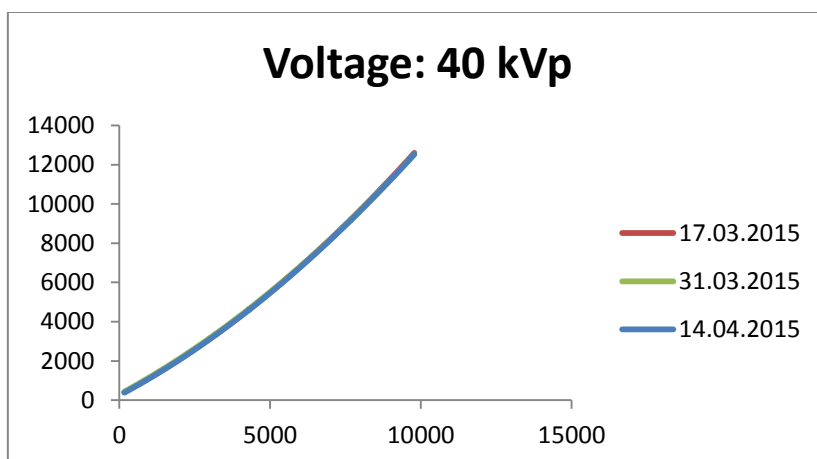
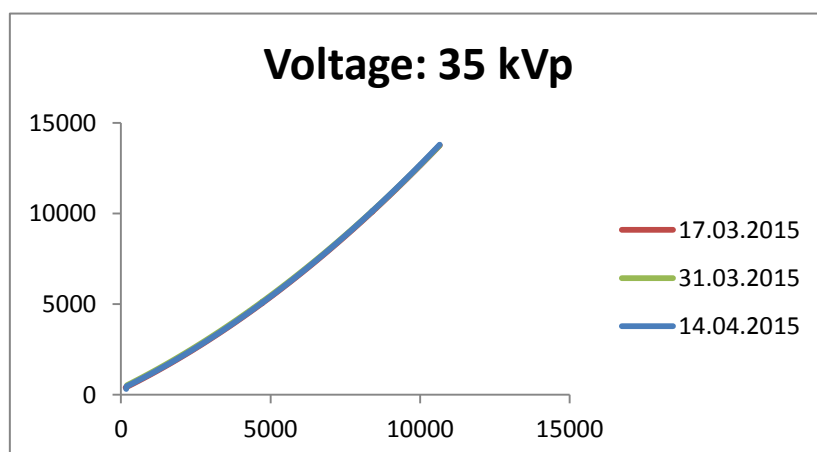


Table 4-5: Behaviour of the first order calibration parameters as the voltages increases.

By applying these values we can compute the second order polynomial that represents the linearization function for each of the voltages and compare them.



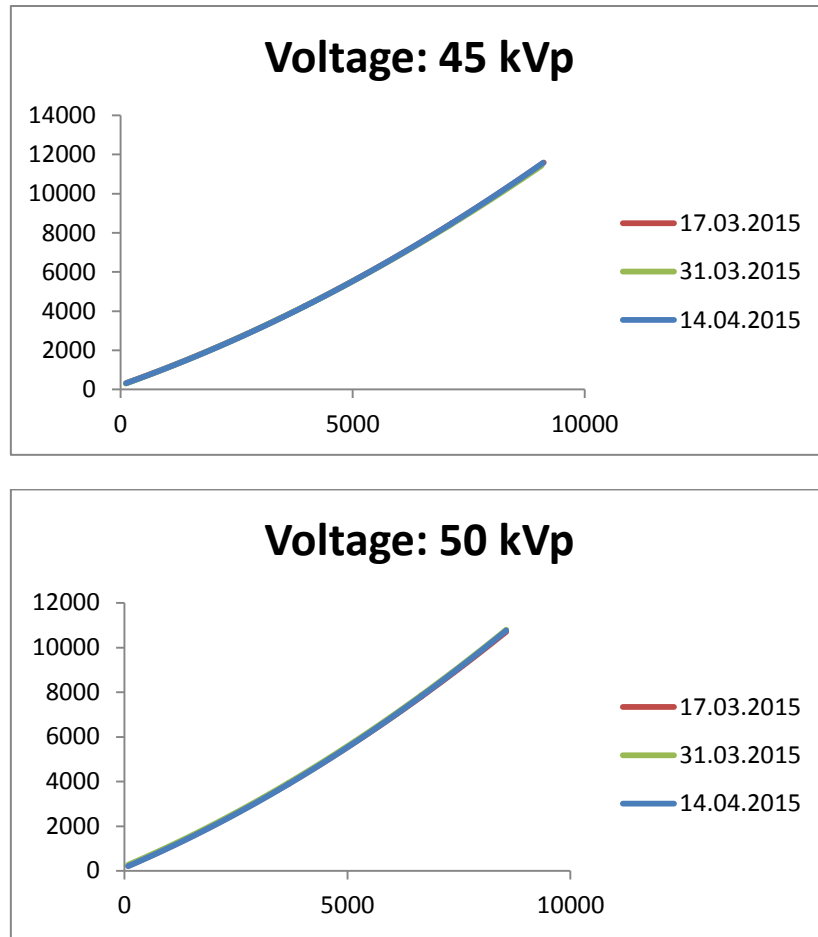


Figure 4-25: Linearization functions at a voltage of 35, 40, 45, and 50 kVp taken in different days.

As shown in these four graphics, the linearization functions for the same voltages match together. Therefore, it can be said that the calibration coefficients are stable. Nevertheless, it has been computed the mean and the standard deviation in order to quantify the stability.

	a	b	c
Mean (μ)	4.25E-05	8.1E-01	317.427
Standard deviation (σ)	8.74 E-07	4.5E-03	44.244

Table 4-6: Mean (μ) and standard deviation (σ) of the first order calibration parameters.

The standard deviation entails a 2.05 %, 0.055 %, and 13.93 % of their respective means for a , b , and c . However, this last measurement can be ignored as parameter c represents the background value, and it should always be zero. This variation is due to some problems with the HU calibration.

SECOND ORDER METHOD

5 Second order method

As explained in the bibliographic review of the beam hardening correction methods [Appendix A], the linearization method exposed in the previous chapter is not sufficient to correct dark streaks produced by the presence of denser objects within a volume. The existence of these objects, such as bones, is the common case seen in nature. Therefore, the importance of the artifact detection and correction is vital for the improvement of the imaging quality. The correction proposed in this paper is based on the theoretical study described in (Joseph *et al* 1978).

5.1 Theoretical explanation

This method assumes that the object under study is only composed of soft tissue and bone. It estimates the quantity of bone of the object in order to later correct it.

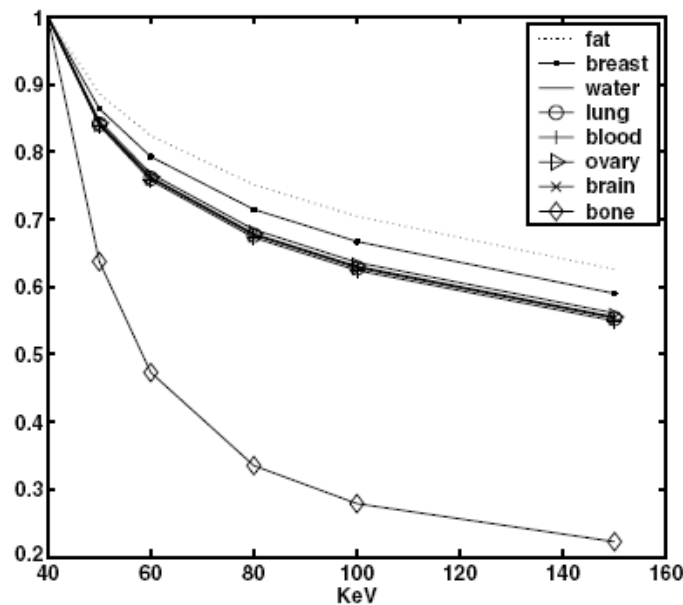


Figure 5-1: Mass attenuation coefficients for human tissues normalized at a voltage of 40 keV (Elbakri *et al* 2002).

The mass attenuation coefficients corresponding to soft tissues differ drastically from bone.

Taking into account this fact, a new beam hardening function can be developed from the formula shown in (4.2) and extended for different lineal combinations of water and bone:

$$F_{BH}(t_w, t_b) = \ln \left(\frac{\int N_0(\varepsilon) d\varepsilon}{\int N_0(\varepsilon) \cdot e^{-m_w(\varepsilon)t_w - m_b(\varepsilon)t_b} d\varepsilon} \right) \quad (5.1)$$

where $N_0(\varepsilon)$ is the intensity of the emitted X-rays, $m_w(\varepsilon)$ and $m_b(\varepsilon)$ the mass attenuation coefficients of water and bone respectively, and t_w and t_b corresponds to the quantity of traversed water and bone respectively.

Formula 5.1 requires the spectrum, and the process to obtain it from a scanner is really tedious. Therefore, $F_{BH}(t_w, t_b)$ must be estimated in a different manner.

There is a way of representing the dependency between the mass attenuation of the bone and the soft tissue within the same energy range.

$$\lambda(\varepsilon) = \frac{m_b(\varepsilon)}{m_w(\varepsilon)} \quad (5.2)$$

This relationship is graphically displayed in Figure 5-2.

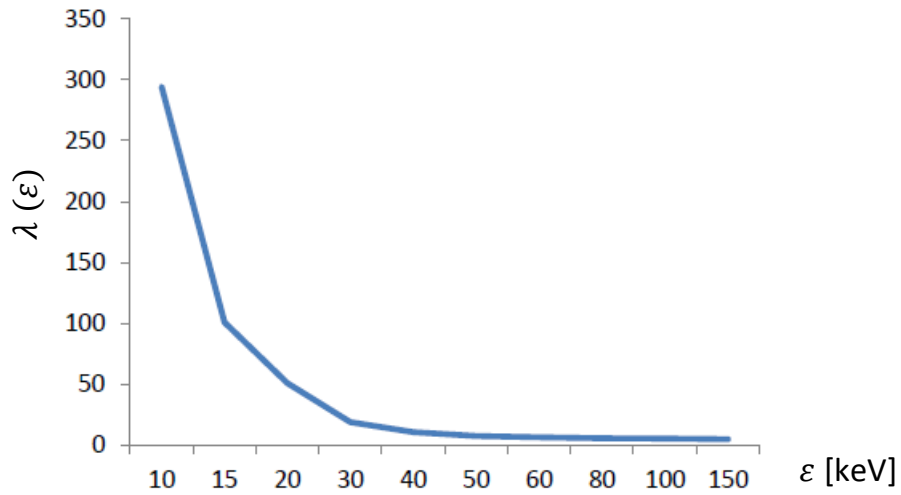


Figure 5-2: Representation of $\lambda(\varepsilon)$ expressing the dependency between the mass attenuation of the bone and the soft tissue within the same energy range

If λ was constant for all energies, that would mean that a gram of bone attenuates λ times more than a gram of water. Thus, the BH artifacts generated in CT would be corrected by simply scaling the bone according to λ .

$$t_e = t_w + \lambda \cdot t_b \quad (5.3)$$

where t_e is the thickness traversed by an X-ray only characterized in terms of effective water. The amount of effective water represents the amount of water that would cause the same effect than a certain amount of bone.

However, as seen in Figure 5-2, λ depends on the energy and it is not constant.

For the second order correction, it is proposed the implementation of the post-processing method outlined by Joseph and Spital [16]. The method is based on the transformation of the whole sample into 'equivalent water' (t_e) and to apply the linearization function $T(x)$ obtained during BH calibration process. To this end, it is necessary to find the amount of water that would have attenuation properties equivalent to the combination of traversed water and bone, so that:

$$F_{BH}(t_w, t_b) = F_{BH_{2D}}(t_w + \sigma(t_w, t_b), 0) = F_{BH}(t_e) \quad (5.4)$$

where the line integral of the equivalent water path is given by:

$$t_e = t_w + \sigma(t_w, t_b) \quad (5.5)$$

Following the ideas additionally proposed by [1] and [14], $\sigma(t_w, t_b)$ can be approximated to a second order polynomial (5.6) only dependent on the amount of bone traversed by the X-rays.

$$\sigma(t_w, t_b) = A \cdot t_b - B \cdot t_b^2 \quad (5.6)$$

The correction is done in the projection space as:

$$proj_{corr} = proj_{line} - \mathbf{A} \cdot proj_b + \mathbf{B} \cdot (proj_b)^2 \quad (5.7)$$

where $proj_{corr}$ corresponds to the corrected projection data, $proj_{line}$ is the linearized projection data, $proj_b$ is the bone projection data, and A and B refer to the correction constants obtained empirically. The value of B affects the correction of the dark streaks as well as the quantification in bone areas, while A is responsible of restoring the correct quantification in bone.

The following diagram shows the second order correction procedure:

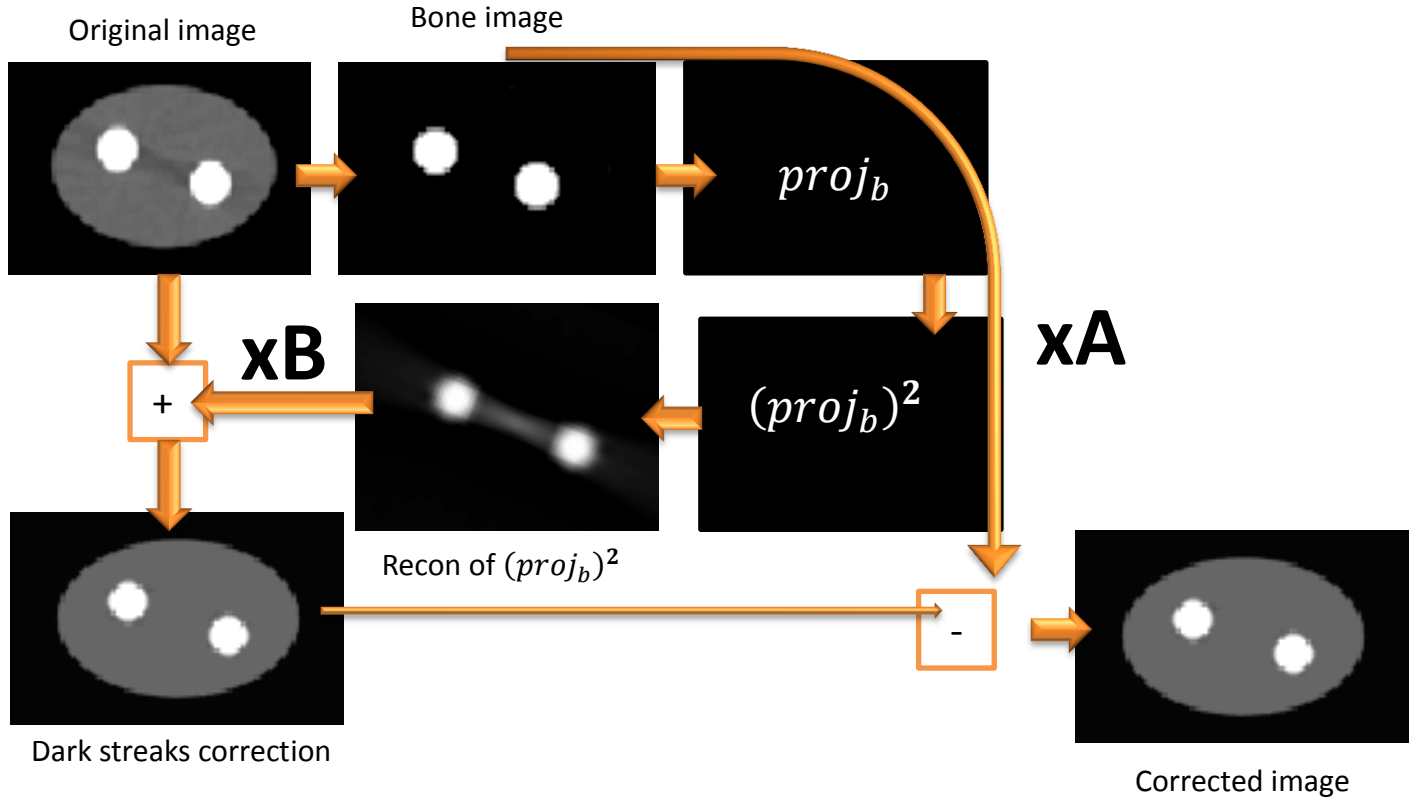


Figure 5-3: Diagram showing the second order correction procedure.

5.2 Calibration

As expressed in (5.7), the second order correction depends linearly on two parameters: \mathbf{A} , and \mathbf{B} . While \mathbf{B} is in charge of correcting the dark streaks between the bones, \mathbf{A} corrects the actual bone value avoiding overcorrection in the bone tissue pixels produced by the correction of the dark streaks.

These calibration parameters depend on the source voltage and on the amount of bone traversed by the X-rays. To minimize this last dependence, \mathbf{B} was modeled as a constant \mathbf{B}_x multiplied by the maximum value of the original projection and divided into the maximum value of the bone projection.

$$\mathbf{B} = \mathbf{B}_x * \frac{\max(\text{original_projection})}{\max(\text{bone_projection})} \quad (5.8)$$

In order to optimize the parameters \mathbf{A} and \mathbf{B} , and accurately determine their optimum values, it has been written a short Matlab code that creates a phantom and simulates the acquisition procedure with a polyenergetic source (so that the reconstructed images have BH artifacts). Afterwards, the phantom is iteratively corrected with

different values so that we can quantify the difference with the reference image (monoenergetic reconstruction) in terms of the mean square error (MSE).

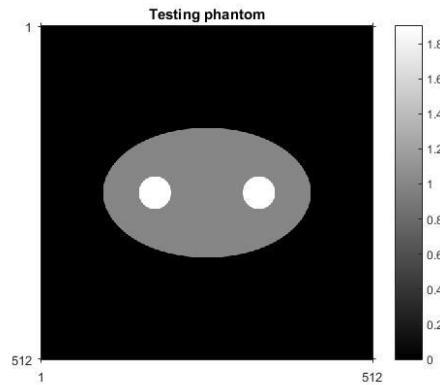


Figure 5-4: Second order calibration phantom simulated in Matlab.

To search for the optimum value of B_x , the MSE is calculated for the rectangle between the bone parts containing the dark streaks. For the case of A, the MSE is computed in the circular area inside the bone tissue. The procedure starts by setting both parameters to zero and fixing A. The correction will be made by using different B_x values which it is easily achieved with a loop (iteratively). Once drawn the graphic for a broad number of values, the point at which the MSE is lowest is chosen.

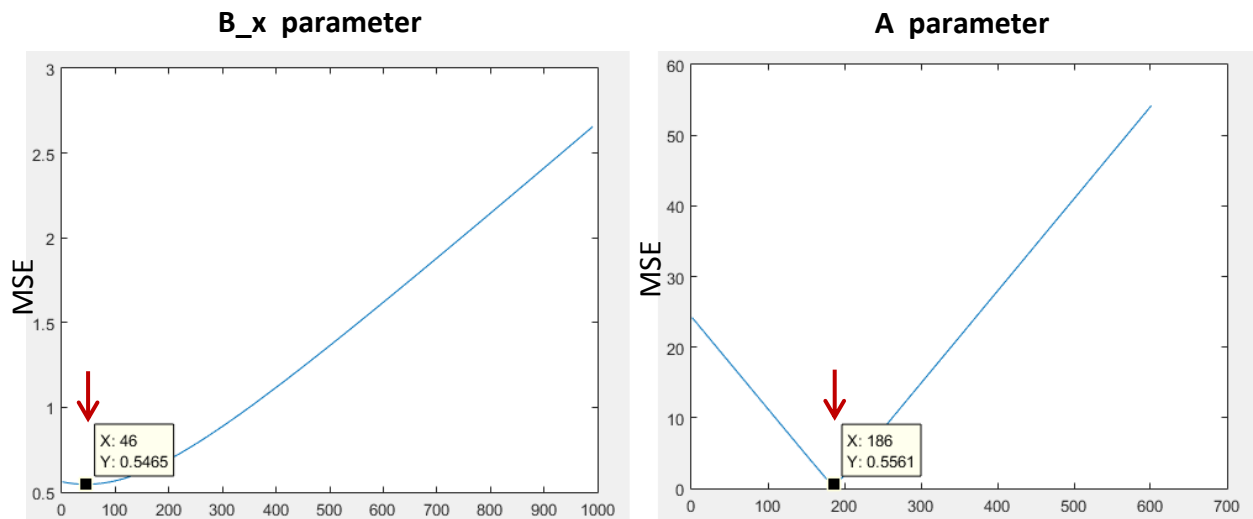


Figure 5-5: Matlab simulation for obtaining the MSE of the second order calibration parameters.

B_x parameter:

```
for B_x=0.00001:0.000001:0.001
    ➔ 0.00001 + 0.000001*46 = 0.000056
```

A parameter:

```
for A=0.4:0.001:1
    ➔ 0.4 + 0.001*186 = 0.586
```

The following values were obtained:

A	B_x
0.586	0.000056

Table 5-1: Resulting values of the second order correction parameters after computing the MSE iteratively in a Matlab simulation.

These values were taken for correcting the dark streaks in the reconstructed images.

Figure 5-6 shows five different reconstructions: the ideal case, with BH artifacts, corrected by just linearization, corrected by just post-processing, and corrected with both linearization and post-processing.

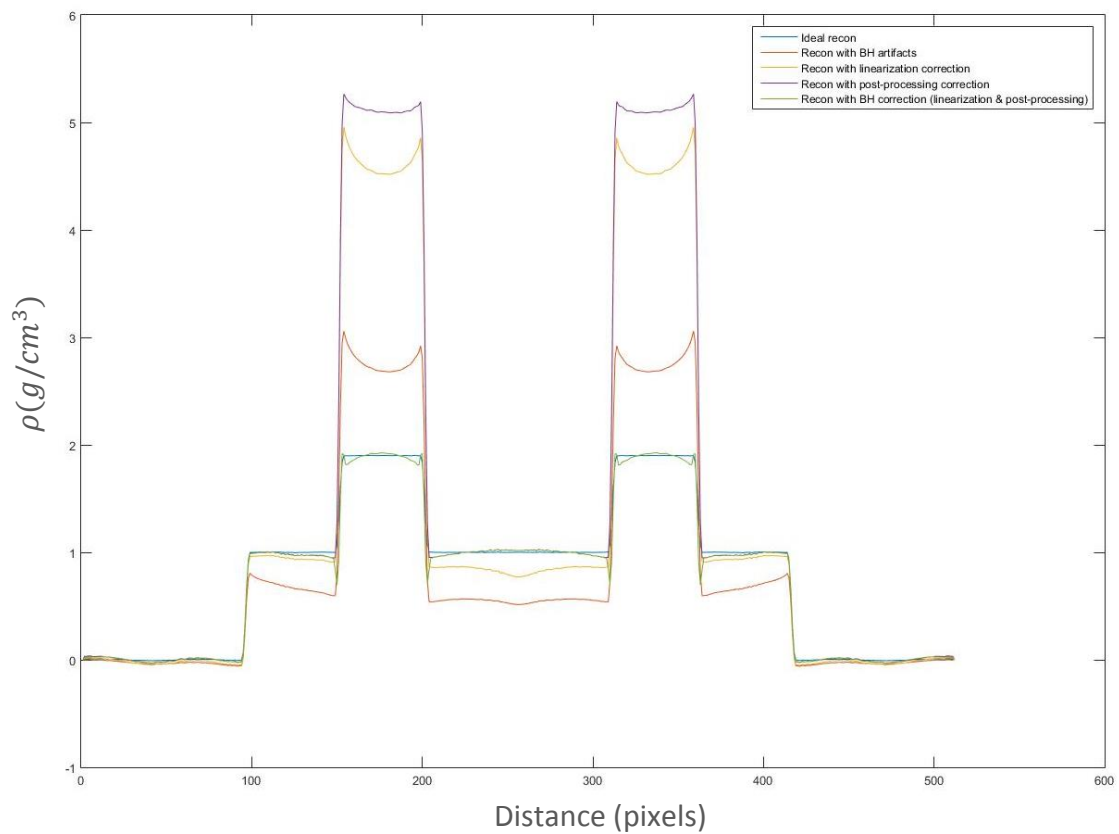


Figure 5-6: Different reconstruction profiles from a simulation (with and without correction).

5.2.1 Design of the calibration phantom

The second order BH correction method has been tested by using a phantom which must represent the combination of soft tissue ($m_i(\varepsilon) \approx 1 \text{ g/cm}^3$) and bone ($m_i(\varepsilon) \approx 1.8 \text{ g/cm}^3$).

In order to find the right solution, we have tried different concentrations of a mixed iodine and saline solution (Figure 5-7). The pixel values in each tube were compared against the pixel values in the bone of a reconstructed image of a rat. It was concluded that a combination of 60 units of an iodine solution (Iopamiro 300 mg/ml), and 40 units of a saline solution show the most equivalent attenuation coefficient values with respect to bone in diverse rodents' studies.

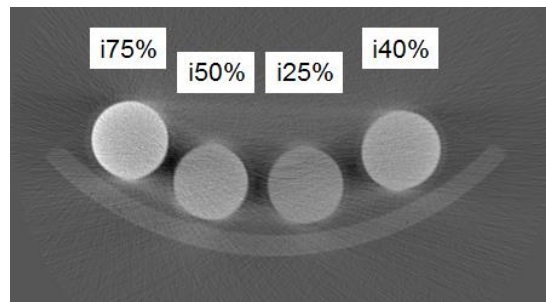


Figure 5-7: Axial slice of four Eppendorf filled with different concentrations of a mixed iodine and saline solution.

The phantom is made out of a cylindrical, universal sample tube with a height of 5 cm and an approximate diameter of 3 cm (Figure 5-8 (a)). The bones are simulated with the iodine solution (Figure 5-8(c)), which will be inserted into two Eppendorfs of 1 ml (Figure 5-8 (b)). Afterwards, the bottle is filled almost up to the top with water which simulates the soft tissue. Finally, the containers with the mixture are stuck to the lid of the bottle with help of modelling clay.

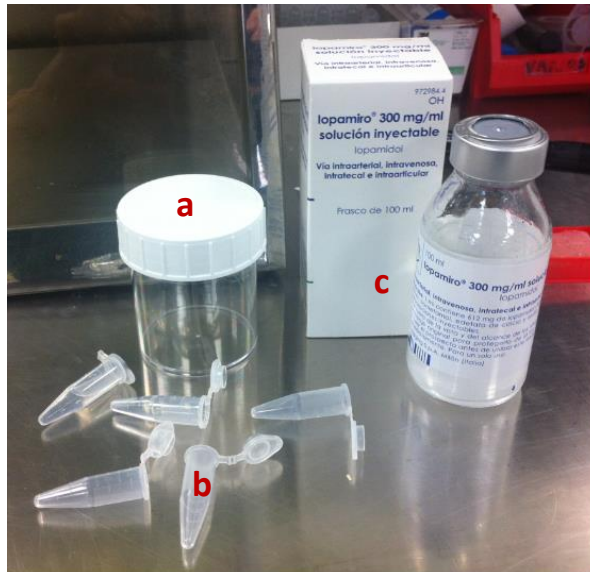


Figure 5-8: Materials used for the fabrication of the BH second order calibration/test phantom.

5.3 Correction

5.3.1 Software development and integration of the second order correction procedure

If 'Second order correction' is set, a new different internal path is taken. The following flow chart shows the structure of the correction process integrated into the MMWKS console.

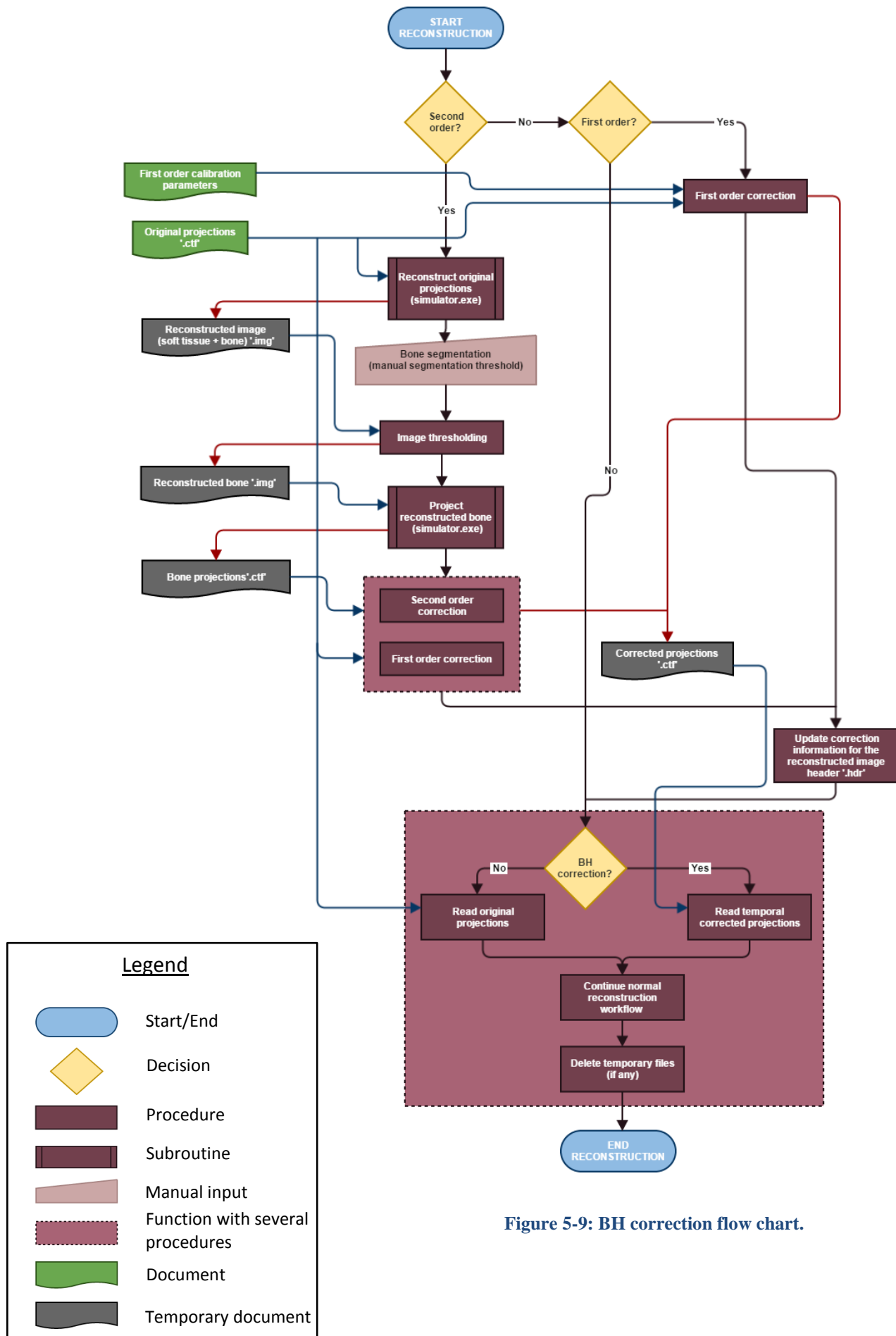


Figure 5-9: BH correction flow chart.

The functions implemented for the second order correction module are BH_Simulator, CreaMascara, and BH_correction_second.

- **Second order correction module**

- **BH_Simulator** is a prototype in charge of reconstructing projections (FDK), or projecting reconstructed images depending on a keyword (/RECON, or /PROY respectively). The generated files are temporarily saved in *path_ct*.

It employs the following parameters:

- **path_act**: string with the directory path in which are the header file with extension '.act' and the data files with extension '.ctf' from the acquisition of the test phantom.
 - **path_ct**: string with the directory path in which is the reconstruction software (Mongoose).
- **CreaMascara** is a prototype in charge of creating a cyan mask which is placed on top of the reconstructed image. This mask depends on the threshold *umbral*.
 - **maniqui_BH**: reconstructed image from the calibration phantom projections.
 - **umbral**: value that separates the bone from soft tissue (in HU).
- **BH_Correction_second** is a prototype that corrects the original projection data ('.ctf') first by linearization, and secondly by post-processing.

It employs the following parameters: **path_act**, **path_ct**, and **umbral**.

The following sequence diagram shows roughly what is happening in the system.

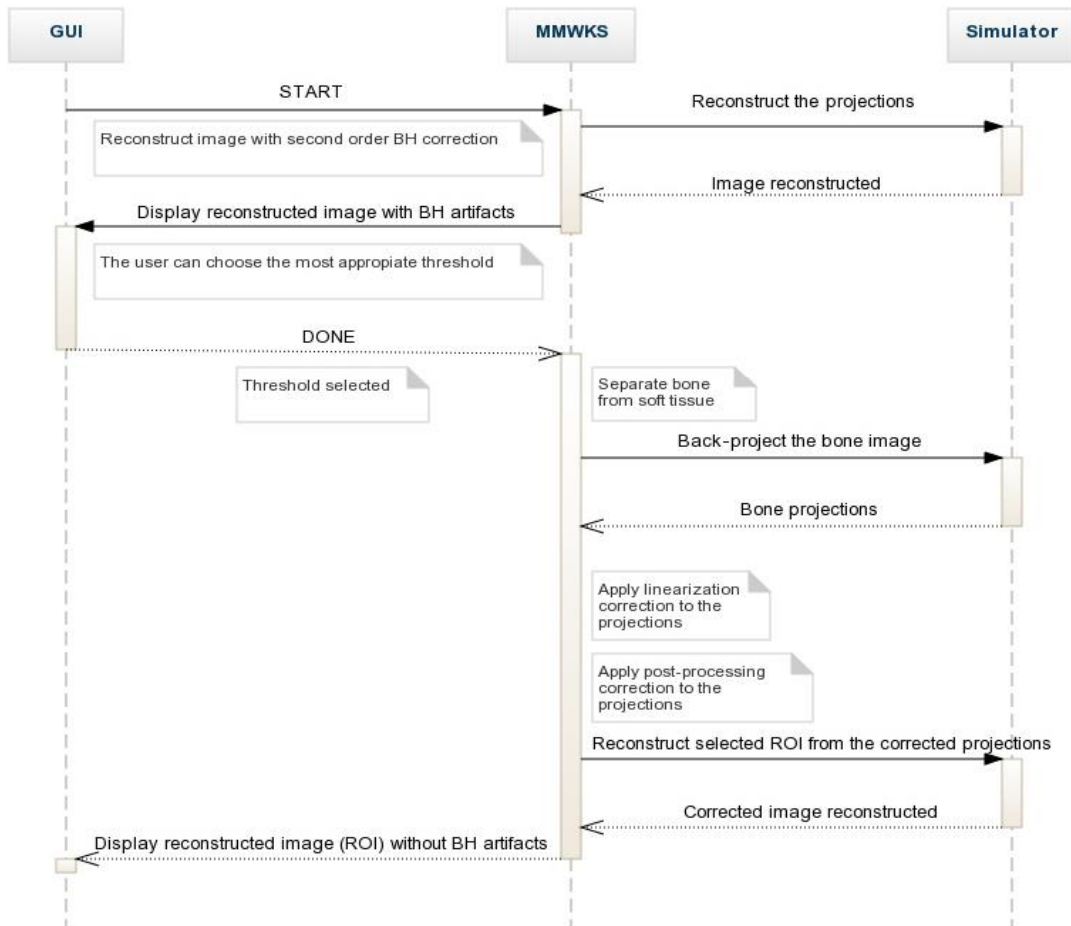


Figure 5-10: Sequence diagram of the second order BH correction.

First of all, the MMWKS calls the simulator. The simulator reads the '.act' header of the raw data and reconstructs it. The provisional resulting volume is called 'volume_recon.img'. This whole volume is displayed into the beam hardening correction interface. By default, the first slice is shown, but it can be change by scrolling up and down the sliding bar placed in the right part of the image (Figure 5-10). This implementation allows the user to select a slice which contains both soft and hard tissue. There is also a sliding bar on the bottom of the image which represents the threshold between both tissues, and helps the user performing the bone segmentation. Unlike the segmentation mask developed in the first order correction, this mask employs an RGB image and places it on top of the original volume. This decision was made due to the small size of the objects to segment (rats and mice bones), in order to avoid 'over-segmentation'. The original image stays underneath as a reference point. Once the user is pleased with the result, the MMWKS can go on with the segmentation procedure by clicking the button 'DONE'.

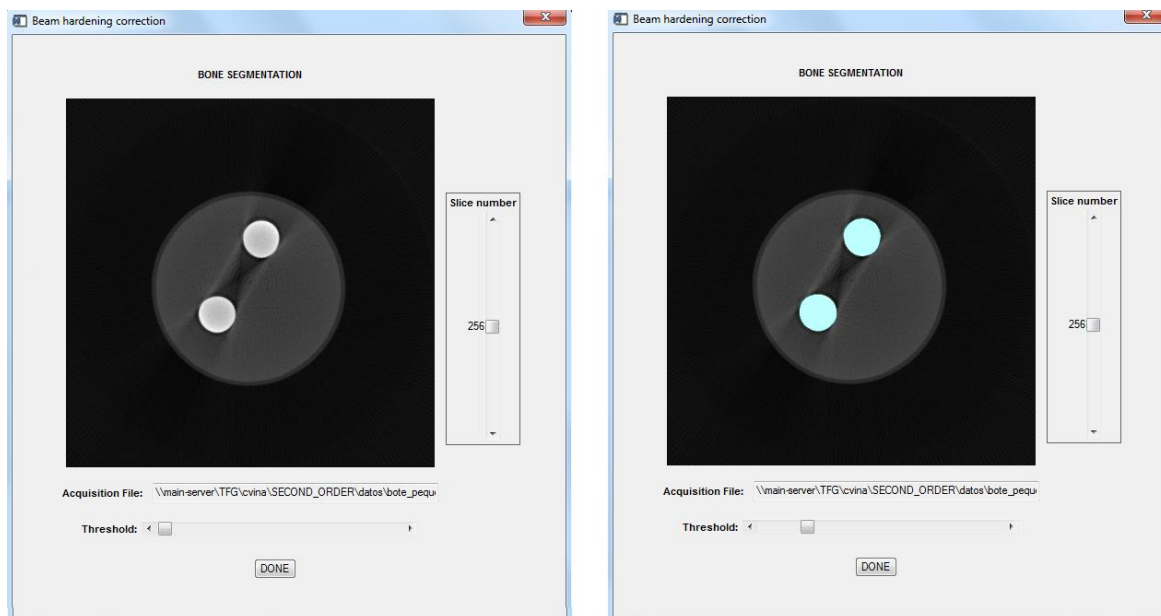


Figure 5-11: Second order segmentation interface, (left) without mask, and (right) with it.

The segmentation procedure is one of the most important parts as it is in charge of separating the soft from the hard tissue. It is possible to achieve this by just taking the pixels of the image whose value is greater or equal than the threshold value. This new generated volume contains only the bone and it is saved as 'hueso_recon.img'. Then, the simulator projects it, and generates as many '.ctf' as beds used. Each '.ctf' contain 360 projections and is saved as 'proy_hueso_X.ctf', being X the corresponding number of bed, starting at 0. These and the original projections are opened, and the first order correction method is applied (same as described in the previous chapter) for reducing any cupping effect they may have. Afterwards, the second order correction is applied to the linearized projections following the formula 5.7). Finally, the corrected projections are temporarily saved and the simulator will reconstruct the chosen ROI (if any was previously selected) and display the result to the user in the console.

5.4 Evaluation

Figure 5-12 shows the resulting reconstructed CT images of the phantom exposed above (section 5.2.1) acquired at a voltage of 35 kVp.

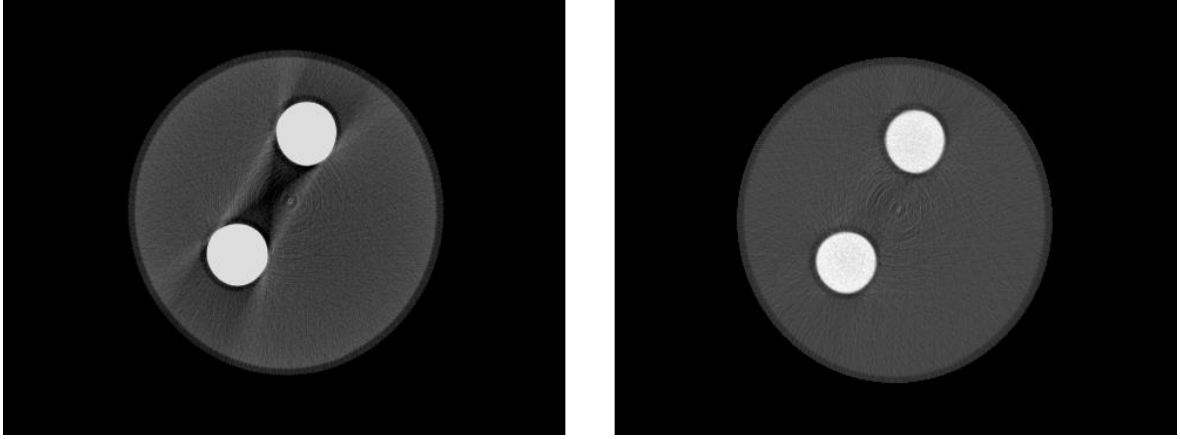


Figure 5-12: (Left) reconstructed projections without correction, and (right) same projections with second order correction.

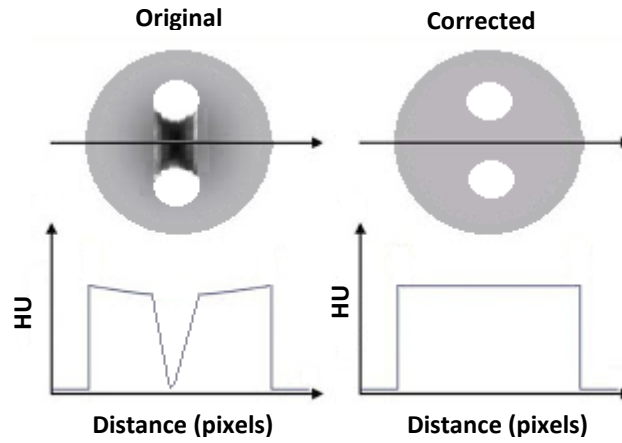
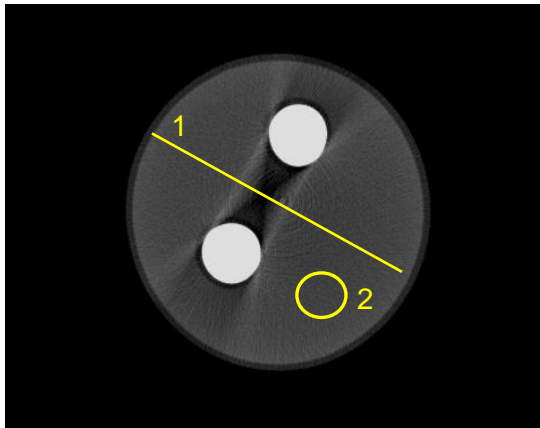


Figure 5-13: Profile representation of the dark streaks effect and its correction.

In order to evaluate the second order correction, we have followed a similar procedure to the first order. Dark streaks are quantified in both the original and the corrected image by tracing a perpendicular profile to them and measuring the Artifact-Noise Ratio (ANR).

$$ARN = \frac{\mu - min}{\sigma} \quad (5.9)$$

where μ is the mean value in an area without the artifact, min the minimum value within the affected area, and σ the standard deviation in an area without the artifact.



Results					
File	Edit	Font	Results		
	Area	Mean	StdDev	Min	Max
1	255	372.853	267.192	-1000	839.860
2	640	469.125	79.036	177	716

Figure 5-14: Reconstructed image from the second order phantom and the data obtained to when analysing different regions to calculate its ANR.

After computing the ANR in both the original and the corrected images, it can be obtained the dark streaks reduction (DSR) percentage by simple applying (5.10).

$$DSR = \frac{ANR_{or} - ANR_{corr}}{ANR_{or}} \cdot 100\% \quad (5.10)$$

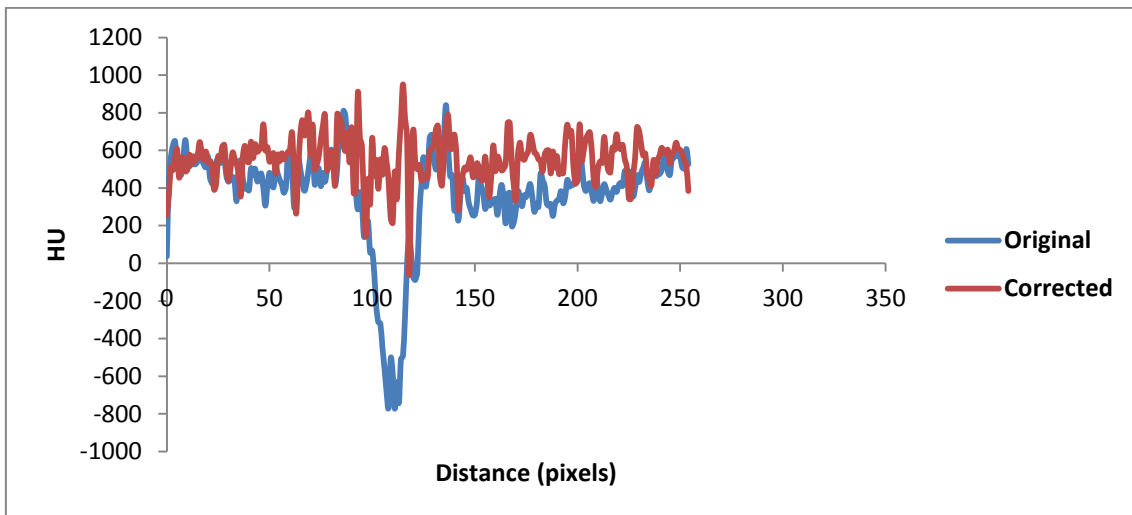


Figure 5-15: Profile representation of the dark streaks effect and its correction.

The ANR for the original image is 18.58, while the corrected image has an ANR of 4.76. Therefore, the dark streaks have been approximately reduced a 74.39 %.

CONCLUSIONS AND FUTURE WORK

6 Conclusions and future work

6.1 Conclusions

This bachelor thesis developed in closely collaboration with the Biomedical Imaging and Instrumentation Group of the University Carlos III de Madrid has focused on the development and integration of compensation algorithms for the BH artifacts into a preclinical, high-resolution micro-CT scanner.

In the first place, the basic concepts of medical imaging were reviewed. Afterwards, it was made an in-depth examination of the Argus PET/CT scanner placed at the Hospital General Universitario Gregorio Marañón for gaining a better understanding of its working mechanisms. Later, the user interface was studied as well as the communication protocols between the user PC and the control PC.

The first order method has been implemented into the console for the correction of the BH artifacts produced in homogeneous objects (cupping). This method is composed of two separate phases: calibration and correction. An appropriate calibration phantom has been designed and manufactured, and it has been defined a calibration protocol which guides the technical staff on the BH calibration process. The protocol details the phantom placement in the scanner's bed in which a part of it must stick out of the bed in order not to alter the measurements. During the calibration process, the adequate value of the calibration parameters is found. One of the limitations encountered in this phase lies in the acquisition of the scanogram. The coronal and sagittal views are obtained independently, i.e., the console has to make two different calls to the scanner one for each view, resulting in a time consuming situation as at the end of each call the scanner's bed returns to its home position. The stability of the calibration parameters has been studied throughout time after calibrating in several days and it has been proved to be stable. Therefore, it is concluded that the calibration is just needed when setting-up the scanner.

The second order method has been also implemented into the console for the correction of the BH artifacts produced in heterogeneous objects (dark streaks). This method assumes that the object under study is composed exclusively by soft tissue

and bone. The correction is based on the error estimation from the contribution of dense objects to the projection, by using the weighting parameters A and B. The value of A has influence over the bone quantification in the reconstructed images, and the value of B affects the correction of the dark streaks. It has been made an optimum search of these parameters by simulation of a rat study. It has been observed that A and B depend on the amount of bone traversed by the X-rays and on the source voltage. It has been also detected that the value of A tends to increase as the bone thickness grows, and the value of B is slightly affected by voltage variations. Hence, it would be necessary to make an exhaustive study of their stability by taking into account these parameters.

Both corrections has been incorporated into the commercial scanner Argus PET/CT by taking into account the communication flow between the control PC and the user PC. The integrated code was designed in order to provide a GUI with the following principles: consistency (the interface uses the appropriate terms and concepts), ease of use (it is intuitive and easy to understand and use), robustness (it is robust and reliable, avoiding failures), user control (it provides the user the authority to abort processes), and flexibility (implementation of different input tools).

The complete scheme of beam hardening correction incorporated into the console has been evaluated in phantom and small animal studies leading to satisfactory results. The cupping effect has been corrected an 83.98 % on average, whereas the dark streaks have been reduced a 74.39 % on average.

Finally, it is worth mentioning that the software developed in this project has been incorporated into the Argus PET/CT scanner commercialized worldwide by SEDECAL. The software is currently at the last validation stage and it will keep under evaluation by the lab technicians.

6.2 Future work

The following work lines have been proposed for the improvement of the calibration procedures used in this project.

- First order calibration

- Modification of the acquisition code (in C) in order to avoid the double insertion of the scanner's bed when obtaining a scanogram.

- Second order calibration

- Exhaustive study of the calibration parameters A and B, and their dependencies with respect to the voltage and the amount of bone traversed by the X-rays.
- Design and implementation of a dedicated calibration interface.

Appendix A: Bibliographic review of the beam hardening correction methods

The research on beam hardening artifacts in computed tomography has been wide-ranging for the last decades, resulting in the publication of a broad amount of strategies to reduce them. The methods described in the literature fall into five groups: physical pre-filtering, linearization, post-processing, dual energy, and iterative reconstruction.

Physical pre-filtering (Brooks *et al* 1976) is usually included in order to harden the X-ray beam before it arrives at the object under study. This filter absorbs not only the lower energy photons, but also reduces the quantity of photons that reach the detector improving the SNR. These filters reduce considerably the beam hardening artifacts, but are not enough to remove them completely.

Linearization methods (Brooks *et al* 1976, Herman 1979, and McDavid *et al* 1997) transform the projection data acquired with a polychromatic source into the projection data that would have been acquired in the equivalent case of a monochromatic source. In order to do so, it is necessary to obtain the attenuation curve with BH for different thicknesses of the material of the scanned object. This method corrects cupping in homogenous objects, but it is insufficient to remove the dark streaks that appear in between denser areas in heterogeneous volumes.

Post-processing techniques (Joseph *et al* 1978, Nalcioglu *et al* 1979, Joseph *et al* 1997, and Hsieh *et al* 2000) reconstruct initially with FBP and afterwards, detach bone and soft tissue from the image by using a density threshold. The image with the segmented bone is projected, and it provides an estimation of the quantity of nonlinear distortion suffered by the beam hardening effect which will be later corrected. When applying FBP to the corrected data, the artifacts in the image are significantly reduced. It is also possible to iterate the procedure a couple of times in order to improve the result of the image, as the artifacts may hamper the segmentation in the first iteration.

Dual energy scanners double the number of measurements by acquiring at two separate energy voltages (preferably with spectrums that do not cover themselves up). Dual energy methods (Alvarez *et al* 1976, Kelcz *et al* 1979, Stonestrom *et al* 1981, Sukovic *et al* 1999, and Fessler *et al* 2002) enable the reconstruction of separate bone and soft tissue images. They model the dependency of the attenuation coefficients with respect to the energy as the combination of two basic functions which represent, for example, both the contributions of the photoelectric and the dispersion effects. The coefficients of these two functions are computed for each pixel of the image. Once obtained, the reconstruction of the coefficients of linear attenuation can be estimated at any energy within the diagnostic range (normally between 80 *kVp* and 120 *kVp* in scanners for humans). These types of scanners are really useful for the characterization of tissue and its quantification, but they require a sophisticated hardware and a greater radiation dose. Therefore, their use is limited to specific applications such as measuring the bone mineral density in the vertebral column (Kalender *et al* 1995), the detection of pulmonary embolism and plaque in coronary arteries, etc.

Iterative reconstruction methods have been widely researched by several authors (Yan *et al* 2000, De Man *et al* 2001, Elbakri *et al* 2002, Menvielle *et al* 2005, O'Sullivan *et al* 2007, and Abella *et al* 2009).

Yan *et al* developed a non-statistical, iterative reconstruction method including the polyenergetic characteristics of the X-ray beam, and whose algorithm is valid for both single and dual-energy CT imaging. The single energy version of the algorithm assumes that each voxel in the scan field can be expressed as a mixture of two known materials and iteratively computes their volume fraction at each pixel.

On the other hand, De Man *et al* proposed an alternative statistical approach that models the object attenuation as a linear combination of the attenuation properties of two base substances. The algorithm uses the polyenergetic source spectrum and does not need a pre-segmented image. In (Alvarez and Macovski 1976), it was stated that the attenuation suffered by a material as a function of the energy can be modelled as a weighted combination of the Compton scatter and the photoelectric effect.

Elbakri *et al* introduced a statistical algorithm that required an initial pre-segmentation of the object into the various tissue classes and did not allow pixels to have tissue mixtures. One year later, the authors remove the need of image pre-thresholding and allow mixed pixels. Both approximations required tabulated measurements of the line integrals of bone and water over a reasonable range of object thicknesses.

In order to avoid modelling of the X-ray spectrum, Abella *et al* presented a simplified approximation based on the statistical reconstruction for systems with a polychromatic source, and using the same calibration data and parameters as in (Joseph *et al* 1978).

Iterative methods are pretty flexible with respect to the acquisition geometry, and they allow including prior knowledge, and model the noise. However, these methods entail a high computational cost as well as a change in the complete reconstruction process.

Throughout the actual research that involves this project, three out of the five methods mentioned above have been incorporated into the Argus PET/CT scanner: physical pre-filtering, linearization and post-processing.

Appendix B: '.ACT' header example

BH_Calibration_24_02_15_24Feb2015_Acq014

Tue 24 Feb 2015 12:50:26 PM CET

[Acquisition]

acq_code_version=4.20

base_filename="BH_Calibration_24_02_15_24Feb2015_Acq014"

Num_projections=360

Binning=4

Frames=8

Voltage=50.000000

Amperage=198.094040

Overlap=0.000000

Bed_positions=1

AI_filter=1.000000

Shutter_mode=0

Init_angle=0

Scan_Angle=360

Rot_direction=0

Init_bed_position=255.000000

[Output files]

Num_files=2

Util_pixels_Z=2400

Proj_size_axial=570

Util_pixels_Y=2400

Proj_size_radial=516

Projections_per_file=180

[Calibration]

file_detector_corrections="d_corrections_CT.txt"
File_flood="flood4bin"
file_dark="dark4bin"
file_hounsfield="hounsfield"
magnification_CT=1.641380
alfa_bed_error=-0.002857
beta_bed_error=0.000000
dz_bed_error=4.926110
D_so=226.000000

[PET/CT alignment]

offset_x=-0.901000
offset_y=0.232000
offset_z=-174.639008

[Info]

GENERAL DATA :=

original institution :=unknown

originating system :=unknown

contact person :=unknown

patient name :=BH_Calibration_24_02_15

patient ID :=

patient breed:=

patient dob:=

patient age:=

patient sex:=Other

patient weight (gr):=

patient size (cm):=

patient orientation :=Head_in

patient rotation :=Prone

study ID :=

study date :=24/2/2015

study time :=12:54:08

data description :=

process description:=

user comment:=

[log]

Appendix C: '.HDR' header example

;INTERFILE -Grupo Imagen UMCE HGGMTue Apr 21 13:07:52 2015

INTERFILE :=

imaging modality:=ct

version of keys := 5.4

date of keys := 2006:22:10

acq code version:=4.20

reconstruction code version:=version: 3.2.2

GENERAL DATA :=

original institution:=unknown

originating system:=unknown

contact person := www.hggm.es/image

patient name:=BH_Calibration_10_02_15

patient id:=none

patient breed:=unknown

patient dob:=none

patient age:=unknown

patient sex:=Other

patient weight (gr):=0

patient size (cm):=unknown

patient orientation:=head_in

patient rotation:=prone

study id:=none

study date:=10/2/2015

study time:=12:44:17

data description:=none

process description:=Reconstructed CT

user comment:=none

name of data
file:=BH_Calibration_10_02_15_10Feb2015_Acq014_corr_calib17_03.img

IMAGE DATA :=

imagedata byte order:=littleendian

slice orientation:=

number format:=signed integer

number of bytes per pixel:=2

number of dimensions:=3

matrix size [1]:=516

matrix size [2]:=516

matrix size [3]:=276

scaling factor (mm/pixel) [1]:=0.121849

scaling factor (mm/pixel) [2]:=0.121849

scaling factor (mm/pixel) [3]:=0.121849

data compression := none

number of time frames:=1

offset [1]:=-0.901000

offset [2]:=0.232000

offset [3]:=164.029

gated data:=no

average cycle length (msec):=NA

cyclelength deviation (%):=NA

accepted deviation (%):=NA

CT IMAGE DATA:=

number of projections:=360

projection binning:=4

voltage (kv):=35.0000

amperage (ua):=238.123

start horizontal bed position (mm):=321.000
overlap (mm):=0.0
magnification factor:=1.64138
number of bed positions:=1
alum filter thickness (mm):=1.00000
projection size [1]:=516.000
projection size [2]:=516.000
projection size [3]:=570.000
number of shots:=8
beam hardening:=First order correction (BH Calibration parameters: 276.147,
0.809976, 4.26709e-005)
reconstruction binning:=1
method of reconstruction:=FeldKamp
type of interpolation:=Lineal
method of scatter correction:=NONE
axial correction:=YES
vertical smooth:=NO
axial smooth:=NO
ring reduction:=NO
TEMPORAL STUDY :=
index nesting level := {time frame}
image duration (sec) [1] :=0.000000
image relative start time (sec) [1] :=0.000000
END OF INTERFILE :=

Bibliographical references

- [1] **Abella, M. and J.A. Fessler**, *A new statistical image reconstruction algorithm for polyenergetic X-ray CT*. Proceedings of the 2009 IEEE International Symposium on Biomedical Imaging (ISBI), pp. 165-8, 2009.
- [2] **Abella, M., J.J. Vaquero, A. Sisniega, J. Pascau, A. Udías, V. García, I. Vidal, and M. Desco**, *Software Architecture for Multi-Bed FDK-based Reconstruction in X ray CT Scanners*. Computer methods and programs in biomedicine, 2011.
- [3] **Alvarez, R.E. and A. Macovski**, *Energy-selective reconstruction in x-ray computerized tomography*. Phys. Med. Biol., vol. 21(5), pp. 733-44, 1976.
- [4] **Barrett, J.F. and N. Keat**, *Artifacts in CT: Recognition and Avoidance*. RadioGraphics, vol. 24, pp. 1679-91, 2004.
- [5] **Brooks, R.A. and G.D. Chiro**, *Beam hardening in x-ray reconstruction tomography*. Phys. Med. Biol., vol. 21, pp. 390-8, 1976.
- [6] **Bissonnette, J.P., L.J. Schreiner**, *A comparison of semiempirical models for generating tungsten target x-ray spectra*, Med. Phys., vol. 19 (3), pp. 579-82, 1991.
- [7] **De Man, B., J. Nuyts, P. Dupont, G. Marchal, and P. Suetens**, *An Iterative Maximum-Likelihood Polychromatic Algorithm for CT*. IEEE Trans. Med. Imaging, vol. 20(10), pp. 999-1008, 2001.
- [8] **De Molina, C.**, *Corrección del artefacto de endurecimiento de haz (beam hardening) para imágenes obtenidas con tomógrafo de rayos X de pequeños animales*, Universidad Autónoma, April 2012.
- [9] **Desco, M.**, *Técnicas avanzadas de imagen en medicina*. Medicina Experimental. Hospital General Universitario ‘G. Marañón’, 2010.
- [10] **Elbakri, I.A. and J.A. Fessler**,
Statistical Image Reconstruction for Polyenergetic X Ray Computed Tomography. IEEE Trans. Med. Imaging, vol. 21(2), pp. 89-99, 2002.
Segmentation-free statistical image reconstruction for polyenergetic x-ray computed tomography with experimental validation. Phys. Med. Biol., vol. 48(15), pp. 2453-77, 2003.
- [11] **Feldkamp, L.A., L.C. Davis, and J.W. Kress**, *Practical cone-beam algorithm*. J. Opt. Soc. Amer., vol. 10(6), pp. 612-9, 1984.

- [12] **Fessler, J.A., I.A. Elbakri, P. Sukovic, and N.H. Clinthorne**, *Maximum likelihood dual-energy tomographic image reconstruction*. Proc. SPIE, vol. 4684(1), pp. 38-49, 2002.
- [13] **Herman, G.T.**, *Correction for beam hardening in computed tomography*. Phys. Med. Biol., vol. 24(1), pp. 81-106, 1979.
- [14] **Hsieh, J., R.C. Molthen, C.A. Dawson, and R.H. Johnson**, *An iterative approach to the beam hardening correction in cone beam CT*. Med. Phys., vol. 27(1), pp. 23-9, 2000.
- [15] **Hounsfield, Godfrey N., J. Radiol**, *Computed Medical Imaging Nobel Lecture*, vol. 61(6-7), pp: 459-68, 1980.
- [16] **Joseph, P.M. and R.D. Spital**, *A Method for Correcting Bone Induced Artifacts in Computed Tomography Scanners*. Comput Assist Tomogr, vol. 2, pp. 100-8, 1978.
- [17] **Joseph, P.M. and C. Ruth**, *A method for simultaneous correction of spectrum hardening artifacts in CT images containing both bone and iodine*. Med. Phys., vol. 24(10), pp. 1629-34, 1997.
- [18] **Kak, A.C., Slaney, Malcolm**, *Principles of Computerized Tomographic Imaging*. IEEE Press, 1988.
- [19] **Kalender, W.A., D. Felsenberg, H.K. Genant, M. Fischer, J. Dequeker, and F. Reeve**, *The European Spine Phantom a tool for standardization and quality control in spinal bone mineral measurements by DXA and QCT*. European Journal of Radiology, vol. 20, pp. 83-92, 1995.
- [20] **Kelcz, F., P.M. Joseph, and S. Hilal**, *Noise considerations in dual energy CT scanning*. Medical Physics, vol. 6, pp. 418-25, 1979.
- [21] **Lewis, J.S. and S. Achilefu**, *Small Animal Imaging: Current Technology and Perspectives for Oncological Imaging*. Eur. J. Cancer, vol. 38, pp. 2173-88, 2002.
- [22] **McDavid, W.D., R.G. Waggener, W.H. Payne, and M.J. Denis**, *Correction for spectral artifacts in cross-sectional reconstruction from X-rays*. Med. Phys. vol. 4(1), pp. 54-7, 1997.
- [23] **Menvielle, N., Y. Goussard, D. Orban, and G. Soulez**, *Reduction of beam hardening artifacts in x-ray ct*. IEEE-EMBS 2005. 27th Annual International Conference of the engineering in Medicine and Biology Society, 2005.

- [24] **Nalcioglu, O. and R.Y. Lou**, *Post-reconstruction Method for Beam Hardening in Computerised Tomography*. Phys. Med. Biol., vol. 24(2), pp. 330-40, 1979.
- [25] **O' Sullivan, J. and J. Benac**, *Alternating Minimization Algorithms for Transmission Tomography*. IEEE Transactions on Medical Imaging, vol. 26, pp. 283-97, 2007.
- [26] **Pascau, J., J.J. Vaquero, M. Soto, R. Cacho, J. Sánchez, A. Santos, and M. Desco**, *Multimodality workstation for small animal image visualization and analysis*. Molecular Imaging and Biology, vol. 8, 2006.
- [27] **Stonestrom, J., R.E. Alvarez, and A. Macovski**, *A framework for spectral artifact corrections in X-ray CT*. IEEE Transactions on Biomedical Engineering, vol. 28, pp. 128-41, 1981.
- [28] **Sukovic, P. and N.H. Clinthorne**. *Design of an experimental system for dual energy xray CT*, IEEE Nuclear Science Symposium Conference Record, 1999.
- [29] **Vaquero, J.J., S.Redondo, E.Lage, M.Abella, A.Sisniega, G.Tapias, M.L.S. Montenegro, and M.Desco**, *Assessment of a New High-Performance Small-Animal X-Ray Tomograph*. IEEE TRANSACTIONS ON NUCLEAR SCIENCE, vol. 55, pp. 898-905, 2008.
- [30] **Yan, C.H., R.T. Whalen, G.S. Beaupré, S.Y. Yen, and S. Napel**, *Reconstruction algorithm for polychromatic CT imaging: application to beam hardening correction*. IEEE Trans. Med. Imaging, vol. 19, pp. 1-11, 2000.

Glossary of terms

I. Acronyms

BH: Beam Hardening

CT: Computed Tomography

FBP: Filtered Backprojection

FDK: Feldkamp, David y Kreis

FOV: Field Of View

FT: Fourier Transform

GUI: Graphical User Interface

IDL: Interactive Data Language

LIM: Laboratorio de Imagen Médica

MMWKS: Multimodality Workstations

MSE: Mean Square Error

PET: Positron Emission Tomography)

PPMA: Poly methyl methacrylate

ROI: Region Of Interest

UMCE: Unidad de Medicina y Cirugía Experimental

SEDECAL: Sociedad Española de Electromedicina y Calidad

SNR: Signal-to-Noise Ratio

SPECT: Single Positron Emission Tomography

II. Units of measurement

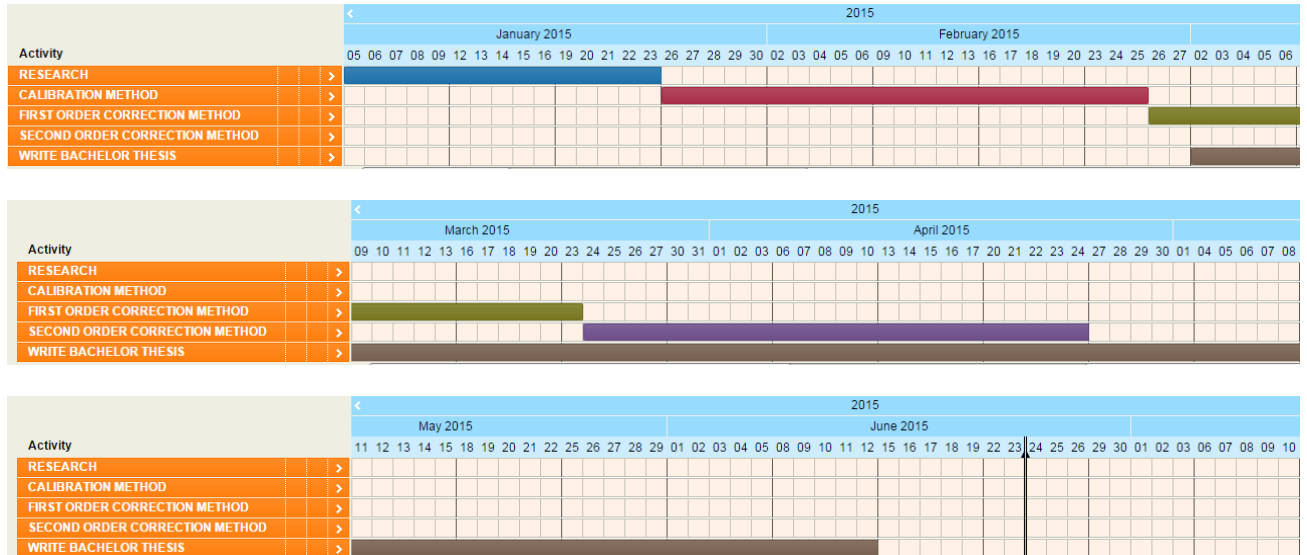
eV: electronvolt

HU: Hounsfield Units

kVp: kilovolt peak

Project management

I. Gantt chart



- **RESEARCH** (5th - 23th January)
- **CALIBRATION METHOD** (26th January – 25th February)
- **FIRST ORDER CORRECTION METHOD** (26th February – 23th March)
- **SECOND ORDER CORRECTION METHOD** (24th March - 24th April)
- **WRITE BACHELOR THESIS** (2nd March - 12th June)

Milestones:

- **23th January 2015:** Project management: Gantt chart planning.
- **2nd March 2015:** Abstract.
- **20th March 2015:** Introduction.
- **23th March 2015:** Presentation of the goals of my bachelor thesis at the LIM.
- **31st March 2015:** Motivation.
- **19th April 2015:** Materials and methods: First order correction.
- **17th May 2015:** Materials and methods: Second order correction.
- **7th June 2015:** Results.
- **11th June 2015:** Conclusions and future work
- **12th June 2015:** Final presentation of my bachelor thesis at the LIM.

II. Financial plan

Supplies and materials

- PC Intel Core 2 Duo 4,00 GB RAM + Monitor Dell 18' 1,000 €
- Matlab license..... 6,000 €
- IDL license..... 300 €
- Office furniture..... 100 €
- Calibration phantom..... 40 €
- Test phantom..... 3 €
- Depreciation and amortization¹..... 595.44 €
- Argus PET/CT rental fee 180 € per hour
(30 hours)

Total Supplies and materials..... 5,995.44 €

Direct personnel cost

Salaries

- Engineer fees..... 15 € per hour
(600 hours)
- Support staff fees..... 20 € per hour
(50 hours)

Total Salaries..... 10,000 €

Travel expenses

- Season ticket 54.60 € per month
(6 months)

Total Travel expenses..... 327.60 €

Total Direct personnel cost..... 10,327.60 €

Subtotal budget..... 16,323.04 €

Non recoverable VAT

- 21% Subtotal budget 3,427.83 €

Total budget..... 19,750.87 €

Madrid, June 2015
Cristina Viña Berlanga
Telematics Engineer

¹ Depreciation/amortization calculation: $D = (P - R) \cdot \frac{T}{L}$

P: product value, S: residual value (20% product value), T: time used (6 months), and L: useful life (60 months)